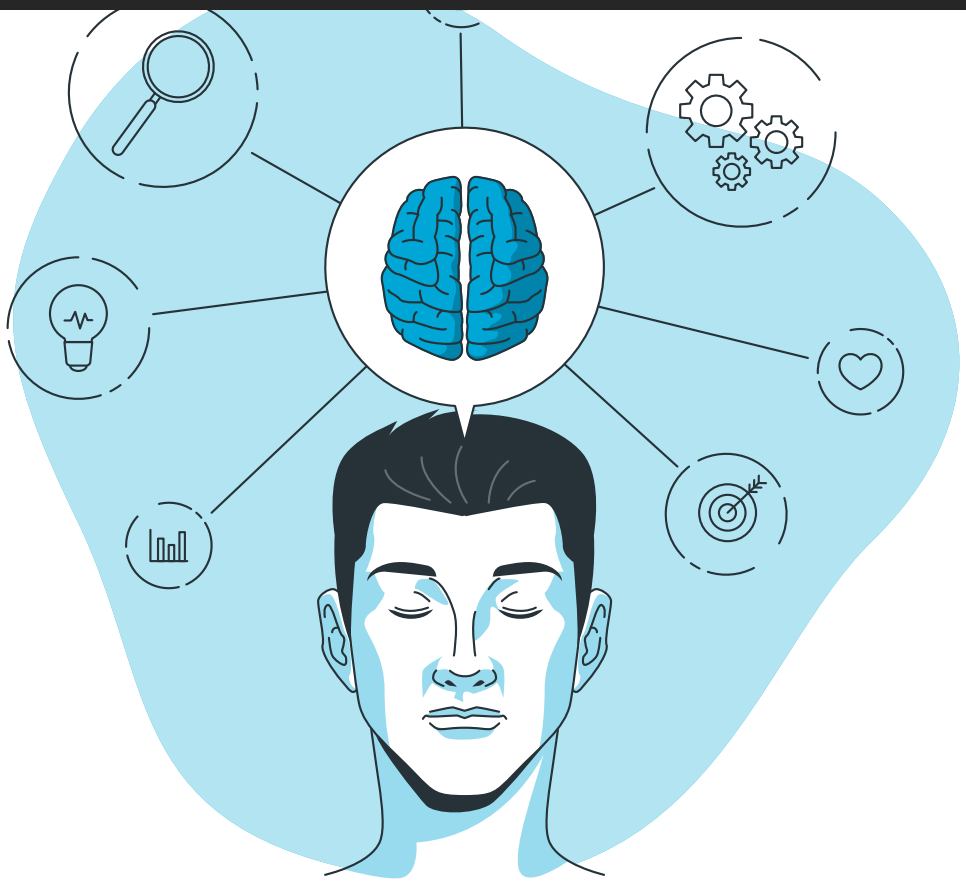
Design and Fabrication of an Upconversion-Based Optical Platform for Cardiac NADH Fluorescence Excitation

Master Thesis

Z. Wang

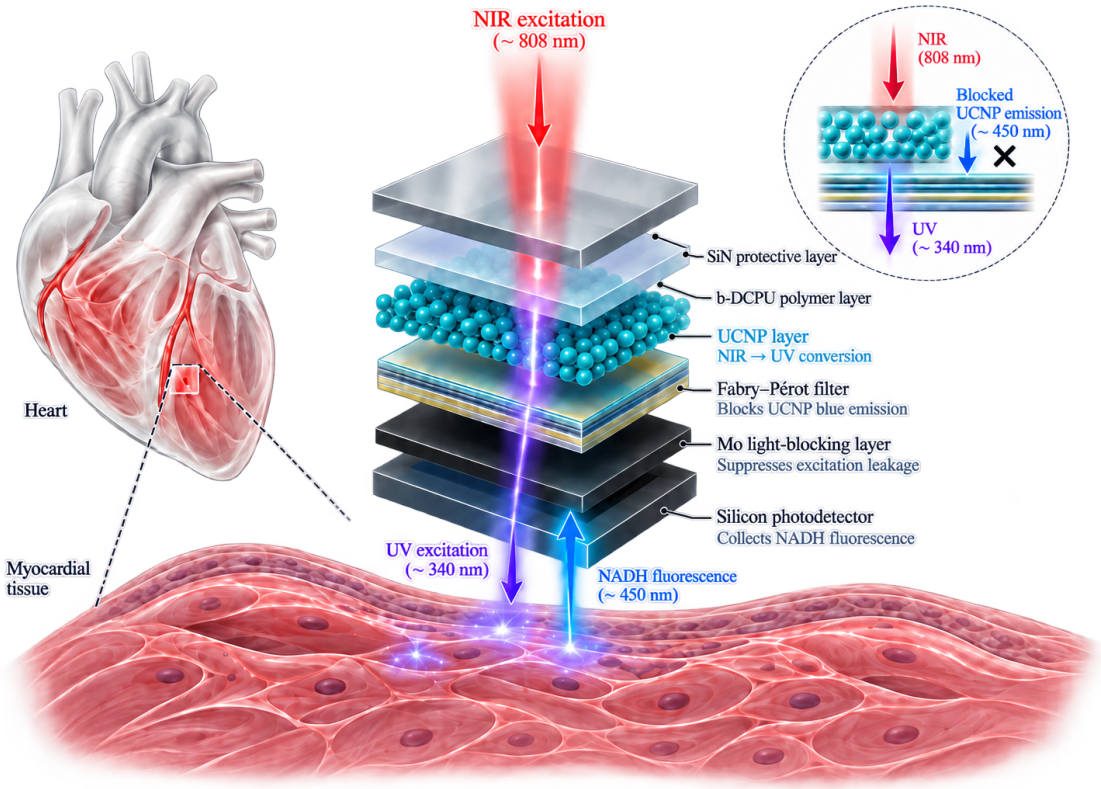


Design and Fabrication of an Upconversion-Based Optical Platform for Cardiac NADH Fluorescence Excitation

Master Thesis

by

Z. Wang



Thesis committee:

Dr. Filipe Arroyo Cardoso,	TU Delft, Thesis supervisor
Dr. Clementine Boutry,	TU Delft, Thesis supervisor
Dr. Matthias Alfeld,	TU Delft, Thesis co-supervisor
Dr. Marcel Sluiter,	TU Delft, External member
MSc. Z. Liao,	TU Delft, Daily supervisor

TU Delft

Preface

This thesis presents the results of my master's project, titled *Design and Fabrication of an Upconversion-Based Optical Platform for Cardiac NADH Fluorescence Excitation*, carried out as part of the MSc programme in Materials Science and Engineering at Delft University of Technology.

Coming from a materials science background, this project gave me the opportunity to work in the interdisciplinary field of implantable biomedical devices, optical sensing, and microfabrication. Throughout the project, I was involved in the development and integration of a wide range of materials and fabrication processes. The combination of these different techniques made the project both challenging and rewarding, and allowed me to develop a much broader understanding of how materials science can contribute to practical biomedical device development.

One of the most valuable aspects of this project was learning how to translate a conceptual multilayer device design into a practical fabrication sequence. Many unexpected challenges arose during the integration process, and solving them required continuous experimentation, troubleshooting, and adjustment of the original process flow. This experience has greatly strengthened both my experimental skills and my ability to approach engineering problems from a materials perspective.

I would like to express my sincere gratitude to my supervisors, Dr. Filipe Arroyo Cardoso and Dr. Clémentine Boutry, for their guidance, support, and valuable feedback throughout the project. I am also grateful to Dr. Matthias Alfeld for his suggestions during the progress meetings, and to Zhengwei Liao for his continuous practical guidance and support in the laboratory. I would also like to thank the PhD and Master researchers in the ECTM and EI groups for generously sharing their experience and providing valuable advice whenever I encountered experimental or fabrication challenges.

Finally, I would like to express my deepest gratitude to my family members for their continuous support, encouragement, and understanding throughout my studies. They made me make up my mind to travel for 16 hours up in the air to a completely unfamiliar country, stepping out of my confort zone. Their support had been an important source of confidence and motivation during my master's programme and throughout the completion of this thesis.

Z. Wang
Delft, September 2026

Abstract

Heart failure remains a major clinical challenge, creating a need for implantable sensing platforms capable of providing long-term information on cardiac metabolic state. In this thesis, an upconversion-based optical platform was developed toward myocardial NADH sensing, using near-infrared excitation, local wavelength conversion, spectral filtering, and backside photodetection. Rather than focusing on the individual optical components, the main aim of this work was to determine whether these elements could be integrated into a compatible microfabrication workflow.

The proposed device combines a silicon photodetector with front-side optical shielding, a SiO_2/SiN Fabry–Pérot filter, an upconversion nanoparticle layer, and a flexible b-DCPU substrate protected by a SiN hard mask. The main fabrication challenge was the strong coupling between these materials and processes: steps required for one layer could introduce thermal, chemical, or mechanical limitations for another. The process sequence was therefore developed around maintaining detector integrity, optical functionality, and electrical accessibility throughout integration.

Several key process improvements were identified. The Fabry–Pérot filter could be reproduced using calibrated dielectric deposition and patterned using a CHF_3/Ar etching condition with improved selectivity. UCNP deposition became more uniform when the solvent evaporation rate was reduced through humidity control and lower-temperature drying. For the flexible substrate, b-DCPU films with thicknesses within the target integration range were obtained by spin-coating optimization. Tensile testing gave a Young's modulus of approximately 3.37 MPa, and the required polymer thickness for the adopted tensile-rigidity criterion was estimated to be approximately 22.6 µm. To enable photolithography on the polymer, a SiN protection layer was introduced, although interrupted deposition with intermediate cooling was required to avoid thermal damage.

The complete front-side integration sequence was demonstrated on a process-validation detector, showing that the proposed multilayer fabrication strategy is feasible. However, several limitations remain, including incomplete control of UCNP layer thickness, reduced b-DCPU etching efficiency during prolonged plasma exposure, formation of a white post-etch residue, and partial delamination of the Mo light-blocking layer. In addition, the validation detector did not contain a fully opened optical transmission window and therefore did not represent a fully functional sensing device. Further work should focus on improving these remaining process steps and validating the complete optical and electrical sensing performance on a functional detector.

Keywords: cardiac NADH sensing; upconversion nanoparticles; Fabry–Pérot filter; b-DCPU; flexible implantable device; heterogeneous integration; microfabrication; optical sensing.

List of Abbreviations

Abbreviation	Full name
AFM	Atomic Force Microscopy
ATP	Adenosine Triphosphate
b-DCPU	Bioresorbable Dynamic Covalent Polyurethane
DI	Deionized
FP	Fabry–Pérot
HDI	Hexamethylene Diisocyanate
HF	Heart Failure
ICPECVD	Inductively Coupled Plasma Enhanced Chemical Vapor Deposition
NADH	Nicotinamide Adenine Dinucleotide
NAD^+	Oxidized Nicotinamide Adenine Dinucleotide
NIR	Near-Infrared
PCL-triol	Polycaprolactone Triol
PR	Photoresist
SEM	Scanning Electron Microscopy
TMAH	Tetramethylammonium Hydroxide
TEOS	Tetraethyl Orthosilicate
UCNP	Upconverting Nanoparticle
UV	Ultraviolet

Contents

Preface i

Abstract ii

List of Abbreviations iii

1 Introduction 1

2 State of the Art 4
2.1 Clinical Background and Detection Principle . . . 4
2.2 Optical Constraints in Biological Tissues . . . 4
2.3 Upconverting Nanoparticles . . . 5
2.4 Fabry–Pérot Optical Filter . . . 6
2.5 Silicon Photodetector and Backside Detection . . . 7
2.6 Flexible Polymer Substrate . . . 9
2.7 Fabrication Challenges for Device Integration . . . 10
2.8 Research Gap and Objective . . . 11

3 Methods 13
3.1 Integrated Device Design . . . 13
3.2 Starting Detector and Pre-processing . . . 15
3.3 Front-Side Optical Shielding . . . 16
3.4 Fabry–Pérot Filter Integration . . . 17
3.5 UCNP Deposition . . . 18
3.6 Temporary Bonding . . . 19
3.7 b-DCPU Polymer Preparation and Deposition . . . 20
3.8 Mechanical Characterization of b-DCPU . . . 21
3.9 SiN Protective Layer and Polymer Lithography . . . 22
3.10 b-DCPU Dry Etching . . . 23
3.11 Planned Final Fabrication Steps . . . 24
3.12 Characterization Methods . . . 26

4 Experiments and Results 28
4.1 Front-Side Mo Light-Blocking Layer . . . 28
4.2 Fabry–Pérot Filter Fabrication . . . 29
4.3 UCNP Deposition and Optical Characterization . . . 31
4.4 b-DCPU Polymer Preparation and Optical Properties . . . 35
4.5 Mechanical Characterization of b-DCPU . . . 37
4.6 SiN Protective Layer and Polymer Lithography . . . 41
4.7 b-DCPU Dry Etching . . . 42

5 Discussion 48
5.1 Overall Integration Strategy . . . 48
5.2 Optical Functional Layer Integration . . . 48
5.3 Mechanical and Polymer Integration . . . 49
5.4 Dry-Etching Challenges and Process Control . . . 50
5.5 Final Device Validation and Remaining Limitations . . . 51
5.6 Future Process Improvements . . . 52

6 Conclusion 54

References 55

A Fabrication Recipes **59**
A.1 Mo Light-Blocking Layer 59
A.2 Fabry–Pérot Filter Fabrication 59
A.3 UCNP Deposition 60
A.4 b-DCPU Preparation and Deposition 61
A.5 SiN Protective Layer 62
A.6 b-DCPU Dry Etching 62
A.7 Additional Process Development and Alternative Recipes 63

1 Introduction

The heart is one of the most important organs for maintaining normal physiological activities in the human body. Through continuous contraction, it delivers oxygen and nutrients to tissues throughout the body. With the aging of the population and the increasing incidence of cardiovascular diseases, heart failure (HF) has become an important disease that affects patient quality of life and long-term health[1]. Heart failure is commonly accompanied by reduced myocardial contractility and deterioration of tissue metabolic conditions. Therefore, long-term, continuous, and real-time monitoring of cardiac function is of great importance to evaluate disease progression, assess treatment effectiveness, and allow timely clinical intervention[2, 3]. Conventional cardiac examinations mainly rely on large-scale hospital-based instruments or intermittent measurements. Although these approaches can provide relatively accurate diagnostic information, they are difficult to use for continuously reflecting changes in myocardial tissue under the daily physiological conditions of patients. From this point of view, miniaturized sensors that can be implanted for a long period and continuously acquire physiological information from myocardial tissue provide a promising technical route for future cardiac disease monitoring.

The metabolic state of myocardial tissue is closely related to the local oxygen supply. Since cardiomyocytes continuously contract, their energy consumption is extremely high and strongly relies on oxidative metabolism in mitochondria to continuously produce adenosine triphosphate (ATP)[4, 5]. Therefore, the redox state inside myocardial tissue can provide important information on cellular metabolism and cardiac function. However, conventional oxygen monitoring methods mainly measure the oxygen concentration in blood or in the extracellular environment, which may not always directly reflect the metabolic condition inside cardiomyocytes[6]. Nicotinamide adenine dinucleotide (NADH), as an important coenzyme involved in cellular energy metabolism, is closely related to the intracellular redox state and can therefore be considered as a potential biomarker for evaluating myocardial metabolism[7, 8]. More importantly, NADH possesses intrinsic fluorescence properties. It exhibits a strong absorption band around 340 nm and produces fluorescence centered at approximately 469 nm after excitation [9], which makes label-free optical detection possible.

Based on this characteristic, the present project aims to develop an implantable optical sensing platform for myocardial NADH monitoring. The basic concept is to locally generate UV light near myocardial tissue to excite NADH and subsequently collect the resulting blue fluorescence using an integrated photodetector. However, UV light has a limited penetration depth in biological tissue and is therefore difficult to directly deliver from outside the body to the heart[10, 11]. In contrast, red or near-infrared (NIR) light shows a much stronger propagation capability in biological tissue and is more suitable as an external excitation source[12, 13]. To overcome this wavelength mismatch, upconverting nanoparticles (UCNPs) are introduced into the device, which convert the externally incident long-wavelength light into higher-energy UV and blue light near the implantation site. In this way, an optical conversion pathway can be established between the external light source that is able to penetrate biological tissue and the short-wavelength excitation light required by NADH[14, 15, 16].

In addition to UV emission, UCNPs also generate blue light, whose wavelength range significantly overlaps with the fluorescence emission of NADH. If the blue emission generated by the UCNPs directly enters the photodetector, it will be mixed with the target NADH fluorescence signal and consequently reduce the selectivity of the measurement. Therefore, a Fabry–P'erot (FP) optical filter is further introduced into the device to suppress the blue emission from the UCNPs, while allowing the UV light required for NADH excitation to continuously propagate toward the myocardial tissue[17, 18]. Previous work has already investigated the UCNP materials, particle deposition process, and the design, fabrication, and optical performance of the SiO_2/SiN multilayer FP filter. These studies provide an important basis for the further integration of the complete sensing platform.

In the final device, external red or NIR light is incident from the top and passes through the SiN protection layer and flexible polymer substrate before reaching the UCNP layer. The UCNPs convert the

incident light into UV and blue emission. The blue component is suppressed by the Fabry–Pérot (FP) filter, while the UV light passes through the filter and the thinned optical transmission region of the silicon detector to excite NADH in the underlying myocardial tissue. The resulting NADH fluorescence propagates back toward the device and is detected from the backside of the silicon photodetector. To suppress direct front-side illumination of the photosensitive region, a Mo light-blocking layer is integrated on the detector front side. Together, the UCNP layer, FP filter, silicon photodetector, and optical shielding layer form the excitation, filtering, and fluorescence-detection pathway of the device. The simplified working principle of the proposed sensing platform is illustrated in Figure 1.1.

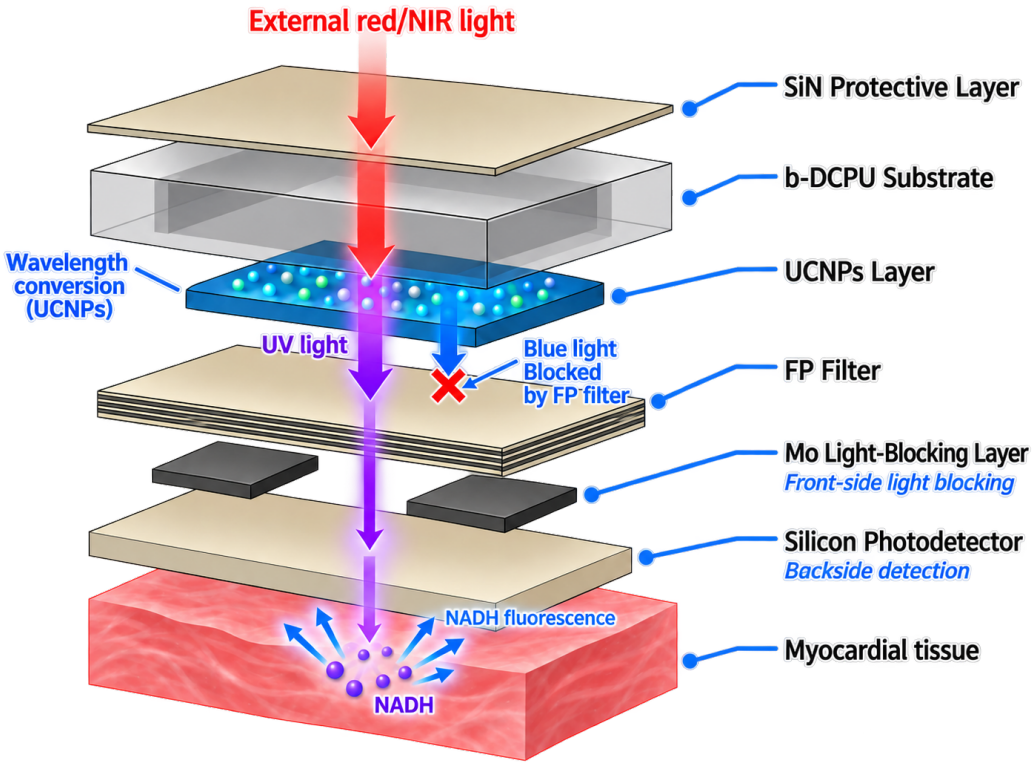


Figure 1.1: Working principle of the proposed optical sensing platform.

Although the individual optical components have been investigated previously, integrating them into a complete implantable device introduces additional fabrication constraints. The device combines a silicon photodetector, an approximately 200 nm Mo light-blocking layer, an approximately 1 µm FP filter, a UCNP layer, an approximately 15 µm to 25 µm b-DCPU polymer substrate, and a SiN protection layer for polymer patterning. These materials differ in their tolerance to deposition temperature, photolithography chemicals, etching conditions, and mechanical stress, while the detector contact pads must remain accessible throughout fabrication. Consequently, the process sequence must be designed to balance optical performance, electrical accessibility, material compatibility, and structural stability.

This thesis therefore focuses on the development of a compatible fabrication workflow for integrating these components. The investigated processes include front-side Mo patterning, FP filter deposition and patterning, UCNP deposition, b-DCPU preparation and mechanical characterization, and polymer photolithography and dry etching. Several practical limitations were identified during fabrication, including multilayer filter etching control, polymer–photoresist incompatibility, post-etch polymer residue, and the mechanical instability of ultrathin silicon. These issues were addressed through process optimization and workflow adjustment, including the introduction of a SiN protection layer and postponing the final silicon thinning step to a later stage of integration.

The objective of this thesis is therefore not to re-establish the fundamental optical mechanisms of the UCNPs or FP filter, but to evaluate whether the existing optical design can be translated into a

practical and compatible microfabrication process. By analyzing material compatibility, etching behavior, structural stability, and process-sequence constraints, this work aims to identify the main limitations of the current integration strategy and provide a fabrication basis for final backside thinning, device release, and subsequent NADH fluorescence detection.

2 State of the Art

2.1. Clinical Background and Detection Principle

2.1.1. Heart Failure

Heart failure (HF) is a clinical condition in which the pumping capability of the heart is reduced, resulting in an insufficient supply of blood and oxygen to body [1]. For patients with chronic heart failure, long-term monitoring of cardiac function is valuable for identifying changes in disease condition at an early stage. For some patients with acute heart failure, continuous monitoring can also provide useful information for evaluating treatment effectiveness and the recovery process[19]. Conventional diagnostic methods mainly rely on large-scale hospital-based equipment and intermittent examinations, which makes it difficult to continuously reflect changes in cardiac function under daily physiological conditions. Therefore, implantable sensors that can perform long-term and real-time monitoring directly near the myocardial tissue provide a potential solution for continuous evaluation of cardiac conditions.

Cardiomyocytes continuously contract and therefore have a relatively high demand for both energy and oxygen. Changes in the local oxygen supply can directly influence mitochondrial metabolism and cellular energy production. As a result, the redox state of myocardial tissue can be considered an important indicator for evaluating cardiac metabolic conditions[5].

2.1.2. NADH

Nicotinamide adenine dinucleotide (NADH) is an important reduced coenzyme involved in cellular energy metabolism. During oxidative phosphorylation, NADH provides electrons to the mitochondrial electron transport chain and is subsequently oxidized to NAD^+. Since this process is closely related to oxygen consumption and adenosine triphosphate (ATP) production, the NADH concentration and NADH/NAD^+ ratio can provide information on the cellular redox state and metabolic activity. Therefore, NADH can be considered a potential indicator for evaluating the local metabolic and oxygenation state of myocardial tissue[5].

NADH also possesses intrinsic fluorescence properties. When excited by ultraviolet (UV) light at approximately 340 nm, NADH generates fluorescence in the blue wavelength region with an emission peak at approximately 469 nm. Since this process does not require the introduction of additional fluorescent labels, the autofluorescence of NADH enables label-free optical detection[9].

2.1.3. Photoluminescence-Based Sensing

Based on the fluorescence properties of NADH, photoluminescence is employed in this project as the fundamental sensing principle for evaluating the metabolic state of myocardial tissue. First, UV light capable of exciting NADH needs to be generated near the myocardial tissue. After excitation, NADH emits blue fluorescence, part of which can be collected by a nearby photodetector and subsequently converted into an electrical signal[9, 20]. By detecting this fluorescence signal, information related to the NADH concentration and metabolic state of the myocardial tissue can be indirectly obtained.

However, the UV excitation light required by NADH has a relatively limited penetration depth in biological tissue, making it difficult to directly deliver the excitation light from outside the body to the myocardial region. Therefore, how to use longer-wavelength light with stronger tissue penetration and locally generate the required UV light near the implantation site becomes a key optical challenge of the proposed sensing strategy[21]. This limitation provides the basis for the following discussion on optical propagation in biological tissue and local wavelength conversion.

2.2. Optical Constraints in Biological Tissues

2.2.1. Light Penetration

When light propagates through biological tissue, its intensity gradually decreases with increasing propagation distance due to the combined effects of absorption and scattering. Different biological tissues have different absorption and scattering coefficients, and these optical properties strongly depend on the wavelength of the incident light[11, 22]. Therefore, the effective penetration depth of light in the human body is largely determined by the selected wavelength.

For myocardial tissue located relatively deep inside the body, short-wavelength light generally experiences stronger absorption and scattering, while longer-wavelength red or near-infrared (NIR) light shows better tissue penetration. Therefore, compared with directly applying UV light from outside the body, red or NIR light is more suitable as the external excitation source for an implantable optical sensing system[12, 23].

2.2.2. Challenges of UV Excitation

NADH requires UV light for effective excitation, while UV light has a limited penetration depth in biological tissue. When UV light is incident from outside the body, its energy is rapidly attenuated through the skin, fat, muscle, and other tissue layers, making it difficult for sufficient optical energy to reach the myocardial region[10]. In contrast, longer-wavelength NIR light generally experiences lower attenuation in biological tissue and is therefore more suitable for delivering optical energy from outside the body to an implanted device.

However, red or NIR light cannot directly excite NADH. Therefore, the incident long-wavelength light needs to be converted into shorter-wavelength light capable of exciting NADH near the implantation site. Based on this requirement, upconverting nanoparticles (UCNPs) are employed in this project as a local wavelength conversion material[16]. The externally incident long-wavelength light is converted by the UCNPs into UV light near the myocardial tissue, thereby avoiding the severe optical attenuation associated with directly transmitting UV light from outside the body.

2.3. Upconverting Nanoparticles

2.3.1. Function of UCNPs in the Device

As discussed in the previous section, red or near-infrared (NIR) light shows relatively good penetration through biological tissue, while its photon energy is insufficient to directly excite NADH. Therefore, upconverting nanoparticles (UCNPs) are employed in this project as a local wavelength conversion material to convert the externally incident long-wavelength light into higher-energy short-wavelength light[16, 24]. The upconversion process is generally achieved through successive photon absorption and energy transfer between rare-earth ions, during which the energy of multiple low-energy photons is gradually accumulated and eventually converted into ultraviolet (UV) or visible-light emission[14].

In the proposed device, the main function of the UCNPs is to generate UV light capable of exciting NADH, thereby enabling local optical excitation near the implantation site. Compared with directly delivering UV light from outside the body, this approach allows red or NIR light with stronger tissue penetration to be used as the external energy source[22]. Meanwhile, no additional electrically driven light source is required inside the implanted device, which is beneficial for simplifying the overall device configuration.

2.3.2. Selected UCNP Structure

A rare-earth-ion-doped UCNP system is employed in this project[25]. Such nanoparticles generally consist of a host matrix together with doped ions serving different functions, including the sensitizer, migrator, and activator. The sensitizer is mainly responsible for absorbing the externally incident long-wavelength light, while the migrator transfers the absorbed energy between different ions. The activator subsequently receives the transferred energy and generates the required short-wavelength emission. By appropriately selecting the combination of these functional ions, energy conversion from long-wavelength excitation to UV or blue-light emission can be achieved[14, 24, 26].

In addition, the luminescence efficiency of UCNPs can be strongly influenced by surface quenching. Excited ions located close to the nanoparticle surface may lose their energy through nonradiative processes associated with surface defects or surrounding molecules[14, 27]. Therefore, a core–shell

structure is commonly introduced to reduce the interaction between the luminescent centers and the external environment, which can consequently suppress surface-related nonradiative energy loss and improve the upconversion emission efficiency[28].

Although the UCNPs can generate the UV light required for NADH excitation, their emission is generally not limited to a single wavelength. The emission characteristics of the UCNPs used in this study are shown in Figure 2.1. In the nanoparticle system employed in this project, blue-light emission is also generated in addition to the desired UV emission. Since this blue wavelength range is very close to the fluorescence emission of NADH, the UCNP-generated blue light may directly enter the photodetector and interfere with the target NADH fluorescence signal[9]. Therefore, the UCNP layer alone is insufficient to achieve reliable NADH detection. A wavelength-selective optical filtering structure is further required to suppress the blue emission generated by the UCNPs while maintaining effective transmission of the UV light used for NADH excitation[18].

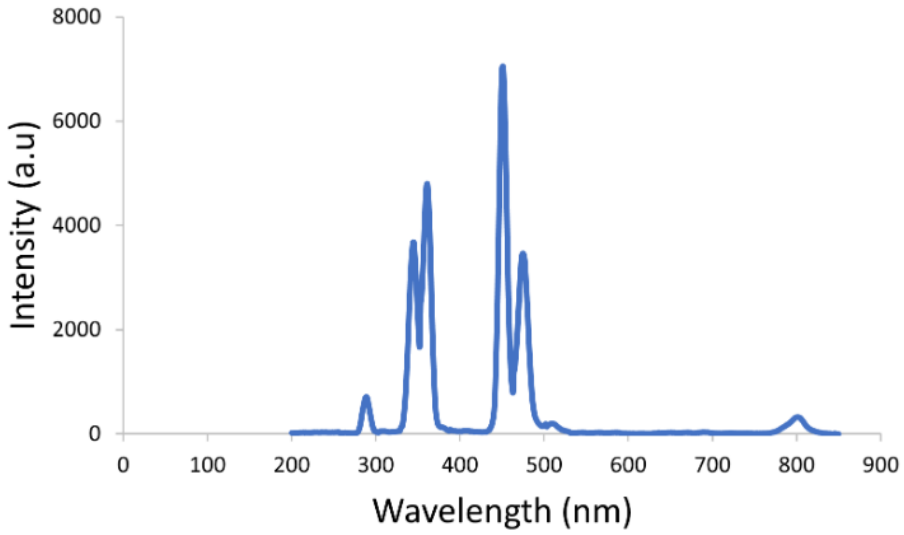


Figure 2.1: Emission spectrum of the water-dispersible $NaYF_4$:Yb,Tm upconverting nanoparticles used in this study. Data provided by CD Bioparticles[25].

2.4. Fabry–Pérot Optical Filter

2.4.1. Spectral Filtering Requirement

While the UCNPs generate the UV light required for NADH excitation, they also produce emission in the blue wavelength region[25, 29]. Since NADH also emits blue fluorescence after UV excitation, the blue emission generated directly by the UCNPs spectrally overlaps with the target NADH fluorescence signal. If this undesired blue light directly enters the photodetector, it will introduce an additional background signal and consequently reduce the selectivity and measurement accuracy of NADH fluorescence detection.

Therefore, a wavelength-selective optical filtering structure is required between the UCNP layer and the photodetector. The filter should suppress the blue emission generated by the UCNPs while maintaining a relatively high transmission in the UV wavelength range required for NADH excitation. In this way, the UV light can continuously propagate through the optical transmission region of the detector and reach the myocardial tissue underneath. Therefore, the optical filter plays an essential role in separating the excitation light pathway from the fluorescence detection pathway within the complete device.

2.4.2. Fabry–Pérot Multilayer Structure

A Fabry–Pérot (FP) multilayer dielectric filter is employed in this project to achieve the required wavelength selectivity. Such a filter consists of alternating dielectric thin films with different refractive indices, where multiple reflections and optical interference within the individual layers determine the transmission behavior at different wavelengths[17]. In the previous work, SiO_2 was selected as the

low-refractive-index material, while SiN was employed as the high-refractive-index material, thereby providing a sufficient refractive-index contrast for constructing the multilayer optical structure.

The optical response of the FP filter mainly depends on the refractive index and physical thickness of each individual layer[30]. By appropriately designing the multilayer structure, relatively high transmission can be obtained within the target UV wavelength range, while the undesired blue light can be strongly reflected or attenuated. The multilayer configuration adopted in the previous work is shown in Figure 2.2. Since the interference condition is highly sensitive to the optical thickness of each layer, even a relatively small deviation in film thickness may result in a shift of the transmission spectrum. Therefore, accurate control of the film thickness, refractive index, and layer-to-layer uniformity is important during the deposition process. For this reason, in the previous work, the actual deposition rates of SiO_2 and SiN were calibrated by ellipsometry before each complete FP filter fabrication process in order to reduce thickness deviations caused by variations in the deposition conditions.

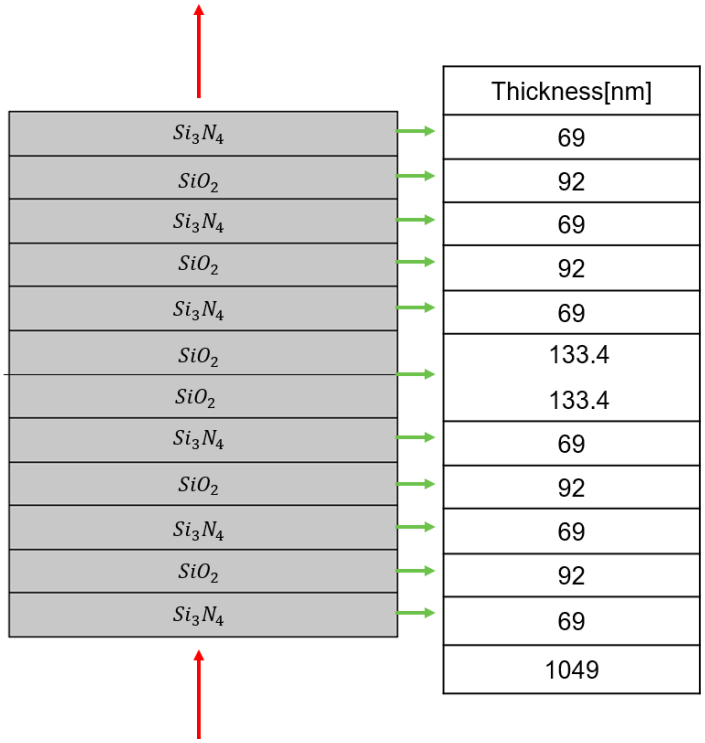


Figure 2.2: Multilayer structure and designed thicknesses of the Fabry–Pérot filter adopted in the previous work. Source: reproduced from the MSc thesis defense presentation of Haoxiang Jiang, TU Delft, 2025[31].

In addition to the thickness of the dielectric layers, the surface flatness of the underlying substrate can also influence the thickness uniformity of the deposited layers and consequently the final optical performance of the filter[30]. Therefore, within the complete device fabrication workflow, the FP filter is not only an optical functional layer but also places relatively strict requirements on the mechanical stability and surface flatness of the underlying silicon structure. This consideration is also one of the main reasons why an approximately 10 µm thick silicon optical transmission region is initially preserved during the fabrication process, while the final thinning step is postponed to a later stage of device integration. In this way, excessive mechanical stress and surface deformation of an ultrathin silicon membrane can be avoided during FP filter fabrication.

2.5. Silicon Photodetector and Backside Detection

2.5.1. Detector Architecture

A silicon-based photodetector is employed in this project to convert the blue fluorescence generated by NADH into an electrical signal. The detector mainly consists of a silicon substrate, a doped photosensitive region, dielectric layers, and metal electrodes. The photosensitive region is able to absorb the blue

fluorescence returning from the myocardial tissue and generate measurable electrical signals. The architecture of the silicon photodetector used in this study is illustrated in Figure 2.3.

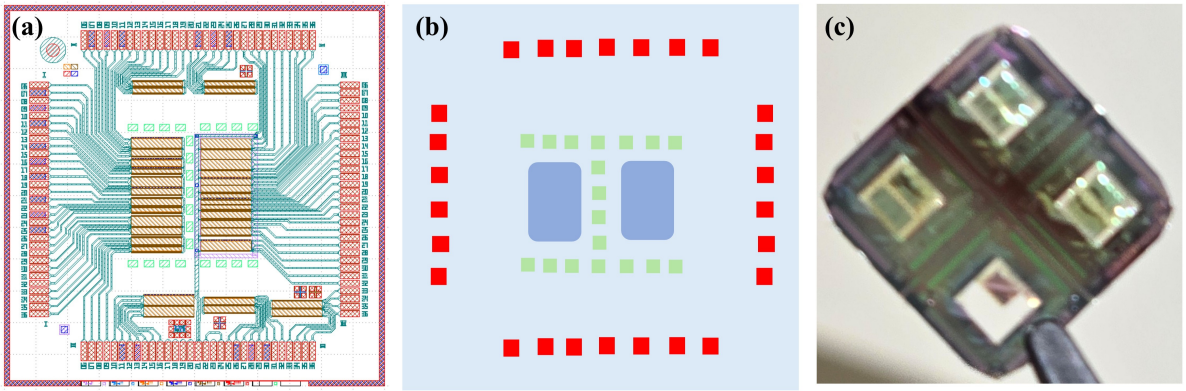


Figure 2.3: Silicon photodetector architecture used in this study. (a) Original layout of the detector. (b) Simplified schematic of the detector structure, highlighting the photosensitive regions (in red), thin optical regions (in green), and electrical contact pads (in dark blue). (c) Photograph of the fabricated chip containing four individual photodetectors arranged in a 2 × 2 configuration. Detector layout provided by the EI and ECTM group, TU Delft.

In addition to the photosensitive region, the detector also contains metal contact pads for electrical connection and signal readout. Since these contact pads need to remain accessible during device fabrication and final testing, the subsequently deposited optical filter, polymer, and protection layers cannot permanently cover these regions. Therefore, the later functional layers need to be patterned or selectively removed in order to preserve the required electrical contact windows.

2.5.2. Backside Detection

In the proposed device configuration, the external excitation light is incident from the top side of the device, while the target NADH fluorescence returns from the myocardial tissue located underneath the device. In order to prevent the externally incident light or stray light generated by the UCNPs from directly entering the photosensitive region from the front side of the detector, a backside detection configuration is employed.

For this purpose, a metal light-blocking layer is introduced above the photosensitive region on the front side of the detector to suppress optical signals arriving from the top side. In this way, the detector mainly receives the NADH blue fluorescence returning from the myocardial tissue and entering through the backside of the silicon substrate, thereby reducing direct optical interference from the excitation source above the device. Therefore, the front-side metal shielding structure and the backside detection configuration together establish a clear optical pathway within the device. The external light is mainly used to drive the UCNPs and generate the UV excitation light, while the target fluorescence returns from the myocardial side and is collected through the backside of the detector.

2.5.3. Thin Silicon Optical Window

Since the silicon substrate itself has a certain thickness, an excessively thick silicon region would significantly limit effective light propagation if light needs to enter from the backside or pass through the central region of the detector. Therefore, a locally thinned region is required in the detector to form an optical transmission window.

In the fabrication design of this project, this region is first thinned from the original silicon substrate to approximately 10 µm. This intermediate thickness provides sufficient mechanical strength and surface flatness during the subsequent FP filter deposition, photolithography, and device integration processes. After the major front-side functional layers have been integrated, the same region is further thinned to approximately 1 µm in order to improve the final optical transmission.

This stepwise thinning strategy reflects the trade-off between optical performance and mechanical stability. A thinner silicon membrane is beneficial for improving light transmission, but it also significantly reduces structural stiffness and increases the possibility of warping or local deformation

caused by residual or surface stress. For a Fabry–Pérot filter that relies on thin-film interference, an uneven underlying surface may result in local variations in film thickness and consequently influence the spectral response of the filter. Therefore, postponing the final thinning step to a later stage of device integration helps maintain suitable fabrication conditions for the FP filter while still enabling the required optical transmission window to be obtained in the final device.

2.6. Flexible Polymer Substrate

2.6.1. Requirements for a Flexible Supporting Layer

The final device is intended to directly contact continuously moving myocardial tissue. Therefore, its mechanical properties should not only satisfy the requirement of structural integrity, but should also minimize the mechanical mismatch between the device and the surrounding soft tissue[32, 33]. Compared with a rigid silicon substrate, a flexible polymer can provide better bendability and conformability, while simultaneously serving as a mechanical supporting and structural integration layer within the device[34, 35].

In this project, as the silicon optical transmission region is further thinned, the mechanical strength of the detector itself decreases significantly[36]. Therefore, an additional flexible material is required to support the complete integrated structure. This supporting layer should not only be sufficiently compliant, but should also remain compatible with the subsequent thin-film deposition, photolithography, and etching processes.

2.6.2. b-DCPU as the Polymer Substrate

b-DCPU is selected in this project as the flexible polymer substrate for the final device. This material belongs to a crosslinked polyurethane system, whose mechanical properties can be adjusted by controlling the precursor ratio and crosslinking degree[37, 38]. Meanwhile, micrometer-scale thin films can be prepared by spin coating.

In the final device stack, the b-DCPU layer is located above the UCNP layer and serves as the main flexible supporting layer, mechanically integrating the UCNPs, optical filter, and thinned silicon photodetector into a complete structure. Compared with relying only on an ultrathin silicon membrane, the polymer layer can improve the structural stability of the device during the subsequent release, transfer, and operation processes[37].

However, the introduction of the polymer also brings additional fabrication limitations. Compared with conventional inorganic microfabrication materials, polyurethane can be more sensitive to certain photoresists, solvents, and plasma treatments[39, 40]. Therefore, material compatibility needs to be carefully considered during the subsequent patterning process. This issue will be further discussed in the following chapters regarding the device integration and fabrication workflow.

2.6.3. Mechanical Compatibility

The mechanical compatibility between the flexible device and myocardial tissue cannot be evaluated only by the Young's modulus, E, of the material. For thin-film structures with a finite thickness, the overall tensile and bending responses are also strongly influenced by the geometrical dimensions[41].

For a rectangular film with a width w and thickness t, the axial stiffness can be expressed as

$$EA = Ewt, \tag{2.1}$$

while the flexural rigidity can be expressed as

$$EI = \frac{Ewt^3}{12}. \tag{2.2}$$

The film thickness plays an important role in determining the final mechanical response, particularly since the flexural rigidity is proportional to the third power of thickness. Even if the Young's modulus of the polymer itself is higher than that of myocardial tissue, reducing the film thickness

can significantly decrease the overall flexural rigidity of the structure and consequently improve its mechanical compliance.

Based on this consideration, tensile tests are performed in this project to obtain the stress–strain relationship and Young's modulus of b-DCPU. The measured modulus is further combined with the designed film thickness to calculate the corresponding EA and EI, which are used to evaluate the mechanical compatibility between the polymer supporting layer and myocardial tissue[34, 41].

2.7. Fabrication Challenges for Device Integration

Integrating the photodetector, metal light-blocking layer, Fabry–Pérot filter, UCNPs, and flexible polymer into a single device requires not only maintaining the performance of each individual functional layer, but also considering the fabrication compatibility between different materials. Since these materials respond differently to temperature, chemical reagents, plasma treatment, and mechanical stress, a process suitable for one layer may negatively influence structures that have already been fabricated. Therefore, arranging the fabrication sequence in a reasonable way is an essential requirement for realizing the final device.

2.7.1. Heterogeneous Material Compatibility

The final device contains multiple types of materials, including metals, inorganic dielectrics, nanoparticles, silicon, and organic polymers. These materials differ significantly in their allowable deposition temperatures, etching conditions, and chemical treatments. For example, inorganic SiO_2 and SiN thin films can generally withstand relatively strong plasma treatment, while flexible polymers are more sensitive to solvents, elevated temperatures, and reactive plasma environments. Therefore, during the fabrication of subsequent layers, thermal damage, chemical degradation, or interfacial delamination of the already completed functional structures need to be avoided.

In addition, residual stress between different layers may also influence the overall device structure[42]. For a relatively thick silicon substrate, such stress generally does not cause significant deformation. However, as the silicon optical transmission region is further thinned, thin-film stress may induce local warping, which can subsequently affect the surface flatness and thickness uniformity of the multilayer optical films deposited above. Therefore, material compatibility in the integrated device involves not only chemical and thermal stability, but also the mechanical interaction within the complete multilayer structure.

2.7.2. Polymer–Photolithography Compatibility

Conventional microfabrication processes usually rely on photoresist for pattern definition. However, flexible polymers may interact unfavorably with the photoresist itself as well as the associated solvents, developers, or resist-removal chemicals. Direct photolithography on the polymer surface may lead to swelling, changes in surface properties, or local degradation of the polymer, which can further influence film integrity and subsequent device performance.

Therefore, an additional protection strategy is required when patterning structures on the polymer surface. In this project, an inorganic SiN thin film is introduced as an isolation layer between the b-DCPU polymer and the photoresist, preventing direct contact between the polymer and the photolithography chemicals. Meanwhile, the SiN layer can also serve as a protection layer or hard mask during the subsequent etching process, thereby improving the controllability of polymer patterning.

2.7.3. Polymer Dry Etching

In order to define the final device geometry and reopen regions that need to remain exposed, the b-DCPU layer requires selective etching. For organic polymers, oxygen-containing plasma is commonly used to remove carbon-based materials through oxidation reactions that convert the polymer into volatile products. However, for highly crosslinked polymer systems, plasma treatment may simultaneously induce surface oxidation, further crosslinking, or the formation of non-volatile residues, causing the actual etching behavior to deviate from the ideal case.

Therefore, polymer dry etching requires not only a sufficient etching rate, but also control over residue formation, surface damage, and mask selectivity. For the present project, establishing a stable b-DCPU

dry-etching process capable of producing a clean etched surface is one of the important fabrication steps required for complete device integration.

2.7.4. Temporary Bonding and Thin-Device Handling

As the thickness of the silicon optical transmission region is reduced, the mechanical strength of the device decreases significantly, making it more susceptible to fracture or deformation during spin coating, thin-film deposition, photolithography, and etching. Therefore, a carrier wafer is generally required during the later fabrication stages to provide temporary mechanical support, while a temporary bonding material is used to fix the device onto a larger and more rigid substrate.

This approach can improve the handling stability of the thin device inside fabrication equipment and reduce the risk of damage caused by mechanical loading during processing. However, the temporary bonding material itself must also remain compatible with the subsequent thermal and chemical treatments. Meanwhile, it needs to be removed reliably after fabrication without damaging the previously completed structures. Therefore, the bonding and release steps must also be considered as part of the overall fabrication sequence.

2.7.5. Electrical Pad Accessibility

In addition to the optical and mechanical requirements, the metal contact pads of the detector must remain accessible throughout the fabrication process in order to enable final electrical connection and signal readout. However, the subsequently deposited filter, polymer, and protection layers are generally formed over relatively large areas and may easily cover the existing metal contact pads.

Therefore, after the deposition of each functional layer, a corresponding patterning or opening step needs to be considered in order to ensure that the contact pads remain exposed in the final device. This requirement indicates that device integration cannot simply follow the final stacking order through sequential layer deposition. Instead, the spatial separation between the optical region, photosensitive region, and electrical contact region must be considered throughout the complete fabrication process.

Overall, the fabrication of the complete device represents a multi-material and multi-process integration problem in which different fabrication steps are strongly coupled with each other. The final fabrication workflow must simultaneously satisfy the requirements of optical transmission, spectral selectivity, mechanical support, material compatibility, and electrical accessibility. Therefore, compared with individually optimizing the UCNPs or the optical filter, the present study further focuses on how these functional components can be integrated into a complete device through an appropriate fabrication sequence, while identifying and addressing the key processing limitations that arise during device integration.

2.8. Research Gap and Objective

Previous studies have separately demonstrated the feasibility of using UCNPs for wavelength conversion from long-wavelength excitation to UV emission and established a Fabry–Pérot filter design capable of suppressing the blue emission generated by the UCNPs while maintaining UV transmission. Meanwhile, the silicon-based photodetector, locally thinned optical transmission region, and flexible polymer substrate individually provide the basic functions required for the final implantable optical sensing platform. However, when these components are integrated into a single device, additional fabrication challenges arise that are not present when the individual functional layers are prepared separately.

These challenges mainly originate from the mutual limitations between different materials and fabrication steps. For example, the FP filter requires a relatively flat supporting surface and accurate control of individual layer thicknesses, while thinning the silicon optical transmission region to its final thickness at an early fabrication stage may introduce structural deformation. The polymer can provide flexible mechanical support, but it is more sensitive to conventional photoresists and certain chemical treatments. Subsequent polymer patterning also requires a stable dry-etching process, while the formation of residues that are difficult to remove needs to be avoided. In addition, the metal contact pads of the detector must remain accessible throughout the integration process, whereas the UCNPs, optical filter, and polymer layers need to cover specifically defined optical regions. Therefore, realization of the

final device depends on a fabrication workflow that can simultaneously satisfy the optical, electrical, mechanical, and material-compatibility requirements.

Based on these considerations, the main objective of this study is to develop and evaluate a microfabrication workflow for integrating the silicon photodetector, metal light-blocking layer, Fabry–Pérot filter, UCNP layer, and b-DCPU flexible polymer substrate into a complete device. The main focus is placed on the compatibility between individual fabrication steps and the practical problems encountered during device processing, rather than on revalidating the fundamental working mechanisms of the UCNPs or the optical filter.

More specifically, this study focuses on the following aspects:

1. Integrating the front-side metal light-blocking structure and Fabry–Pérot filter onto the silicon photodetector while maintaining the accessibility of the metal contact pads and the functionality of the detector.
2. Further integrating the UCNP layer and b-DCPU flexible polymer substrate onto the existing optical structure while providing sufficient mechanical support for the complete device.
3. Addressing the material compatibility between b-DCPU and conventional photolithography processes, and establishing suitable protection and etching strategies for polymer patterning.
4. Arranging the sequence of silicon thinning, temporary bonding, polymer processing, and final device release in order to obtain the required optical transmission region while maintaining the surface flatness of the FP filter and the structural stability of the device.
5. Identifying the major limitations of the current fabrication workflow and providing a process basis for the subsequent completion of the final device and complete NADH optical detection.

Therefore, this study can be considered as a bridge between the previous development of individual optical components and the realization of a complete integrated device. Its main contribution is to advance the system from the verification of separate functional layers toward device-level integration under multi-material and multi-process fabrication conditions.

3 Methods

This chapter describes the fabrication and characterization methods used to integrate the optical, mechanical, and electronic components of the proposed sensing platform. The process flow was developed to account for the compatibility constraints between the silicon photodetector, dielectric optical layers, UCNPs, flexible polymer substrate, and subsequent lithography and etching steps.

The chapter first introduces the final device architecture and overall fabrication workflow, followed by the individual processing steps in the order in which they are implemented. The final sections describe the planned backside processing and the characterization methods used to evaluate the fabricated structures and materials.

3.1. Integrated Device Design

Before describing the individual fabrication steps, the overall device architecture and working principle are introduced in this section. The purpose is to define the functional role and relative position of each layer and to establish the fabrication sequence required for subsequent integration.

3.1.1. Final Device Architecture

The final device adopts a multilayer integrated structure consisting of a silicon-based photodetector, Mo light-blocking layer, Fabry–Pérot (FP) filter, UCNP layer, b-DCPU flexible polymer substrate, and SiN protection layer. These functional layers are sequentially stacked along the thickness direction and serve different purposes, including photodetection, optical shielding, spectral filtering, wavelength conversion, mechanical support, and process protection[18]. Moreover, soft implantable bioelectronic systems benefit from mechanically compliant and thin device structures that reduce the mechanical mismatch between conventional rigid electronics and soft biological tissues and improve conformal contact with the target tissue [32, 33, 35]. The integration of wavelength-selective thin-film optical filters with silicon photodetectors has previously been demonstrated for fluorescence-based bioelectronic sensing, providing a basis for combining spectral filtering and photodetection within a compact device architecture [18].

The overall multilayer configuration of the proposed device is illustrated in Figure 3.1.

From top to bottom, the device consists of an approximately 90 nm thick SiN protection layer, an approximately 15 µm to 25 µm thick b-DCPU polymer layer, an approximately 1 µm thick UCNP layer, an approximately 1 µm thick FP filter, an approximately 200 nm thick Mo light-blocking layer, and the silicon-based photodetector. A locally thinned optical transmission region is formed within the detector to establish an optical pathway from the top side of the device toward the myocardial tissue underneath. Meanwhile, peripheral metal contact pads are preserved for subsequent electrical connection and signal readout.

Reducing the thickness of crystalline silicon is an established strategy for increasing its flexibility and enabling mechanically compliant electronic structures, although thinner silicon also becomes increasingly sensitive to mechanical handling and deformation [36]. In the present design, local thinning is therefore restricted to the optical transmission region while the surrounding silicon is retained for mechanical support.

3.1.2. Optical Working Principle

The device employs a top-to-bottom excitation pathway together with a fluorescence detection pathway returning from the myocardial tissue toward the photodetector.

Lanthanide-doped UCNPs enable the conversion of lower-energy NIR excitation into shorter-wavelength emission through sequential energy-transfer processes [14, 26]. In particular, Nd^{3+}-sensitized UCNP

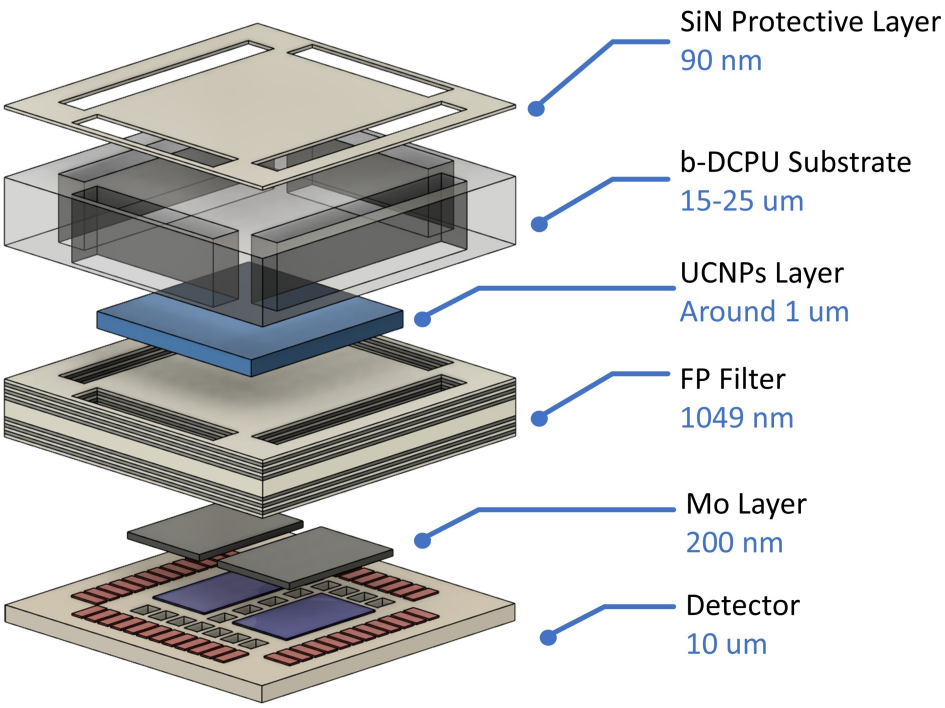


Figure 3.1: Exploded schematic of the final integrated device architecture developed in this study, showing the SiN protection layer, b-DCPU flexible polymer substrate, UCNP layer, Fabry–Pérot optical filter, Mo light-blocking layer, and silicon-based photodetector, together with their nominal design thicknesses.

systems enable excitation near 808 nm, where water absorption and the associated heating effect are reduced compared with conventional 980 nm excitation [23]. The external red or near-infrared (NIR) light first passes through the SiN and b-DCPU layers and reaches the UCNP layer, where it is converted into UV and blue light. The core–shell UCNPs used in this study are specified by the supplier to exhibit emission near 365 nm and 475 nm under 808 nm excitation [25].

Since the blue emission generated by the UCNPs spectrally overlaps with the NADH fluorescence signal, it is suppressed by the FP filter. Meanwhile, the UV light continues to propagate through the filter and the optical transmission region of the detector, eventually reaching the myocardial tissue underneath. The spectral transmission of a Fabry–Pérot multilayer structure is governed by the optical thickness and refractive-index contrast of its constituent layers, allowing selected wavelength bands to be transmitted while others are suppressed [17, 30]. This wavelength-selective filtering principle is used here to separate the desired UV excitation pathway from the undesired blue UCNP emission.

After excitation by the UV light, NADH in the myocardial tissue emits blue fluorescence. Part of this fluorescence propagates back toward the device and is collected by the photosensitive region from the backside of the detector, where it is converted into an electrical signal. Meanwhile, the Mo layer located on the front side of the photodetector blocks light that would otherwise directly enter the photosensitive region from the top side of the device, thereby reducing interference from the external excitation light and other undesired optical signals. Suppression of excitation light before photodetection is an important requirement in fluorescence-based optical sensing, since residual excitation light can otherwise contribute directly to the photodetector response and reduce the selectivity of fluorescence detection [18].

3.1.3. Overall Fabrication Workflow

The overall fabrication strategy of the proposed device is illustrated in Figure 3.2. Instead of following the final layer stack in a simple sequential manner, the process was designed to balance optical functionality, material compatibility, and structural stability during integration. This consideration is particularly important for soft implantable systems, in which mechanically dissimilar inorganic electronic or optical components must be combined with compliant polymeric materials while maintaining device integrity

and tissue compatibility [32, 33, 35].

The fabrication starts from a silicon photodetector with exposed peripheral contact pads. A Mo light-blocking layer and Fabry–Pérot (FP) filter are then deposited and patterned on the detector to provide wavelength-selective transmission. Because the optical response of multilayer interference filters is strongly dependent on the optical thickness of the deposited layers, accurate deposition and thickness control are required to reproduce the intended spectral response [17, 30].

After completion of the filter structure, a UCNP layer is deposited on top as the local wavelength conversion medium. The flexible polymer substrate is subsequently formed above the UCNP layer to provide mechanical support for the integrated device. Crosslinked polyurethane systems based on polycaprolactone-derived components have previously been investigated as soft and biodegradable materials for biomedical applications [38], while dynamic covalent polyurethane materials have also been demonstrated as soft, bioresorbable substrates and encapsulation layers for implantable electronic devices [37].

To enable further polymer patterning without exposing the polymer directly to photolithography chemicals, a SiN protection layer is deposited on the polymer surface and later patterned to define the required device geometry.

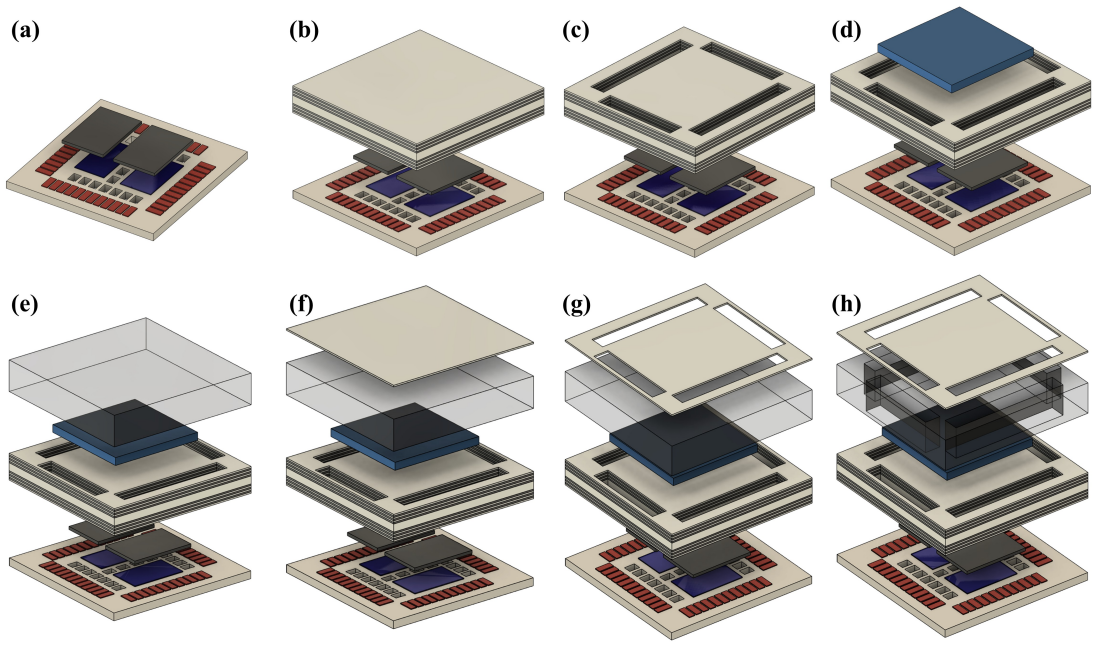


Figure 3.2: Schematic overview of the device fabrication workflow. (a) Starting silicon photodetector with the front-side Mo light-blocking structure. (b–c) Deposition and patterning of the Fabry–Pérot filter. (d) Deposition of the UCNP layer. (e) Coating of the b-DCPU polymer supporting layer. (f–g) Deposition and patterning of the SiN protection layer for subsequent polymer processing. (h) Resulting integrated multilayer structure prior to the remaining backside thinning and final release steps.

Through this process sequence, the optical, mechanical, and fabrication requirements of the different functional layers can be integrated into a single device structure. The workflow also reflects an important design principle of this study: process order is not determined only by the final stacking arrangement, but also by the compatibility constraints between the constituent materials and the need to preserve electrical access and structural integrity throughout fabrication.

3.2. Starting Detector and Pre-processing

The fabrication process starts from a prefabricated silicon photodetector that has already undergone initial backside thinning and selected dielectric-layer removal. This section describes the starting detector structure and the pre-processing steps that establish the platform for subsequent front-side integration.

3.2.1. Initial Detector Structure

A prefabricated silicon-based photodetector is used in this study as the starting platform for subsequent device integration. The main body of the detector is based on p-type silicon and contains the photosensitive region for photoelectric conversion, a locally defined optical transmission region, doped regions, and peripheral metal contact pads. The metal contact pads are used for subsequent electrical connection and signal readout and therefore need to remain accessible throughout the complete fabrication process.

The detector surface also contains dielectric layers, including SiO_2 and SiN, which provide electrical insulation, passivation, and surface protection. A locally defined optical transmission structure is located in the central region of the detector, providing the optical pathway required for the subsequent UV light to pass through the detector and reach the myocardial tissue underneath. In this thesis, the term *optical transmission window* refers to this locally thinned silicon region rather than to a completely open aperture. Its purpose is to reduce the optical path length through silicon while retaining the surrounding detector structure for mechanical support.

3.2.2. Initial Backside Thinning

Before the device integration work carried out in this study, an initial backside thinning process had already been performed on the detector. The original silicon substrate had a thickness of approximately 290 µm. Through tetramethylammonium hydroxide (TMAH) wet etching, the central optical transmission region was thinned to approximately 10 µm, while the surrounding silicon remained relatively thick to provide mechanical support.

Reducing the thickness of crystalline silicon is an established approach for increasing its flexibility, biodegradability and enabling mechanically compliant electronic structures. However, as the silicon thickness decreases, the structure also becomes increasingly sensitive to mechanical handling, bending, and residual stress [36]. Retaining thicker silicon around the locally thinned region therefore provides additional structural support during subsequent processing. This intermediate thickness does not represent the final design thickness. Instead, it was intentionally preserved in order to maintain sufficient mechanical stability and surface flatness during the subsequent metal deposition, FP filter fabrication, and other front-side processing steps. This process strategy is consistent with the mechanical behaviour of ultrathin silicon structures, for which decreasing thickness substantially reduces bending stiffness and increases susceptibility to deformation [36]. Maintaining an intermediate silicon thickness during front-side fabrication therefore reduces the risk that deformation of the locally thinned region influences subsequent thin-film processing. The optical transmission region is further thinned to its final thickness during a later stage of device integration.

3.2.3. Dielectric Layer Removal

After the initial thinning process, selected SiN and TEOS SiO_2 layers on the detector surface are removed in order to open the regions required for subsequent device integration. The SiN and SiO_2 layers are selectively removed through the corresponding dry- and wet-etching processes, while the dielectric structures required for normal detector operation are preserved.

After these pre-processing steps, the detector provides a suitable initial structure for the integration of the subsequent functional layers, while the peripheral metal contact pads remain exposed. This pre-processed detector therefore serves as the starting platform for the subsequent integration of the Mo light-blocking layer, Fabry–Pérot filter, UCNP layer, and flexible polymer substrate.

3.3. Front-Side Optical Shielding

A front-side light-blocking structure is required to reduce direct optical interference with the photosensitive regions during backside detection. This section describes the design, lithographic definition, deposition, and lift-off of the Mo shielding layer while maintaining access to the peripheral contact pads.

3.3.1. Design of the Light-Blocking Layer

Since the device operates in a backside detection configuration, the externally incident light should not directly enter the photosensitive region from the front side of the detector. Otherwise, an additional

background signal may be generated and interfere with the subsequent detection of NADH fluorescence. In fluorescence-based silicon photodetection systems, suppression of the excitation light before it reaches the photosensitive region is important because residual excitation light can contribute directly to the detector response and reduce the selectivity of the fluorescence measurement [18]. Therefore, a metal light-blocking layer is introduced above the photosensitive region on the front side of the detector to suppress direct illumination from the top side of the device.

Mo is selected in this study as the light-blocking material and is patterned only over the photosensitive region that requires optical shielding. Meanwhile, the peripheral metal contact pads are kept exposed in order to ensure that the subsequent electrical connection and signal readout are not affected. The patterned configuration therefore provides local optical shielding while preserving the electrical access required for later device characterization and signal readout.

3.3.2. Photolithography

The Mo pattern is defined by a photolithography process. First, S1813 positive photoresist is spin-coated on the detector surface. After soft baking, exposure, and development, openings are formed at the positions where the Mo layer needs to be retained. The photomask is also designed to avoid the peripheral metal contact pads, thereby ensuring that these regions are not permanently covered during the subsequent deposition process.

3.3.3. Mo Deposition

After photolithography, an approximately 200 nm thick Mo layer is deposited onto the sample surface. Since the non-target regions are covered by photoresist, Mo is directly deposited only onto the predefined openings as well as onto the surface of the remaining photoresist.

3.3.4. Lift-Off

After Mo deposition, the remaining photoresist together with the metal deposited on top of it is removed through a lift-off process. As a result, only the Mo light-blocking structure located above the front-side photosensitive region remains. After this step, the photosensitive region on the front side of the detector is effectively shielded, while the peripheral contact pads remain exposed, providing the required starting condition for the subsequent integration of the Fabry–Pérot filter.

3.4. Fabry–Pérot Filter Integration

The Fabry–Pérot filter is integrated after formation of the Mo light-blocking structure to provide the required wavelength-selective transmission. This section describes the deposition-rate calibration, multilayer deposition, and subsequent patterning of the SiO_2/SiN filter while preserving the required optical and electrical regions.

3.4.1. Selected Filter Structure

The Fabry–Pérot (FP) filter used in this study follows the previously established SiO_2/SiN multilayer design and is integrated directly onto the detector after fabrication of the Mo light-blocking layer. The optical design itself was established in previous work, while the present study focuses on reproducing the designed multilayer structure and integrating it within the complete detector fabrication sequence [31]. In multilayer interference filters, wavelength-selective transmission is determined by the refractive indices and optical thicknesses of the constituent dielectric layers. Consequently, deviations in individual layer thickness can shift the spectral response away from the intended design [17, 30].

The total designed thickness of the multilayer stack is approximately 1 µm. The fabrication process therefore focuses on reproducing the predefined layer thicknesses, patterning the FP filter within the optical functional region, and maintaining access to the peripheral metal contact pads[31].

3.4.2. Deposition Rate Calibration and Multilayer Deposition

Both SiO_2 and SiN are deposited by ICPECVD. Because the spectral response of the FP filter depends directly on the optical thickness of each dielectric layer, accurate control of the deposited film thickness is required during fabrication [17, 30]. Deposition-rate calibration was therefore performed before fabrication of the complete multilayer stack.

Before deposition of the complete FP filter, the chamber is conditioned and short calibration depositions are performed for both dielectric materials. The thicknesses of the calibration films are measured by ellipsometry, and the deposition times are adjusted according to the measured deposition rates. In this way, the experimentally determined deposition rates are used to convert the predefined optical design into the corresponding process times for the individual SiO_2 and SiN layers. After calibration, the SiO_2 and SiN layers are sequentially deposited according to the predefined multilayer sequence. The calibrated deposition process is first evaluated on a glass substrate and is subsequently applied to the detector sample to form the complete SiO_2/SiN multilayer stack[31].

3.4.3. Filter Patterning and Dry Etching

After deposition of the multilayer stack, photolithography is performed to define the optical functional region in which the FP filter should remain. The patterned photoresist serves as the etching mask, protecting the optical functional region while exposing the multilayer stack above the peripheral metal contact pads and other areas to be removed.

The exposed SiO_2/SiN multilayer stack is subsequently patterned by dry etching. For successful pattern transfer, the etching process must remove the complete dielectric stack from the exposed regions while retaining sufficient photoresist thickness to protect the filter region throughout the etch. Because the etching behavior of the dielectric multilayer differs from that of the photoresist mask, etching tests are carried out to evaluate both removal of the multilayer stack and consumption of the photoresist. Different plasma chemistries are compared to determine suitable process conditions for complete pattern transfer while maintaining sufficient mask selectivity.

The final plasma chemistry is therefore selected experimentally on the basis of the relative removal of the dielectric stack and the photoresist mask, rather than being adopted directly from the optical filter design. Endpoint monitoring is used during the dry etching process to assist in determining when the exposed multilayer stack has been sufficiently removed.

3.4.4. Photoresist Removal and Pad Reopening

After completion of the dry etching process, the remaining photoresist is removed and the sample is cleaned. The FP filter is retained within the optical functional region, while the multilayer stack above the peripheral metal contact pads is removed, thereby reopening the pads for subsequent electrical connection. This selective patterning is required to preserve the optical function of the filter while maintaining electrical access to the detector, illustrating the need to consider both optical and electrical requirements during integration. The patterned FP filter then provides the surface for the subsequent UCNP deposition process.

3.5. UCNP Deposition

After completion of the Fabry–Pérot filter, the UCNP layer is deposited to provide local wavelength conversion from the external excitation light to UV emission. This section describes the deposition approach and the process parameters considered for controlling the particle distribution, deposition area, and layer thickness.

3.5.1. UCNP Material

The upconverting nanoparticles previously selected and validated in the earlier project are employed in this study as the wavelength conversion material. Lanthanide-doped UCNPs are widely used for converting lower-energy NIR excitation into shorter-wavelength emission, while core–shell structures can reduce surface-related non-radiative quenching and improve the optical response of the nanoparticles [14, 26].

The nanoparticle system used in the present work was therefore not redesigned, but adopted from the previously established device concept [31]. The UCNPs are used in the form of an aqueous suspension and are subsequently deposited onto the surface of the Fabry–Pérot filter, where they form the optical wavelength conversion region in the final device. They are specified to exhibit characteristic emission near 365 nm and 475 nm under 808 nm excitation, corresponding to the UV excitation pathway and the additional blue emission considered in the device design [25].

Since the main focus of this study is device integration, different UCNP compositions are not compared again. Instead, the nanoparticle system and the basic handling procedure established in the previous work are directly adopted. Accordingly, the UCNP-related process development in this study focuses on deposition and integration rather than on optimization of the nanoparticle composition or upconversion mechanism.

3.5.2. Suspension Preparation

UCNPs show a certain tendency to agglomerate in aqueous suspension and therefore need to be redispersed before deposition. Because particle aggregation in a colloidal suspension can lead to a non-uniform particle distribution after solvent evaporation, maintaining a reproducible dispersion state is important for controlling the morphology of the deposited UCNP layer. Ultrasonic treatment and mixing are applied to disperse the particles as uniformly as possible in the solution, and the subsequent deposition is performed before significant particle sedimentation occurs.

According to the experimental requirements, the UCNP suspension is adjusted to the required concentration. The same redispersion procedure is maintained before each deposition in order to improve the reproducibility between different samples. These procedures are therefore used as process-control measures to reduce sample-to-sample variation before the subsequent drop-casting step.

3.5.3. Drop-Casting Process

The UCNP layer is deposited onto the patterned Fabry–Pérot filter surface by drop casting. Compared with spin coating, drop casting can reduce particle loss during rotational spreading and is more suitable for obtaining a relatively high particle loading within a defined deposition area[31]. This localized deposition approach is particularly suitable for the present device because the UCNPs are required only within the optical functional region, rather than as a continuous coating over the complete detector surface.

After deposition, the sample is dried under controlled conditions, allowing the UCNPs to remain on top of the filter and form a continuous functional layer. Since solvent evaporation influences particle transport and redistribution during drying, the drying condition is treated as an important process parameter for controlling the final lateral distribution and thickness uniformity of the UCNP deposit. This UCNP layer serves as the local wavelength conversion region within the device and provides the surface basis for the subsequent integration of the polymer substrate.

3.6. Temporary Bonding

The locally thinned detector requires additional mechanical support before subsequent vacuum-assisted spin-coating and lithographic processes. This section describes the temporary bonding strategy used to fix the device onto a rigid carrier wafer and improve handling stability during further fabrication.

3.6.1. Purpose of Temporary Bonding

Temporary bonding is introduced at an early stage of the fabrication process, before the first photolithography step. The pre-processed silicon photodetector contains a locally thinned region and is therefore mechanically more fragile than a conventional bulk silicon substrate. As the thickness of crystalline silicon is reduced, its bending stiffness decreases substantially and the structure becomes increasingly sensitive to handling, bending, and externally applied mechanical loads [36].

During photoresist spin coating, the sample needs to be fixed onto the spin coater by vacuum suction. Directly applying the vacuum force to the thinned detector may increase the risk of cracking or fracture, particularly within the locally thinned silicon region. For this reason, mechanical support is introduced before the first vacuum-assisted processing step rather than only after completion of the front-side optical layers. To prevent mechanical failure during spin coating and subsequent handling, the detector is temporarily bonded onto a larger rigid carrier wafer before fabrication of the Mo light-blocking layer. The carrier wafer provides mechanical support and allows the sample to be securely held by the vacuum chuck without directly loading the fragile detector.

In this configuration, the carrier wafer temporarily restores a mechanically robust handling platform while the locally thinned detector remains attached, allowing conventional lithographic and thin-film

processing steps to be performed without making the carrier part of the final device. The temporarily bonded configuration is maintained during the following front-side fabrication steps until the device needs to be released for the final backside processing.

3.6.2. Crystalbond 555 Bonding

Crystalbond 555 is used as the temporary bonding material to attach the pre-processed detector to a rigid carrier wafer. The bonding material softens upon heating, allowing the detector to be positioned and bonded to the carrier surface. After cooling, the adhesive solidifies and provides sufficient mechanical support for subsequent spin coating, photolithography, thin-film deposition, and related processing steps.

The use of a removable thermoplastic bonding layer allows the detector to be mechanically supported during front-side processing while still permitting subsequent release for backside access. The temporary bonding layer serves only as a mechanical support during fabrication and is not part of the final device structure. After completion of the required front-side integration processes, the detector is released from the carrier wafer and re-mounted when necessary for the final backside processing.

3.7. b-DCPU Polymer Preparation and Deposition

The b-DCPU layer provides the flexible mechanical support required for the final integrated structure. Soft and bioresorbable polyurethane-based materials have been developed for implantable bioelectronic systems because their mechanical compliance can help reduce the mismatch between rigid electronic components and soft biological tissues while providing temporary structural support [32, 35, 37].

This section describes the preparation of the polymer from its precursors, its deposition by spin coating, and the subsequent curing process used to form the supporting layer.

3.7.1. b-DCPU Synthesis

Bioresorbable dynamic covalent polyurethane (b-DCPU), formed through the reaction between polycaprolactone triol (PCL-triol) and hexamethylene diisocyanate (HDI), is employed in this study as the flexible polymer substrate [37]. Polyurethane networks based on PCL-derived polyols and HDI have previously been investigated as biodegradable and mechanically compliant materials for biomedical applications [38].

The ratio between the two precursors is calculated according to the target crosslinking degree in order to obtain suitable mechanical properties and processability for device support. PCL-triol and HDI are weighed according to the calculated ratio and subsequently mixed under magnetic stirring at approximately 60 °C, allowing the two components to be sufficiently mixed and undergo the crosslinking reaction. The hydroxyl groups of PCL-triol react with the isocyanate groups of HDI to form urethane linkages, resulting in the formation of a crosslinked polyurethane network [37, 38]. The resulting network structure provides the basis for the mechanical integrity of the polymer film and allows its stiffness and handling properties to be adjusted through the precursor ratio and curing conditions.

After completion of the reaction, the mixture is allowed to rest until most of the internal bubbles disappear, thereby reducing the possibility of forming voids or surface defects during the subsequent spin-coating process. The b-DCPU is then spin-coated onto the device surface to cover the central functional structures and form a continuous flexible supporting layer. Because the mechanical response of the final flexible structure depends not only on the intrinsic modulus of the polymer but also strongly on the film thickness, thickness control is an important design parameter for achieving the required mechanical compliance [32, 41].

The final film thickness is controlled by adjusting the spin speed, coating time, and amount of polymer applied, with a target thickness of approximately 15 µm to 25 µm. After that, the polymer is subsequently cured to obtain sufficient mechanical stability and to provide a stable surface for the following SiN protection-layer deposition and polymer patterning processes. The specific spin-coating and curing conditions used in this study are treated as process parameters to be optimized experimentally rather than as fixed values taken directly from the literature.

The overall b-DCPU preparation, deposition, and curing process is schematically illustrated in Figure 3.3.

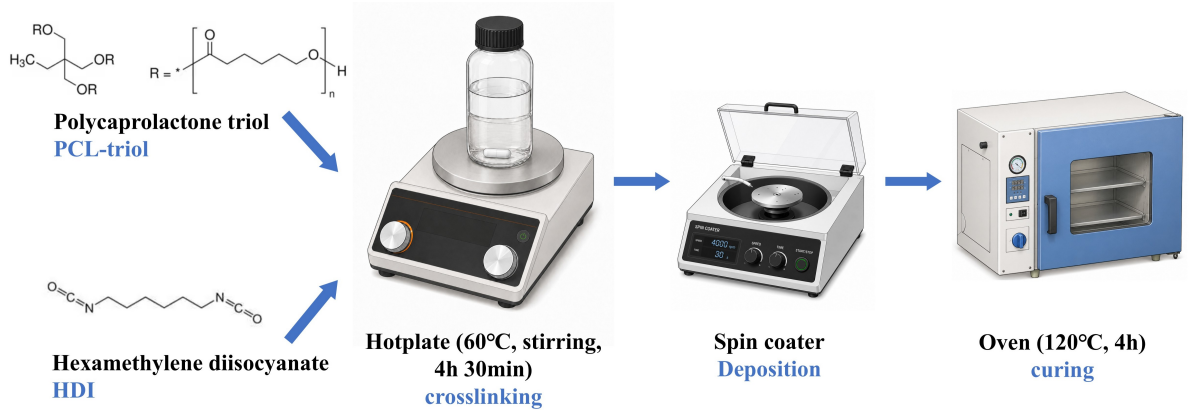


Figure 3.3: Schematic overview of the b-DCPU preparation and deposition process. Polycaprolactone triol (PCL-triol) and hexamethylene diisocyanate (HDI) are mixed and stirred, followed by spin coating of the resulting polymer mixture onto the device surface and thermal curing.

3.7.2. Polymer Thickness Measurement

After curing of the b-DCPU layer, the film thickness is measured in order to confirm whether it satisfies the device design requirements. The measured thickness is also used in the subsequent mechanical analysis, since the thickness of the polymer layer directly influences the axial stiffness and flexural rigidity of the final device.

For thin flexible structures, the tensile rigidity scales with thickness, whereas the flexural rigidity exhibits a stronger thickness dependence. This makes film thickness a critical parameter when comparing the mechanical compatibility of the polymer-supported device with cardiac tissue [41].

3.8. Mechanical Characterization of b-DCPU

The suitability of b-DCPU as a flexible supporting substrate depends on both its intrinsic material properties and the thickness of the fabricated film. This section describes the tensile-testing procedure and the calculation of Young's modulus, tensile rigidity, and flexural rigidity used to evaluate its mechanical compatibility with myocardial tissue.

3.8.1. Tensile Testing

In order to evaluate the mechanical properties of b-DCPU as a flexible supporting layer, dogbone-shaped specimens are prepared for tensile testing. The specimen geometry is designed according to the requirements of the tensile testing equipment and the available thin-film fabrication conditions. All specimens are fabricated from the same batch of polymer film in order to minimize material variations between different samples.

Tensile testing is performed to obtain the force–displacement response of b-DCPU, which is further converted into a stress–strain curve. During the measurement, the tensile force applied to the specimen and the corresponding displacement are recorded. The engineering stress and engineering strain are subsequently calculated according to the initial gauge length, width, and thickness of the specimen:

$$\sigma = \frac{F}{A}, \tag{3.1}$$

$$\varepsilon = \frac{\Delta L}{L_0}, \tag{3.2}$$

where F is the applied tensile force, A is the initial cross-sectional area of the specimen, ΔL is the change in gauge length, and L_0 is the initial gauge length.

3.8.2. Young's Modulus

The Young's modulus, E, is obtained by fitting a selected linear region of the stress–strain curve:

$$E = \frac{d\sigma}{d\varepsilon}. \tag{3.3}$$

This parameter is used to characterize the intrinsic material stiffness of b-DCPU and provides the basis for the subsequent calculation of the structural mechanical properties of the polymer layer. For thin and flexible bioelectronic structures, however, the Young's modulus alone does not fully describe the mechanical response of the integrated device, because the effective tensile and bending stiffness also depend strongly on the geometry and thickness of the supporting layer [32, 41].

3.8.3. Tensile and Flexural Rigidity

In addition to the Young's modulus, the tensile rigidity, EA, and flexural rigidity, EI, are further employed in this study to evaluate the overall mechanical response of the polymer thin film[37, 41]. Structural mechanical parameters such as tensile and flexural rigidity are particularly relevant for cardiac interfaces, because they reflect the combined effects of material stiffness and device geometry and therefore provide a more direct measure of the mechanical loading imposed by a thin-film structure [32, 41].

For a rectangular cross-section with a width w and thickness t,

$$EA = Ewt, \tag{3.4}$$

and

$$EI = \frac{Ewt^3}{12}. \tag{3.5}$$

For comparison with myocardial tissue, the mechanical rigidities are expressed per unit width. Dividing the above expressions by w gives

$$\frac{EA}{w} = Et, \tag{3.6}$$

and

$$\frac{EI}{w} = \frac{Et^3}{12}. \tag{3.7}$$

When a unit width of $w = 1\,\mathrm{m}$ is adopted, these expressions are numerically equivalent to the corresponding rigidity values calculated for a one-meter-wide strip. By combining the experimentally obtained Young's modulus with the actual polymer film thickness, the tensile and bending compliance of b-DCPU in the final device can be evaluated. The resulting rigidity values are compared with reported mechanical parameters of cardiac tissue and cardiac interface structures in order to evaluate whether the polymer-supported device approaches the mechanical compliance required for conformal interaction with the myocardium [41]. These parameters are further used to assess the degree of mechanical matching between the flexible polymer supporting layer and myocardial tissue[41].

3.9. SiN Protective Layer and Polymer Lithography

Direct photolithographic processing on b-DCPU is limited by the chemical and thermal sensitivity of the polymer. This section describes the introduction of a SiN protection layer, followed by lithographic patterning and SiN etching to form a hard mask for subsequent polymer processing.

3.9.1. Protective Layer Concept

b-DCPU is relatively sensitive to the photoresist and associated chemical treatments used in conventional photolithography. Direct contact may lead to degradation of the polymer surface or changes in its material properties. Because b-DCPU is employed as a soft and bioresorbable polyurethane-based substrate rather than as a conventional microfabrication substrate, the subsequent lithographic process must be adapted to limit unnecessary chemical and thermal exposure of the polymer [37, 38]. In order to avoid this problem, a SiN layer is deposited onto the b-DCPU surface as a protection layer, preventing direct contact between the polymer and the subsequently applied photoresist. The SiN layer therefore provides an intermediate inorganic processing surface, allowing the subsequent lithographic steps to be performed without direct contact between the photoresist process and the underlying b-DCPU. In addition to its isolation function, the SiN layer can also serve as a hard mask during the subsequent polymer patterning process, thereby improving the stability of pattern transfer.

In a hard-mask process, the lithographically defined pattern is first transferred from the photoresist into a more etch-resistant inorganic layer, which subsequently protects the underlying material during plasma etching. This approach reduces the dependence of the subsequent polymer etch on the plasma resistance of the photoresist alone.

3.9.2. SiN Deposition

After curing of the b-DCPU layer, a nominal SiN thickness of approximately 90 nm is deposited onto the polymer surface. The deposition conditions need to balance film integrity and the thermal stability of the polymer in order to avoid damage to the underlying b-DCPU caused by excessive temperature or plasma exposure.

In preliminary processing, continuous SiN deposition was found to introduce thermal damage and cracking of the underlying polymer. The deposition was therefore divided into three shorter deposition cycles of approximately 30 s each, with the sample removed and allowed to cool between successive cycles. The interrupted deposition sequence was therefore selected experimentally rather than adopted directly from a conventional silicon-based SiN deposition process.

3.9.3. Photolithography

After SiN deposition, conventional photolithography is performed on its surface. The required pattern is defined on the SiN layer through photoresist spin coating, soft baking, exposure, and development. Since the photoresist is in direct contact only with the SiN surface, the underlying b-DCPU remains protected during this process. This process sequence separates the lithographic pattern-definition step from the polymer surface and allows the photoresist-defined geometry to be transferred first into the more plasma-resistant SiN layer.

3.9.4. SiN Etching

After photolithography, the patterned photoresist is used as an etching mask to selectively remove the exposed SiN, thereby transferring the lithographic pattern into the SiN protection layer. The patterned SiN subsequently provides a more robust masking layer for the longer b-DCPU plasma-etching step than relying on the photoresist alone. After completion of the SiN etching and removal of the remaining photoresist, the patterned SiN layer can further serve as the hard mask for the subsequent dry etching of b-DCPU.

3.10. b-DCPU Dry Etching

After patterning of the SiN hard mask, the exposed b-DCPU regions must be selectively removed to define the final polymer geometry. This section describes the O_2/Ar plasma-etching approach and the methods used to monitor and evaluate the polymer-removal process.

3.10.1. Etching Strategy

After patterning of the SiN hard mask, the exposed b-DCPU regions are dry etched in order to further transfer the pattern from the SiN layer into the polymer. Oxygen-containing plasmas are widely used for the dry etching and removal of organic polymeric materials. Reactive oxygen species interact with the polymer surface, promoting oxidation and chain scission and forming volatile reaction products

that can be removed from the surface [40].

Since b-DCPU is an organic polymer, its removal mainly relies on oxygen plasma, which oxidizes the organic components and converts them into volatile reaction products. Studies on polyurethane and related polymer systems have shown that oxygen plasma exposure can result not only in material removal but also in oxidation and changes in surface chemistry and morphology [43]. During this process, the SiN layer serves as a hard mask to protect the polymer regions that need to remain, thereby improving the selectivity and structural stability of the pattern transfer process.

3.10.2. O_2/Ar Etching Parameters

A mixed O_2/Ar plasma is employed in this study for dry etching of b-DCPU. O_2 provides the reactive species responsible for oxidation and removal of the organic polymer, while Ar is included as an auxiliary plasma gas in the etching process. The etching condition used in this study consists of 80 sccm O_2 and 5 sccm Ar at a plasma power of 200 W. The polymer removal rate is controlled by adjusting the gas flow rates, plasma power, chamber pressure, and etching time. The selected O_2/Ar condition is treated as an experimentally established process recipe for the present b-DCPU system rather than as a universal polyurethane etching condition, since polymer plasma-etching behaviour depends strongly on material chemistry and process parameters. Since the b-DCPU layer has a relatively large thickness, the required etching duration needs to be determined according to the actual film thickness and the previously obtained etching rate.

Because the effective b-DCPU removal rate was observed to change during extended plasma exposure, the required etching time cannot be estimated from a single constant etch rate alone. Instead, the removal depth is evaluated as a function of etching duration and used together with endpoint monitoring and surface inspection. In this way, removal of the target polymer regions can be evaluated while avoiding unnecessary damage to the underlying functional layers.

3.10.3. Post-Etch Cleaning

After completion of the dry etching process, the sample surface is inspected and residues formed during etching are removed. This step is required to ensure that the exposed regions are sufficiently cleaned and to prevent residual particles from interfering with the subsequent device release and backside processing. Because oxygen plasma treatment can simultaneously cause polymer removal, surface oxidation, and chemical restructuring, solid or weakly attached post-etch material should not automatically be assumed to consist of the original polymer alone [43, 44, 45].

In the present study, the chemical composition of the post-etch residue was not independently characterized. Possible mechanisms such as plasma-induced oxidation, chain scission, restructuring, or formation of less volatile degradation products are therefore treated only as hypotheses rather than as confirmed explanations. During cleaning, strongly corrosive treatments that may damage the b-DCPU, SiN hard mask, or underlying optical functional layers need to be avoided. Therefore, appropriate physical or chemical cleaning methods should be selected according to the nature of the etching residues. Because the residue composition is not yet known, post-etch cleaning is evaluated empirically with emphasis on residue removal while preserving the remaining polymer and underlying device layers.

3.11. Planned Final Fabrication Steps

Several fabrication steps remain after completion of the front-side integration and polymer patterning. This section outlines the planned release, re-mounting, final backside thinning, and device separation required to obtain the intended final device structure.

3.11.1. Release from Carrier Wafer

After completion of the polymer patterning and the related front-side fabrication processes, the device is planned to be released from the temporary carrier wafer. During this step, the Crystalbond 555 used for temporary bonding needs to be removed while minimizing possible mechanical or chemical damage to the b-DCPU, UCNP layer, and underlying optical structures.

The release step marks the transition from carrier-supported front-side processing to backside processing. The carrier is therefore retained until the front-side fabrication steps that require mechanical support

and vacuum-assisted handling have been completed. After release, the device will retain the completed front-side functional layers and proceed to the subsequent backside processing stage.

3.11.2. Re-mounting for Backside Processing

For the subsequent backside thinning process, the released device needs to be re-mounted with the device orientation adjusted so that the backside of the detector can be directly accessed for processing. As the thickness of crystalline silicon decreases, its bending stiffness is strongly reduced and the structure becomes increasingly sensitive to mechanical handling and externally applied loads [36]. Mechanical support therefore remains necessary during the backside processing of the locally thinned detector. During re-mounting, sufficient flatness and mechanical support need to be maintained in order to reduce the risk of fracture or deformation of the ultrathin region during the following etching process.

3.11.3. Final Backside Thinning

During the initial pre-processing stage, the central optical region of the detector has already been thinned from the original thickness of approximately 290 µm to approximately 10 µm. In the final fabrication stage, this region is planned to be further thinned by backside dry etching to approximately 1 µm in order to improve its UV transmission. The approximately 1 µm thickness represents the intended final design target for the local optical transmission region rather than a thickness that has already been experimentally achieved in the present work.

In this way, the UV light generated by the UCNPs and transmitted through the Fabry–Pérot filter can further propagate through the detector toward the underlying tissue. The final thinning process will be limited to the local optical window, while the surrounding thicker silicon structure will remain to provide mechanical support. This locally thinned configuration combines a reduced silicon thickness within the optical pathway with a mechanically more robust surrounding structure, which is advantageous because ultrathin silicon becomes progressively more flexible and mechanically sensitive as its thickness decreases [36].

3.11.4. Rationale for Late-Stage Thinning

The final thinning step is intentionally arranged at a late stage of the device integration process rather than being completed during the initial detector pre-processing. Ultrathin silicon structures exhibit substantially reduced bending stiffness and become more sensitive to residual stress, handling, and deformation as the silicon thickness is reduced [36].

The main reason is that, when the silicon membrane thickness is reduced to approximately 1 µm, the local structure becomes more sensitive to residual stress and may undergo significant deformation, which can reduce the surface flatness of the device. For multilayer interference filters, the spectral response depends on the optical thickness of the deposited dielectric layers. Variations in deposition thickness or uniformity can therefore shift or broaden the intended optical response [17, 30]. Such surface deformation may influence the deposition uniformity of the subsequent Fabry–Pérot multilayer structure and further change its optical response. The fabrication sequence is therefore designed so that the mechanically sensitive final thinning step is separated from the deposition of the thickness-sensitive FP multilayer structure.

Therefore, the final backside thinning is postponed until after the integration of the Mo light-blocking layer, Fabry–Pérot filter, UCNP layer, and polymer substrate. In this way, the influence of the ultrathin silicon structure on the front-side microfabrication processes can be minimized.

3.11.5. Final Device Release

After completion of the final backside thinning, the structure is planned to be released and separated along the predefined device boundary to form an independent flexible device. These final release and separation steps are part of the intended fabrication workflow and were not completed within the process-validation stage described in this study.

The final device is expected to preserve the complete optical functional region, polymer supporting structure, and accessible metal contact pads, thereby providing the required structure for subsequent optical detection, electrical connection, and functional validation of the device.

3.12. Characterization Methods

A combination of optical, morphological, mechanical, and thin-film characterization techniques was used to evaluate the materials and structures produced during fabrication. This section summarizes the measurement methods used to assess film thickness, surface morphology, mechanical properties, optical performance, and etching progress.

3.12.1. Optical Microscopy

Optical microscopy is used for rapid inspection of samples at different fabrication stages, including the photolithographic patterns, metal light-blocking regions, Fabry–Pérot filter patterns, UCNP coverage, and polymer patterning results. This method is mainly employed to evaluate the pattern integrity, boundary positions, and the presence of obvious particles, residues, or surface defects.

3.12.2. Ellipsometry

Ellipsometry is used to measure the thickness of SiO_2 and SiN thin films and to assist in determining their actual deposition rates. By performing short test depositions on reference samples and measuring the resulting film thicknesses, the corresponding deposition rates can be calculated and subsequently used to calibrate the deposition time required for each layer in the Fabry–Pérot multilayer structure.

For fabrication processes requiring accurate control of optical thin-film thickness, ellipsometry provides a rapid and non-destructive thickness measurement method.

3.12.3. Profilometry

Profilometry is used to measure the thickness or etching depth of structures with a clearly defined step height. By scanning across the surface of a sample containing a step, the height difference between different regions can be obtained.

In this study, profilometry can be used to evaluate the polymer thickness, etching depth, and actual thickness of selected thin-film structures, thereby assisting in determining whether the deposition and etching processes have reached the target dimensions.

3.12.4. Scanning Electron Microscopy

Scanning electron microscopy (SEM) is used for higher-resolution morphological characterization of micro- and nanoscale structures. Compared with optical microscopy, SEM provides more detailed information on the distribution of UCNPs, surface residues, and the local morphology of structures after etching.

When further analysis of particle size, surface coverage, or small fabrication defects is required, SEM is employed to provide additional morphological information.

3.12.5. Atomic Force Microscopy

Atomic force microscopy (AFM) is used to characterize the three-dimensional surface morphology and local height variations of the samples. By scanning across the sample surface, the surface topography can be obtained, allowing further analysis of surface roughness and local structural height.

For the UCNP deposition layer and other structures containing nanoscale surface features, AFM can be used to complement the two-dimensional morphological information obtained from SEM and provide additional height information in the vertical direction.

3.12.6. Tensile Testing

Tensile testing is used to characterize the mechanical response of the b-DCPU polymer. Dogbone-shaped specimens are subjected to uniaxial tensile loading while the applied force and corresponding displacement are recorded. The measured data are converted into stress–strain curves, from which the Young's modulus is determined. The obtained modulus is subsequently used for the calculation of the tensile rigidity and flexural rigidity of the polymer layer.

3.12.7. Optical Power Measurement

An optical power meter is used to evaluate the relative optical output of the UCNP layer under near-infrared excitation. The emitted light is collected after passing through the corresponding optical filtering configuration, and the measured optical power is used to compare the emission intensity under different excitation conditions and deposition states.

This measurement provides a direct method for assessing changes in the optical output of the UCNP layer and for evaluating the influence of process parameters on the overall upconversion performance.

3.12.8. Spectral Measurement

A spectrometer is used to characterize the emission spectrum of the UCNP layer under near-infrared excitation. The measured spectrum is used to identify the characteristic emission bands of the UCNPs and to evaluate their spectral overlap with the transmission characteristics of the Fabry–Pérot filter and the fluorescence wavelength range of NADH.

The spectral measurement therefore provides complementary information to the optical power measurement by resolving the wavelength distribution of the emitted light rather than only its integrated optical intensity.

3.12.9. Etching Endpoint Detection

Etching endpoint detection was employed as an in-situ monitoring method during plasma etching to assist in identifying the completion of material removal. The monitoring system records changes in the optical signal reflected from the sample surface as a function of etching time. Variations in the optical properties of the exposed surface, including refractive index, absorption, reflectivity, and surface morphology, can therefore lead to corresponding changes in the measured signal.

For multilayer structures, the endpoint signal may exhibit periodic or quasi-periodic variations as materials with different optical properties are sequentially exposed and removed. When the etching front reaches an underlying layer with substantially different optical characteristics, the signal response can change in amplitude, frequency, or overall stability. Such changes can provide an indication that the target layer has been substantially removed and that the etching process is approaching its endpoint.

The exact form of the endpoint signal depends on the material system, layer thickness, surface condition, and plasma process parameters. Therefore, endpoint detection was not used as an independent proof of complete material removal. Instead, the monitored signal was interpreted together with complementary observations, such as surface inspection and step-height or thickness measurements, to determine the progress and completion of the etching process.

In this study, endpoint monitoring was applied during the dry etching of the Fabry–Pérot multilayer, the SiN protection layer, and the b-DCPU polymer. Because these materials exhibit different optical and plasma-interaction characteristics, their endpoint responses were evaluated individually and are discussed together with the corresponding experimental results in Chapter 4.

4 Experiments and Results

4.1. Front-Side Mo Light-Blocking Layer

4.1.1. Photolithography Mask Design

Two photolithography mask layouts were used for the Mo light-blocking process, as shown in Figure 4.1. Figure 4.1(a) shows the mask designed for process simulation on a glass wafer. In addition to the central light-blocking regions, four cross-shaped alignment marks were included near the corners to facilitate alignment during subsequent photolithography steps. Several elongated rectangular regions were also incorporated around the central area. After Mo deposition, these regions were used to form simulated metal contact pads, providing a metal reference surface for assisting endpoint identification during subsequent dielectric etching.

Figure 4.1(b) shows the mask used for fabrication on the actual photodetector. This pattern defines the Mo light-blocking regions while preserving the peripheral metal contact pads for subsequent electrical connection.

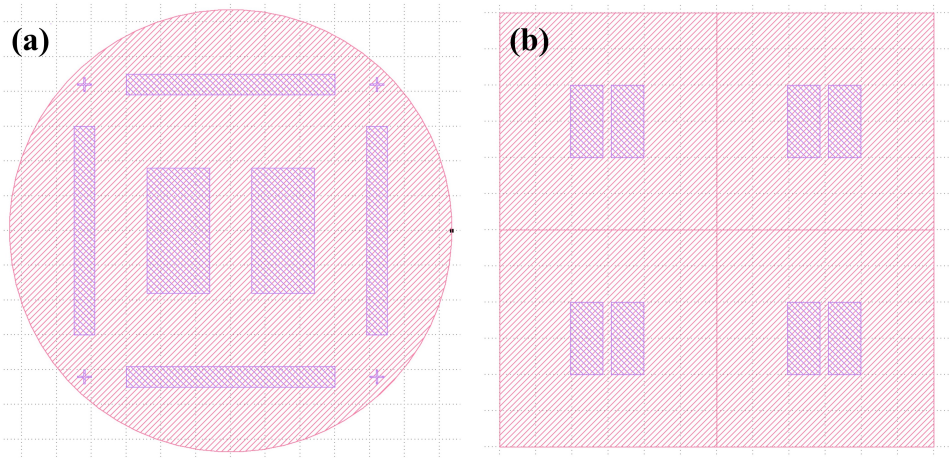


Figure 4.1: Photolithography mask designs used for the Mo light-blocking layer fabrication. (a) Process-simulation mask used on a glass wafer. The four cross-shaped features serve as alignment marks for subsequent photolithography steps, while the elongated rectangular regions are used to form simulated Mo contact pads for assisting endpoint identification during later dielectric etching. (b) Photolithography mask used for Mo patterning on the actual photodetector, defining the front-side light-blocking regions while preserving the peripheral metal contact pads.

4.1.2. Photolithography and Pattern Definition

The Mo light-blocking layer was patterned using S1813 positive photoresist. The photoresist was spin-coated at 2000 rpm for 55 s, followed by a 2 min soft bake. The exposure was performed using a dose setting of 220 and a defocus value of −7, after which the sample was developed in MF-322 for 30 s and rinsed in DI water for 30 s. After spin coating, soft baking, exposure, and development, clear openings were formed in the target light-blocking regions.

For the actual detector, the peripheral metal contact pads remained covered by photoresist during Mo deposition. This configuration prevented permanent Mo coverage of the contact pads and allowed them to be reopened during the subsequent lift-off process. The obtained photolithography pattern showed that the designed shielding regions could be successfully transferred onto the detector surface and provided the required area selectivity for Mo deposition.

4.1.3. Mo Deposition and Lift-Off

After completion of the photolithography process, Mo was deposited with a nominal target thickness of approximately 200 nm. The corresponding deposition time was 4 min 55 s. The approximately 200 nm value represents the deposition process target and was not independently verified by a separate thickness measurement on the integrated detector. Therefore, no experimental thickness uncertainty is assigned to this value. Mo was deposited both within the exposed light-blocking regions and on top of the remaining photoresist. The sample was subsequently immersed in acetone for approximately 16 h to complete the lift-off process.

During lift-off, the photoresist and the Mo deposited on top of it were removed together, leaving Mo only within the predefined light-blocking regions. At the same time, the peripheral metal contact pads were re-exposed. After lift-off, the remaining Mo pattern was generally consistent with the designed front-side light-blocking regions. The localized Mo structures covered the intended shielding areas, while the peripheral metal contact pads remained accessible.

The assessment of the patterned Mo layer at this stage was based primarily on optical inspection of the retained metal regions and the successful reopening of the peripheral contact pads. No independent measurement of the final Mo thickness or optical attenuation was performed on this sample. This result demonstrates that the Mo patterning and lift-off process can form the intended front-side shielding geometry without permanently covering the electrical contact regions. The resulting surface configuration therefore satisfies the geometric integration requirements for the subsequent Fabry–Pérot filter deposition and patterning steps.

4.2. Fabry–Pérot Filter Fabrication

4.2.1. SiO_2 and SiN Deposition Rate Calibration

Before deposition of the complete Fabry–Pérot multilayer structure, the actual deposition rates of SiO_2 and SiN were calibrated separately. Both materials were deposited for 5 min in short test runs, after which the resulting film thicknesses were measured and used to determine the corresponding deposition rates. The same test depositions were also used to pre-condition the deposition chamber in order to reduce the influence of the initial chamber condition on the subsequent film growth.

The calibration-film thicknesses were determined by ellipsometry. The deposition rate for each material was calculated from the measured film thickness divided by the corresponding 5 min deposition time. Based on the measured deposition rates, the deposition times in the original multilayer recipe were adjusted. In this way, the thickness of each SiO_2 and SiN layer was determined according to the actual deposition condition of the equipment rather than relying solely on nominal deposition rates. The calibration-film thicknesses therefore represent measured quantities, whereas the individual FP-layer thicknesses were implemented through deposition times calculated from these measured rates rather than independently measured after every layer deposition.

4.2.2. Multilayer Filter Deposition and Optical Response

After completion of the deposition-rate calibration, SiO_2 and SiN were sequentially deposited according to the predefined layer sequence to form the complete Fabry–Pérot multilayer structure. The predefined multilayer sequence had a total designed thickness of 1049 nm. This value represents the sum of the designed individual layer thicknesses and should therefore be interpreted as a design target rather than as an independent measurement of the total thickness of the completed multilayer stack. The complete deposition process was first evaluated on a glass wafer before being applied to the detector sample. This preliminary fabrication step provided a reference for assessing the reproducibility of the multilayer deposition process before integration onto the actual device.

The optical response of the fabricated filter was evaluated by measuring its transmittance spectrum. Figure 4.2(a) shows the simulated and experimentally measured transmittance of the filter fabricated in the previous work[31]. The experimentally measured spectrum from that work was used as a reference for comparison with the filter fabricated in this study. Figure 4.2(b) shows the measured transmittance of the filter fabricated in the present work.

Although differences in the detailed spectral shape and the exact positions of the transmission minima

can be observed, the measured spectrum shows the same general wavelength-dependent transmission behavior as the previously fabricated reference sample. The comparison is therefore interpreted here as a qualitative agreement in the main spectral characteristics rather than as a quantitative match between the two filters.

4.2.3. Filter Photolithography

After deposition of the complete multilayer structure, photolithography was used to define the regions in which the FP filter should remain. The patterned photoresist protected the optical functional region while exposing the multilayer in areas that required subsequent removal, including the regions above the metal contact pads.

The photolithography layouts used for this process are shown in Figure 4.2(c) and (d). Figure 4.2(c) shows the pattern designed for the actual detector, while Figure 4.2(d) shows the corresponding process-validation pattern used on the glass wafer. The glass-wafer pattern was used to evaluate the deposition and etching process before applying the complete pattern-transfer sequence to the detector. An example of the patterned glass-wafer sample is shown in Figure 4.2(e). The defined filter regions and surrounding reference structures remained clearly distinguishable after fabrication, allowing the subsequent etching process to be evaluated on a simplified test substrate.

4.2.4. Etching Recipe Comparison

Because the FP filter consists of alternating SiO_2 and SiN layers with a total designed thickness of approximately 1049 nm, the dry-etching process must provide sufficient removal of the dielectric stack while maintaining adequate photoresist thickness throughout pattern transfer. Two CHF_3-based dry-etching conditions were experimentally compared, as summarized in Table 4.1.

Table 4.1: Dry-etching conditions evaluated for patterning the SiO_2/SiN Fabry–Pérot multilayer structure.

Recipe	CHF_3	Additive gas	Plasma power	Etching time
CHF_3/O_2	50 sccm	O_2: 5 sccm	100 W	10 min
CHF_3/Ar	50 sccm	Ar: 5 sccm	100 W	10 min

After 10 min of etching, the measured removal amounts of the FP filter and photoresist were approximately 324 nm and 466 nm, respectively, for the CHF_3/O_2 condition. Under the CHF_3/Ar condition, the corresponding removal amounts were approximately 364 nm and 274 nm. The filter-to-photoresist selectivity was calculated as

$$S = \frac{d_{\text{filter}}}{d_{\text{PR}}}, \tag{4.1}$$

where d_{filter} and d_{PR} are the measured removal depths of the dielectric multilayer and photoresist, respectively.

The resulting filter-to-photoresist selectivities are summarized in Table 4.2.

Table 4.2: Measured removal amounts and calculated filter-to-photoresist selectivities after 10 min of dry etching.

Recipe	Filter removal	Photoresist removal	Selectivity
CHF_3/O_2	324 nm	466 nm	0.70
CHF_3/Ar	364 nm	274 nm	1.33

Under the tested conditions, the CHF_3/Ar recipe resulted in a slightly larger dielectric removal while consuming substantially less photoresist. Consequently, the calculated filter-to-photoresist selectivity increased from approximately 0.70 for the CHF_3/O_2 condition to approximately 1.33 for the CHF_3/Ar condition. This corresponds to an increase in selectivity by a factor of approximately 1.9 under the tested conditions. The CHF_3/Ar recipe was therefore selected for the subsequent patterning experiments.

4.2.5. Etching Selectivity and Endpoint Detection

The filter and photoresist removal amounts were determined from changes in the measured step height. The surface profile was measured before etching, after a defined etching period, and again after removal of the remaining photoresist. Comparison of these measurements allowed the contributions from dielectric removal and photoresist consumption to be evaluated separately. The reported removal depths of 324 nm, 466 nm, 364 nm, and 274 nm therefore represent experimentally measured step-height differences rather than nominal etching depths.

In addition to the step-height measurements, endpoint detection was used to monitor the progress of the dry-etching process. Figures 4.2(f) and (g) show endpoint signals obtained from two separate FP-filter etching experiments performed using the selected CHF_3/Ar recipe. During etching of the alternating SiO_2/SiN multilayer, pronounced variations in the monitored signal were observed. These variations are consistent with changes in the material being exposed to the plasma as the multilayer structure was progressively removed. Toward the end of both etching experiments, the signal became comparatively stable and the large variations associated with the dielectric multilayer were no longer observed.

The transition toward a relatively stable endpoint signal was used as an indirect indication that the exposed dielectric multilayer had been substantially removed and that the etch was approaching the underlying metal layer. Since the endpoint signal does not provide a direct thickness measurement, this interpretation was considered together with the measured step-height changes and the subsequent surface condition rather than being used as the sole criterion for determining completion of the etching process.

4.3. UCNP Deposition and Optical Characterization

4.3.1. Initial Drop-Casting Challenges

The UCNP suspension was deposited onto the Fabry–Pérot filter by drop casting. Previous experiments showed that the final particle distribution could be strongly affected by the surface condition and drying behavior. Figure 4.3(a) shows results obtained in the previous work, including an untreated glass wafer and two glass wafers after UCNP deposition. The deposited samples exhibited pronounced non-uniformity and uncontrolled lateral spreading. The degree of lateral spreading and macroscopic uniformity in these preliminary experiments was assessed by visual inspection of the deposited regions rather than by a quantitative surface-coverage metric.

O_2 plasma treatment was initially considered as a possible approach for improving the wetting of the UCNP suspension on the substrate. However, the increased surface wettability promoted lateral spreading of the droplet and reduced the spatial confinement of the deposited region under the present drop-casting conditions. Since localized deposition within the optical functional region is required for device integration, O_2 plasma pretreatment was therefore not adopted in the subsequent experiments. These observations indicated that controlling the droplet volume alone was insufficient to obtain a spatially confined and uniform UCNP layer. The following experiments therefore focused primarily on controlling the drying conditions and evaporation rate.

4.3.2. Deposition Condition Optimization

To reduce the evaporation rate of the deposited droplet, a locally humidified drying configuration was introduced, as illustrated in Figure 4.3(b). The sample was placed on a hotplate at 40 °C and covered by an inverted container. A wet sponge was placed inside the enclosed volume to increase the local humidity and thereby slow the evaporation of the solvent. Figure 4.3(c) shows a deposition result obtained using the combination of humidity control and lower-temperature drying. Compared with the previous deposition results, the deposited region showed visibly improved spatial confinement and a more uniform macroscopic appearance. This comparison was based on optical inspection of the deposited area rather than on a quantitative measurement of particle-density uniformity.

A further experiment was performed using the same humidity-controlled and lower-temperature condition, together with a double-solvent system consisting of H_2O and glycerol at a volume ratio of 50:1 and sodium citrate as a surfactant. The corresponding result is shown in Figure 4.3(d). No visually distinguishable additional improvement in macroscopic deposition morphology was observed

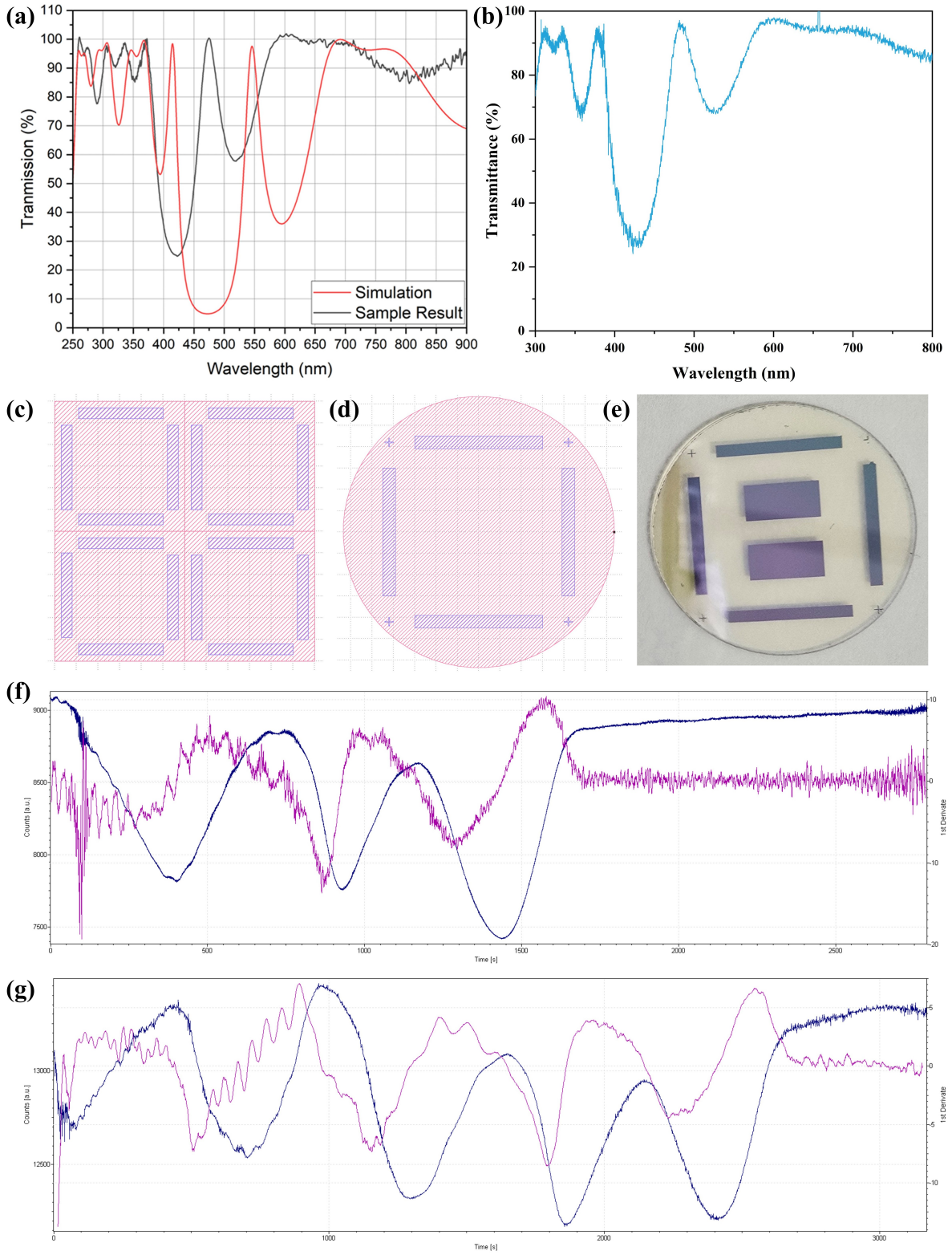


Figure 4.2: Fabrication and characterization of the Fabry–Pérot filter. (a) Simulated and experimentally measured transmittance spectra of the FP filter fabricated in the previous work, used as a reference for comparison. Source: reproduced from the MSc thesis defense presentation of Haoxiang Jiang, TU Delft, 2025[31]. (b) Experimentally measured transmittance spectrum of the FP filter fabricated in this study. (c) Photolithography pattern used for FP-filter patterning on the actual detector. (d) Corresponding process-validation pattern used on a glass wafer. (e) Photograph of the fabricated filter structure on the glass-wafer test sample. (f–g) Endpoint signals recorded during two separate FP-filter dry-etching experiments using the CHF_3/Ar recipe. The transition toward a comparatively stable signal at the end of each process was used, together with measured step-height changes and surface inspection, as an indirect indication that the dielectric multilayer had been substantially removed and that the etch was approaching the underlying metal layer.

compared with the humidity-controlled, lower-temperature condition shown in Figure 4.3(c).

Under the conditions investigated in this study, the comparison suggests that humidity control and lower-temperature drying were the dominant factors in improving the deposition morphology, whereas the addition of glycerol and sodium citrate did not produce an obvious further improvement. This conclusion is restricted to the specific deposition conditions examined here and is based on qualitative comparison of the deposited morphology rather than a quantitative separation of the individual effects of humidity, temperature, glycerol, and sodium citrate.

The subsequent deposition process therefore focused primarily on reducing the solvent evaporation rate. The improved deposition behavior observed under the humidity-controlled and lower-temperature condition indicates that solvent evaporation plays an important role in determining the final UCNP distribution during drop casting. Slower evaporation provides a longer period for particle redistribution within the droplet before complete drying and reduces the rapid accumulation of particles associated with uncontrolled solvent loss. Based on the experimental comparison shown in Figure 4.3(a)–(d), control of the drying environment was identified as a major process parameter for improving the macroscopic confinement of the UCNP deposit under the tested conditions. The evaporation rate itself was not directly measured in this study.

4.3.3. Droplet Volume and Deposition Area Control

In addition to the drying condition, the deposited droplet volume was adjusted to improve control over the lateral deposition area. Excessive droplet spreading may result in UCNP coverage outside the intended optical functional region and interfere with surrounding device structures. A single-droplet volume of approximately 10 µL was selected for the optimized deposition condition. This smaller volume provided improved control of the deposition area and was used together with humidity-controlled, lower-temperature drying in the subsequent deposition experiments. The improvement in deposition-area control was evaluated from the visible lateral extent of the dried deposit; no independent quantitative measurement of the deposited-area fraction was performed.

4.3.4. UCNP Layer Morphology and Thickness

The surface morphology of the deposited UCNP layer was characterized by scanning electron microscopy (SEM). A lower-magnification image is shown in Figure 4.3(e), where the deposited surface exhibits continuous particle coverage over the observed region. The higher-magnification image in Figure 4.3(f) reveals densely packed nanoparticles together with local particle agglomeration. distribution measurement. Based on the high-magnification SEM image, the characteristic particle diameter was estimated to be on the order of 50 nm. This value is used as a representative size estimate and does not represent a statistical particle-size distribution obtained from automated image analysis.

Atomic force microscopy (AFM) was further used to characterize the surface topography and vertical height variation of the UCNP layer. Figures 4.3(g)–(i) correspond to the same AFM sample and the same scan area, presented using different topographical views. The measurements reveal a rough, non-planar surface with substantial local height variation, consistent with the morphology observed by SEM.

Based on AFM and profilometry height measurements, the deposited UCNP layer showed an average thickness of approximately 2.2 µm, while the minimum measured thickness was approximately 1.6 µm. These values are treated as experimentally measured layer-height values for the characterized sample. No statistical uncertainty is assigned here because a repeated-sample thickness distribution was not determined. If a representative particle diameter of approximately 50 nm is used only as a simple geometric reference, the measured thicknesses correspond numerically to approximately 44 and 32 particle diameters, respectively. These values should not be interpreted as experimentally resolved numbers of discrete nanoparticle layers, because the deposit is rough, locally agglomerated, and non-planar. The measured UCNP thickness was therefore approximately 1.6 µm to 2.2 µm, exceeding the approximately 1 µm design target. Relative to the 1 µm target, the measured minimum and average thicknesses were approximately 1.6 and 2.2 times the target value, respectively.

Further reduction of the deposited particle amount is therefore required to obtain a thinner UCNP layer while maintaining sufficient surface coverage.

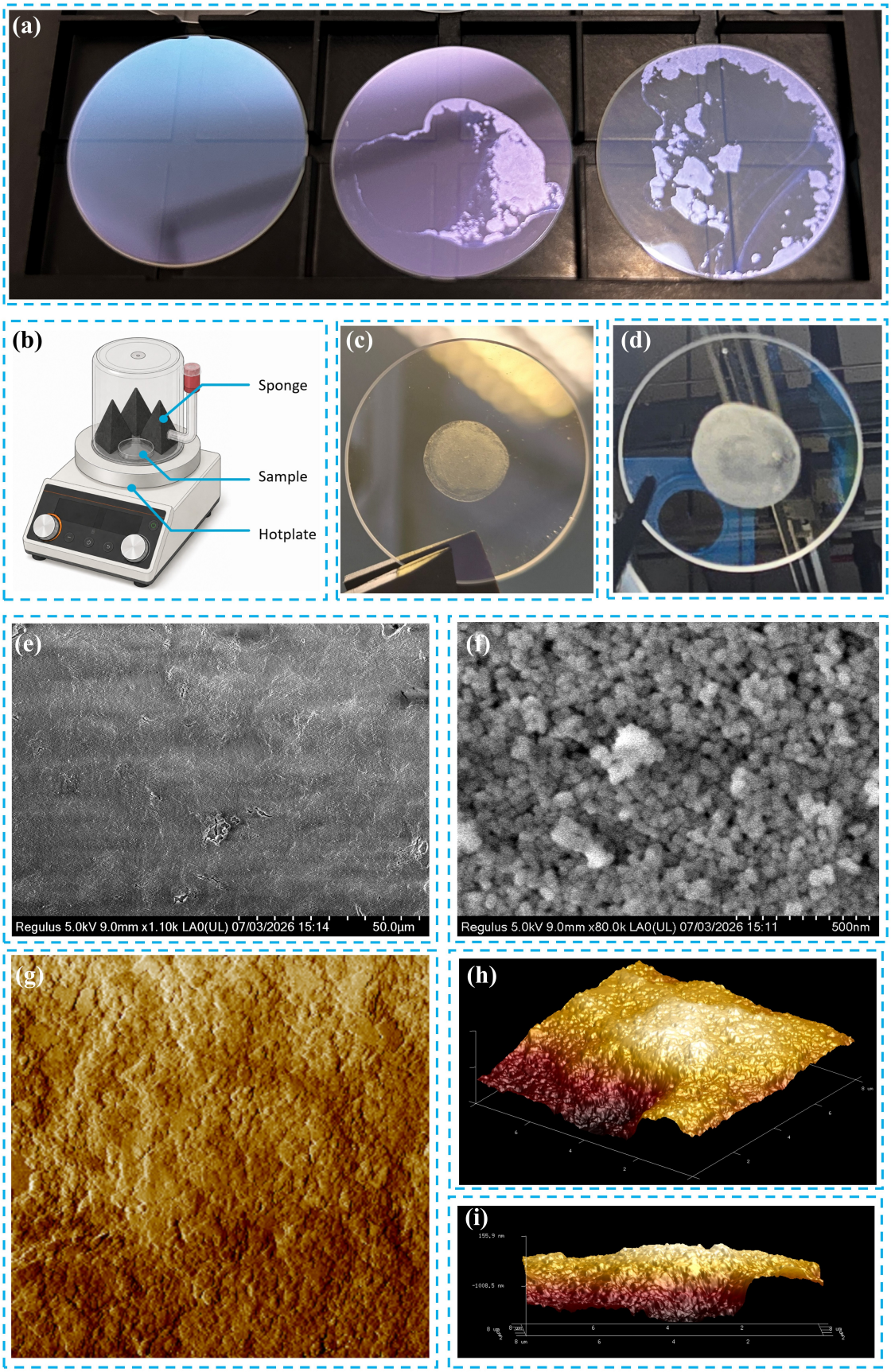


Figure 4.3: Optimization and morphological characterization of the UCNP deposition process. (a) Glass-wafer samples from the previous work. Source: reproduced from the MSc thesis defense presentation of Haoxiang Jiang, TU Delft, 2025[31]. (b) Schematic of the humidity-controlled, lower-temperature drying configuration used in this study. (c) UCNP deposition obtained using humidity control and lower-temperature drying. (d) UCNP deposition obtained using humidity control and lower-temperature drying together with an H_2O/glycerol double-solvent system (50:1 by volume) and sodium citrate surfactant. (e) Low-magnification SEM image of the deposited UCNP layer. (f) High-magnification SEM image showing the local nanoparticle morphology and particle packing; the characteristic particle diameter was estimated to be on the order of 50 nm. (g–i) AFM topographical representations of the same sample and scan area, showing the rough and non-planar UCNP surface.

4.3.5. UCNP Optical Output under 808 nm Excitation

The optical response of the deposited UCNPs under 808 nm excitation was evaluated using an optical setup consisting of an 808 nm laser diode, collimating and focusing optics, and an optical power meter. Measurements were performed under the same optical alignment and excitation conditions for a reference sample consisting of the polymer and Fabry–Pérot filter stack, and for a corresponding sample containing the same polymer/filter structure with an additional deposited UCNP layer. The measured integrated optical powers are summarized in Table 4.3.

Table 4.3: Measured integrated optical power for the polymer/filter reference sample and the polymer/filter/UCNP sample under the same 808 nm excitation condition.

Sample	Measured optical power	Difference from polymer/filter reference
Polymer + filter	248.9 mW	–
Polymer + filter + UCNPs	262.2 mW	13.3 mW

The measured difference between the two samples was calculated as

$$262.2\,\mathrm{mW} - 248.9\,\mathrm{mW} = 13.3\,\mathrm{mW}.$$

Using the polymer/filter sample as the reference, the measured integrated optical power was therefore approximately 13.3 mW higher for the sample containing the additional UCNP layer. Because the power meter measures integrated optical power and does not spectrally separate the UCNP emission from residual excitation light and other optical contributions, the 13.3 mW difference is treated only as an additional measured optical-power contribution associated with the presence of the UCNP layer in the polymer/filter/UCNP structure. It is not interpreted as the absolute UCNP upconversion-emission power or as an upconversion efficiency.

4.3.6. Excitation-Power-Dependent UCNP Output

The laser-diode drive current was further varied to evaluate how the measured optical-power difference changed with excitation level. Another group of filter-only sample and the filter + UCNP sample were compared at drive currents of 100 mA, 200 mA, 300 mA, and 400 mA.

The measured power differences are summarized in Table 4.4.

Table 4.4: Measured difference in integrated optical power between the filter + UCNP sample and the filter-only sample at different laser-diode drive currents.

Laser-diode drive current	Power difference
100 mA	−2.4 mW
200 mA	2.6 mW
300 mA	13.3 mW
400 mA	22.3 mW

At 100 mA, the measured difference was −2.4 mW, while at 200 mA it was 2.6 mW. The corresponding differences increased to 13.3 mW at 300 mA and 22.3 mW at 400 mA. Because repeated measurements and the uncertainty of the complete optical setup were not quantified, the statistical significance of the individual differences cannot be determined from these measurements alone. In particular, the small positive and negative differences observed at the lower drive currents should not be interpreted as quantitative UCNP emission values. Within the investigated measurement series, the measured difference became more positive as the laser-diode drive current increased. These results are consistent with an excitation-dependent optical contribution from the UCNP-containing layer. However, since the present measurement is based on integrated optical power rather than spectrally resolved emission, the observed power difference should not by itself be interpreted as a quantitative measurement of UCNP upconversion efficiency.

4.4. b-DCPU Polymer Preparation and Optical Properties

4.4.1. Polymer Synthesis and Curing

Bioresorbable dynamic covalent polyurethane (b-DCPU) was prepared through the reaction between polycaprolactone triol (PCL-triol) and hexamethylene diisocyanate (HDI), with a target crosslinking ratio of 80%. The two precursors were mixed under magnetic stirring at approximately 60 °C for 4.5 h. The resulting polymer mixture was subsequently spin-coated to form a thin film and thermally cured at 120 °C for 4 h. The 60 °C mixing temperature, 4.5 h mixing duration, 120 °C curing temperature, and 4 h curing duration represent the process conditions applied in this study. The target crosslinking ratio of 80% is a formulation target and was not independently verified by a separate chemical crosslink-density measurement.

After curing, a continuous b-DCPU film was obtained for subsequent thickness optimization, optical characterization, and mechanical testing. Since the polymer layer serves both as the flexible supporting substrate of the device and as part of the optical propagation path, its thickness and optical compatibility with the underlying Fabry–Pérot (FP) filter are important parameters for device integration.

4.4.2. Polymer Spin-Coating Optimization

The initial spin-coating condition produced a b-DCPU layer substantially thicker than the target thickness range of 15 µm to 25 µm. The spin-coating process was therefore progressively modified by increasing the rotational speed of the second coating stage while maintaining the first-stage condition unchanged.

The complete spin-coating recipes and corresponding measured film thicknesses are summarized in Table 4.5. Each programmed step is expressed in the order of rotational speed, acceleration, and duration. For each spin-coating condition, the film thickness was measured three times, and the reported values are presented as mean ± standard error of the mean (SEM), with $n = 3$.

Table 4.5: Spin-coating conditions used for b-DCPU thickness optimization and the corresponding measured film thicknesses. Thickness values are reported as mean ± SEM ($n = 3$). The parameters for each step are reported as rotational speed/acceleration/time, in units of rpm, rpm/s, and s, respectively.

Recipe	Step 1	Step 2	Step 3	Thickness (µm)
Previous recipe	500/300/40	1000/1200/5	0/300/5	74.21 ± 1.93
New recipe 1	500/300/40	2000/1200/55	0/300/55	33.38 ± 2.34
New recipe 2	500/300/40	3000/1200/55	0/300/55	27.27 ± 1.78
New recipe 3	500/300/40	4000/1200/55	0/300/55	17.77 ± 1.69

A clear decrease in film thickness was observed as the rotational speed of the second spin-coating stage was increased. The average thickness decreased from approximately 74.2 µm for the previous recipe to approximately 17.8 µm when the second-stage speed was increased to 4000 rpm. The latter value falls within the target thickness range required for the final device. This corresponds to a thickness reduction of approximately 76% relative to the previous recipe, or a decrease by a factor of approximately 4.2.

4.4.3. Polymer Thickness Control

The spin-coating results demonstrate that the b-DCPU film thickness can be effectively adjusted through the rotational speed of the high-speed coating stage. Increasing the second-stage speed from 1000 rpm to 4000 rpm reduced the mean film thickness from 74.21 µm to 17.77 µm, corresponding to a reduction by a factor of approximately 4.2. Although the average thickness obtained using the 4000 rpm condition satisfied the design target, the measured standard deviations remained on the order of 1.7 µm to 2.3 µm. This indicates that a certain degree of sample-to-sample thickness variation was still present. For the selected 4000 rpm condition, the reported variation of 1.69 µm corresponds to approximately 9.5% of the mean thickness of 17.77 µm.

The 4000 rpm condition was therefore selected as the preferred spin-coating condition for subsequent device integration, while film uniformity and reproducibility remained important considerations for the following SiN deposition, photolithography, and polymer-patterning processes.

4.4.4. Optical Transmittance of the b-DCPU/FP Filter Stack

In the integrated device, the b-DCPU layer is located above the FP filter and forms part of the optical propagation path. It is therefore important to verify that the addition of the polymer layer does not

eliminate the wavelength-selective response of the underlying optical filter. The optical transmittance of the combined b-DCPU/FP filter structure was measured over the UV–visible wavelength range. The resulting spectrum is shown in Figure 4.4.

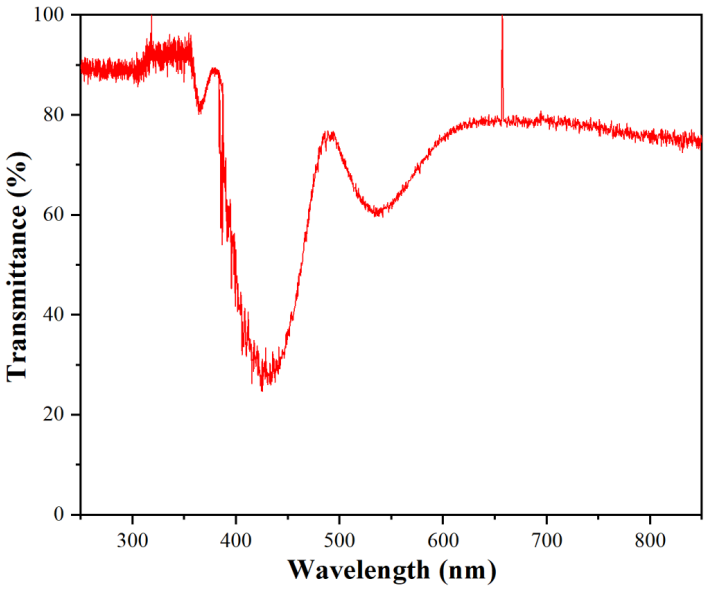


Figure 4.4: Measured optical transmittance spectrum of the integrated b-DCPU/Fabry–Pérot filter structure.

From the measured spectrum, the combined structure reached transmittance values approaching approximately 90% in part of the UV range. A pronounced attenuation band was observed between approximately 400 nm and 460 nm, where the minimum transmittance decreased to approximately 25–30%. At longer wavelengths, the measured transmittance recovered and remained generally in the range of approximately 70–80% over much of the visible-to-near-infrared region. These values were obtained directly from the measured transmittance spectrum and are reported as approximate spectral values rather than as averages from repeated independent samples. These results show that the integrated polymer/filter stack retained a pronounced wavelength-dependent optical response after deposition of the b-DCPU layer.

However, because the measurement was performed on the combined b-DCPU/FP-filter structure rather than on an isolated b-DCPU film, the measured spectrum cannot be used to independently determine the intrinsic optical transmittance or absorption spectrum of b-DCPU. The measurement therefore demonstrates only that the wavelength-dependent response of the combined optical stack remained present after polymer integration. It does not separate the individual optical contributions of the polymer and the FP filter. Instead, it provides a direct assessment of the optical behavior of the polymer/filter stack relevant to the final integrated device.

4.5. Mechanical Characterization of b-DCPU

4.5.1. Tensile Test Specimens and Measurements

The mechanical properties of b-DCPU were evaluated by uniaxial tensile testing using dogbone-shaped polymer specimens. The reduced central gauge section was used to localize the major deformation during stretching. An example of the experimental tensile-test configuration is shown in Figure 4.5(a). A total of three valid specimens ($n = 3$) were tested independently.

The measured force–displacement data were converted into engineering stress–strain curves using the initial specimen dimensions. The resulting curves were subsequently used to determine the Young's modulus and to estimate the tensile and flexural rigidities of the polymer film. The Young's modulus therefore represents an experimentally derived material property obtained from the measured stress–strain response, whereas the tensile and flexural rigidities reported below are calculated quantities that combine the measured modulus with the measured polymer thickness.

4.5.2. Stress–Strain Behavior and Young's Modulus

The stress–strain responses and corresponding linear fits of the three b-DCPU specimens are shown in Figure 4.5(b)–(d). For all three specimens, the Young's modulus was determined by linear fitting over the 0–20% strain range. The individual fitted Young's moduli were approximately 3.38 MPa, 3.11 MPa, and 3.60 MPa, respectively.

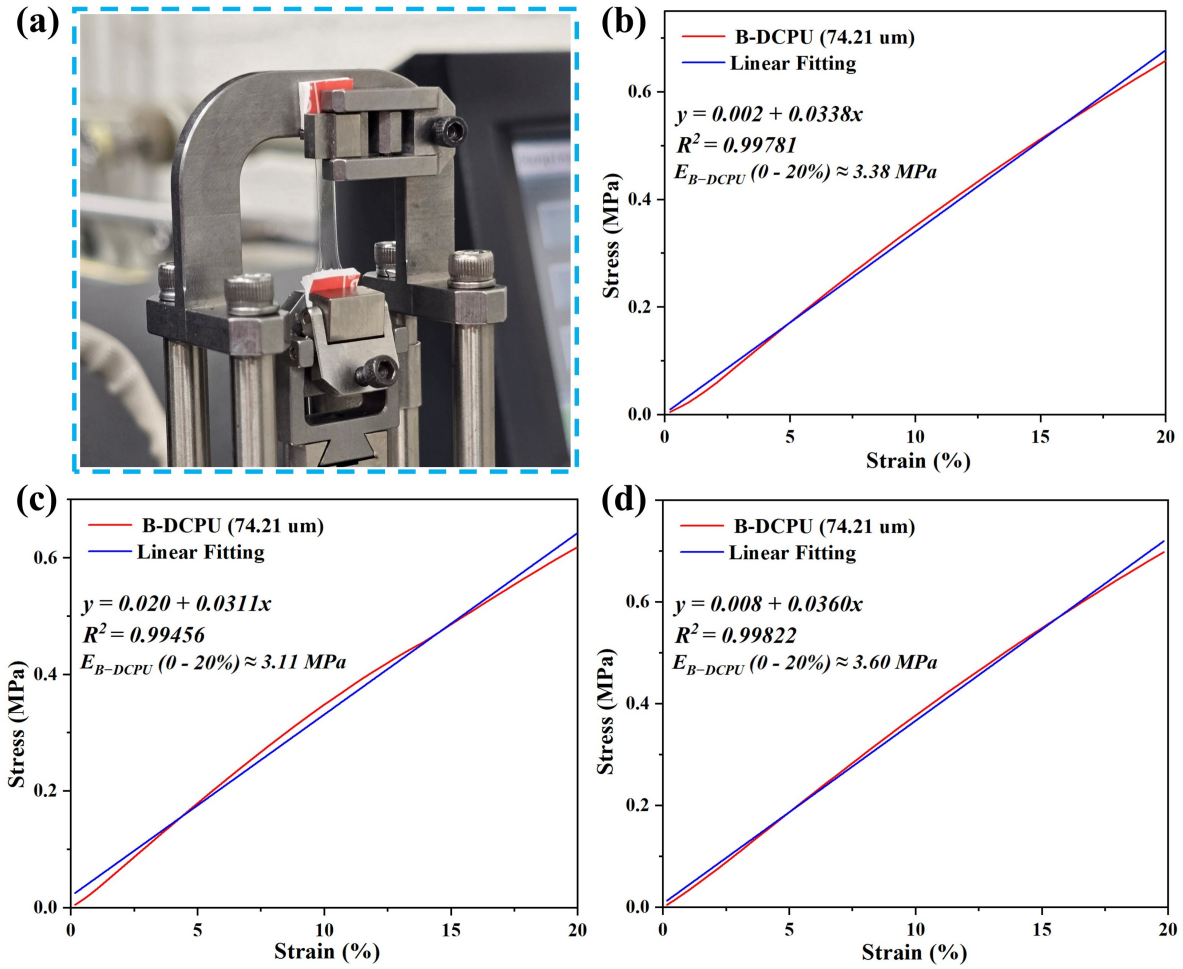


Figure 4.5: Mechanical characterization of b-DCPU by tensile testing. (a) Experimental configuration showing a dogbone-shaped b-DCPU specimen mounted in the tensile tester. (b–d) Engineering stress–strain curves and corresponding linear fits for three independently tested b-DCPU specimens. All linear fits were performed over the 0–20% strain range. The fitted Young's moduli were approximately 3.38 MPa, 3.11 MPa, and 3.60 MPa, respectively. The corresponding R^2 values are summarized in Table 4.6.

The fitting results are summarized in Table 4.6.

Table 4.6: Linear fitting results obtained from the tensile tests of three b-DCPU specimens. All Young's moduli were determined over the 0–20% strain range.

Specimen	Fitting range	Young's modulus (MPa)	R^2
Sample 1	0–20%	3.38	0.99781
Sample 2	0–20%	3.11	0.99456
Sample 3	0–20%	3.60	0.99822

All three linear fits showed high coefficients of determination, with R^2 values ranging from 0.99456 to 0.99822. The fitted Young's moduli also remained within a relatively narrow range across the three independently tested specimens.

The mean Young's modulus was determined to be

$$E = (3.37 \pm 0.14)\,\mathrm{MPa}, \tag{4.2}$$

where the result is reported as mean ± standard error of the mean (SEM) with $n = 3$.

The reported mean was calculated from the three fitted values 3.38 MPa, 3.11 MPa, and 3.60 MPa. The reported uncertainty represents the standard error of the mean rather than the measurement uncertainty of the tensile-testing instrument. The measured modulus indicates that the fabricated b-DCPU is mechanically compliant relative to conventional rigid structural materials. However, Young's modulus alone does not fully describe the mechanical response of a thin-film structure, since the structural stiffness also depends strongly on the film geometry. The measured modulus was therefore further combined with the polymer thickness to evaluate the tensile and flexural rigidities of the b-DCPU layer.

4.5.3. Tensile Rigidity

For comparison with myocardial tissue, the tensile rigidity is expressed per unit width. For a rectangular film of width w and thickness t,

$$\frac{EA}{w} = Et, \tag{4.3}$$

where E is the Young's modulus and t is the polymer thickness.

The quantity EA/w has units of $\mathrm{N\,m^{-1}}$. When a unit width of $w = 1\,\mathrm{m}$ is assumed, its numerical value is equivalent to the tensile rigidity of a one-meter-wide strip.

Using the experimentally determined Young's modulus of (3.37 ± 0.14) MPa and the measured initial polymer thickness of

$$t = (74.21 \pm 1.93)\,\mu\mathrm{m}, \tag{4.4}$$

the tensile rigidity per unit width was calculated to be approximately

$$\left(\frac{EA}{w}\right)_{\text{b-DCPU}} \approx 250\,\mathrm{N\,m^{-1}}. \tag{4.5}$$

The cardiac reference value adopted from Kim et al. [41] is

$$\left(\frac{EA}{w}\right)_{\text{cardiac}} = 76\,\mathrm{N\,m^{-1}}. \tag{4.6}$$

The initial b-DCPU film therefore exhibited a tensile rigidity per unit width approximately

$$\frac{250}{76} \approx 3.3 \tag{4.7}$$

times the adopted cardiac reference value.

The tensile rigidity of the initial b-DCPU film was therefore higher than the adopted cardiac reference value. This comparison demonstrates that, although the polymer itself has a relatively low Young's modulus, the thickness of the supporting layer remains an important parameter governing the in-plane mechanical response of the integrated structure.

4.5.4. Flexural Rigidity

For a rectangular polymer film, the flexural rigidity per unit width is

$$\frac{EI}{w} = \frac{Et^3}{12}. \tag{4.8}$$

Using the same measured Young's modulus and initial polymer thickness, the flexural rigidity per unit width was calculated to be approximately

$$\left(\frac{EI}{w}\right)_{\text{b-DCPU}} = 11.46 \times 10^{-8}\,\text{N m}. \tag{4.9}$$

The cardiac reference value adopted from Kim et al. [41] is

$$\left(\frac{EI}{w}\right)_{\text{cardiac}} = 2.30 \times 10^{-5}\,\text{N m}. \tag{4.10}$$

The calculated flexural rigidity per unit width of the initial b-DCPU film is therefore approximately

$$\frac{2.30 \times 10^{-5}}{11.46 \times 10^{-8}} \approx 2.0 \times 10^{2} \tag{4.11}$$

times lower than the adopted cardiac reference value.

In contrast to the tensile rigidity, the calculated flexural rigidity of the b-DCPU film was substantially lower than the cardiac reference value. This indicates that the polymer supporting layer remains highly compliant under bending deformation.

4.5.5. Required Polymer Thickness for Mechanical Compatibility

Because the tensile rigidity per unit width is directly proportional to the polymer thickness, the b-DCPU layer can be mechanically softened in tension by reducing t. Using the measured mean Young's modulus and the adopted cardiac tensile-rigidity reference, the required thickness was estimated from

$$t = \frac{(EA/w)_{\text{cardiac}}}{E}, \tag{4.12}$$

which gives

$$t = \frac{76\,\text{N m}^{-1}}{3.37\,\text{MPa}} \approx 22.6\,\mu\text{m}. \tag{4.13}$$

The 22.6 µm value is therefore a calculated thickness target based on the mean measured Young's modulus and the adopted cardiac tensile rigidity, rather than a directly measured material property.

This estimated thickness lies within the originally defined design range of 15 µm to 25 µm. The spin-coating optimization described in the previous section reduced the measured mean b-DCPU thickness to

$$t = (17.77 \pm 1.69)\,\mu\text{m}, \tag{4.14}$$

which is below the calculated 22.6 µm tensile-rigidity matching thickness and remains within the intended device design range.

Using the measured mean Young's modulus and the optimized mean thickness, the corresponding tensile rigidity per unit width is approximately

$$\left(\frac{EA}{w}\right)_{\text{optimized}} = Et \approx 59.9\,\text{N m}^{-1}. \tag{4.15}$$

This value is lower than the adopted cardiac reference of $76\,\text{N m}^{-1}$, showing quantitatively that the optimized spin-coating condition reaches the intended tensile-rigidity range.

The combined tensile and flexural analysis therefore shows that thickness control is a key parameter for mechanical integration. While the initial 74.21 µm film produced a tensile rigidity approximately 3.3 times higher than the selected cardiac reference, reducing the b-DCPU thickness to the optimized value of approximately 17.8 µm reduced the calculated tensile rigidity per unit width to approximately $59.9\,\text{N m}^{-1}$.

4.6. SiN Protective Layer and Polymer Lithography

4.6.1. SiN Deposition on b-DCPU

A SiN layer was deposited onto the cured b-DCPU surface to provide an inorganic interface for the subsequent photolithography process and to serve as a hard mask for polymer patterning. The standard optical SiN ICPECVD process used in this study had a nominal deposition rate of approximately $60\,\text{nm min}^{-1}$. This value represents the nominal deposition rate associated with the standard ICPECVD process and was used to estimate the deposited SiN thickness. The SiN thickness on the b-DCPU sample was not independently verified by a separate post-deposition thickness measurement.

Direct transfer of this deposition process to the polymer substrate required additional consideration of the thermal stability of b-DCPU. In particular, prolonged plasma exposure and heat accumulation during continuous deposition were found to affect the integrity of the polymer layer.

4.6.2. Thermal Effect during Continuous SiN Deposition

Initial continuous-deposition trials indicated that prolonged SiN deposition could introduce substantial thermal loading to the underlying b-DCPU. Surface cracking and structural degradation of the polymer were observed by visual and surface inspection after extended continuous deposition. The observed damage was therefore treated as an experimental indication that the continuous SiN process imposed an excessive thermal and/or plasma load on the polymer under the investigated conditions. The individual contributions of substrate heating and plasma exposure were not independently separated in this study. These observations indicated that the standard continuous ICPECVD process was not directly suitable for SiN deposition on b-DCPU. The deposition procedure was therefore modified to reduce heat accumulation while still forming a continuous inorganic layer suitable for subsequent lithography.

4.6.3. Interrupted SiN Deposition with Intermediate Cooling

To reduce the thermal load on the polymer, an interrupted deposition strategy was adopted. SiN was deposited for approximately 30 s, after which the sample was removed from the chamber and allowed to cool before the next deposition cycle. This procedure was repeated four times.

Using the nominal deposition rate of $45\,\text{nm min}^{-1}$, each 30 s deposition cycle corresponds to a nominal SiN thickness of

$$45\,\text{nm min}^{-1} \times 0.5\,\text{min} = 22.5\,\text{nm}. \tag{4.16}$$

After four cycles, the nominal accumulated thickness is therefore

$$4 \times 22.5\,\text{nm} = 90\,\text{nm}. \tag{4.17}$$

The resulting SiN thickness is therefore reported as a nominal accumulated thickness of approximately 90 nm. Because the SiN layer on the polymer-supported sample was not independently measured after deposition, no experimental thickness uncertainty is assigned to the 90 nm value. The use of intermediate cooling reduced the duration of continuous thermal exposure and allowed the SiN layer to be deposited without the severe cracking observed during the initial continuous process.

Under the interrupted-deposition condition, no comparable severe cracking was observed by visual inspection, and the resulting surface could subsequently be used for photolithography and SiN pattern transfer. No independent measurement of SiN residual stress, density, refractive index, or film uniformity was performed on the polymer-supported sample; the suitability of the deposited layer was therefore evaluated primarily from its compatibility with the subsequent fabrication steps. The resulting SiN-coated polymer surface was subsequently used for photolithography and pattern transfer.

4.6.4. Photolithography on SiN-Protected b-DCPU

After SiN deposition, photolithography was performed directly on the SiN surface. The photoresist was therefore separated from the underlying b-DCPU by the inorganic protection layer during spin coating, exposure, development, and subsequent resist removal. A well-defined photoresist pattern could be formed on the SiN-coated polymer surface. The pattern quality was evaluated by optical inspection, which showed that the intended lithographic features remained clearly distinguishable after development.

This result demonstrates that the interrupted SiN deposition procedure provided a sufficiently stable processing surface for the subsequent lithographic step while maintaining physical separation between the photoresist and the b-DCPU layer. The result does not by itself provide a quantitative measure of SiN film uniformity or barrier performance, but confirms its practical suitability for the pattern-transfer sequence used in this study.

4.6.5. SiN Pattern Transfer and Endpoint Detection

Following photolithography, the exposed SiN regions were removed by dry etching in order to transfer the photoresist pattern into the protection layer. During this process, endpoint monitoring was used to assist in identifying the completion of SiN removal. Figure 4.6(a) and (b) show endpoint signals obtained during SiN etching of two different samples. Although the detailed signal evolution and periodic variations differed between the two measurements, both experiments exhibited a pronounced transition to high-frequency signal fluctuations near the end of the etching process. The appearance of these high-frequency fluctuations was treated as a reproducible qualitative feature associated with the final stage of the SiN etching process.

This reproducible change in signal behavior was used as an indication of the SiN etching endpoint. The difference in the preceding signal profiles between the two samples suggests that the exact waveform may depend on the individual sample or process condition; however, the appearance of the high-frequency fluctuation provided a practical feature for identifying the final stage of SiN removal. Since endpoint monitoring provides an indirect optical or plasma-response signal rather than a direct measurement of the remaining SiN thickness, the endpoint feature was interpreted together with subsequent surface inspection rather than being used as the sole criterion for complete SiN removal. The repeated appearance of the high-frequency fluctuation in two independent etching experiments supports its use as a practical process indicator, but no quantitative threshold value or signal-frequency criterion was established in this study.

After completion of SiN etching and removal of the remaining photoresist, the patterned SiN layer remained on the regions intended to be protected. The retained SiN regions and opened areas were verified by surface and optical inspection after resist removal. The resulting SiN pattern was subsequently used as the hard mask for b-DCPU dry etching, completing the pattern-transfer sequence from photolithography to polymer etching.

4.7. b-DCPU Dry Etching

4.7.1. Initial O_2-Based Plasma Etching

After patterning of the SiN hard mask, the exposed b-DCPU regions were etched using an O_2-based plasma. The etching condition used in this study consisted of 80 sccm O_2, 5 sccm Ar, and a plasma power of 200 W. Figure 4.7(a) shows a representative sample after completion of the SiN etching step but before b-DCPU dry etching. At this stage, the polymer remained largely transparent and the patterned SiN layer defined the regions to be exposed during the subsequent polymer etching process.

During the first 1 h of O_2/Ar plasma exposure, the measured b-DCPU thickness within the exposed

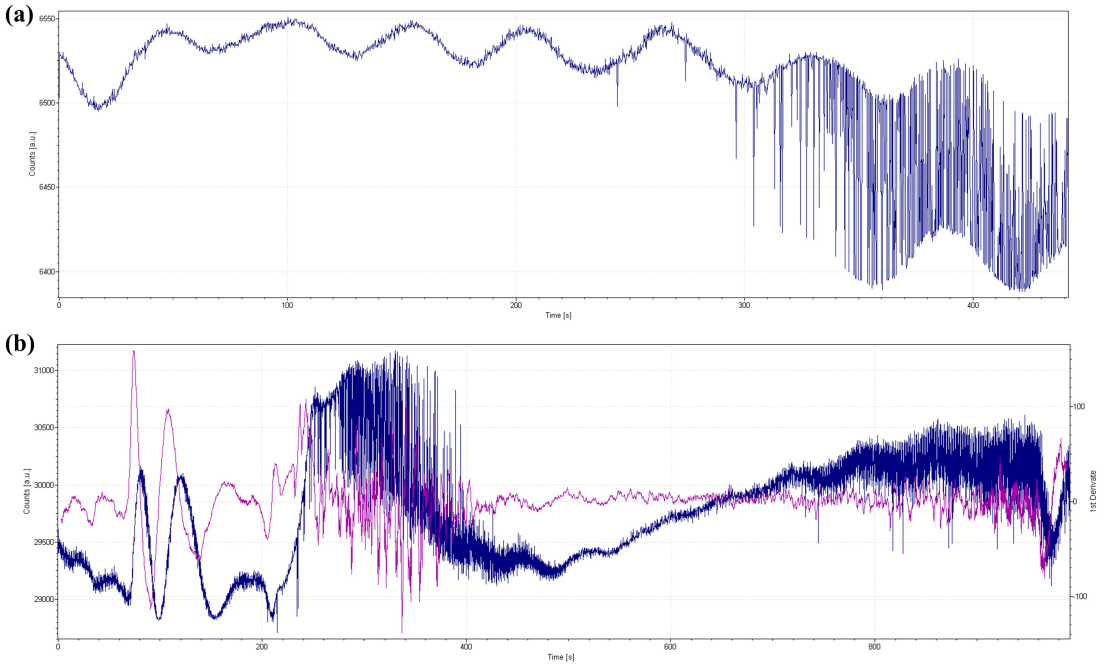


Figure 4.6: Endpoint monitoring during SiN dry etching. (a) Endpoint signal obtained from the first sample. (b) Endpoint signal obtained from the second sample together with its first derivative; the blue curve represents the measured signal and the orange curve represents the first derivative. In both measurements, pronounced high-frequency fluctuations appeared near the final stage of etching and were used, together with subsequent surface inspection, as an indirect indication that the process was approaching the endpoint.

regions decreased by approximately 12 µm, demonstrating substantial material removal during the initial stage of the process. The reported removal depth represents an experimentally measured thickness change rather than a nominal value calculated from the plasma recipe.

4.7.2. Time-Dependent Etching Behavior

As the etching process continued, the optical appearance and surface condition of the exposed b-DCPU changed progressively. A representative sample during polymer etching is shown in Figure 4.7(b), where the exposed polymer region had become visibly more opaque compared with the unetched state. The change in transparency was evaluated by visual inspection and is therefore treated as a qualitative surface observation rather than as a quantitative optical-absorption measurement.

The polymer thickness reduction after different etching durations was measured using a profilometer. Because the plasma-etched surface was not perfectly uniform, the local step height varied across the exposed region. The reported thickness reductions therefore represent average values obtained from the measured surface profile and should be regarded as estimates of the overall material removal rather than as a uniform etch depth across the entire exposed area. The measured polymer thickness changes after different etching durations are summarized in Table 4.7.

Table 4.7: Average b-DCPU thickness reduction measured by profilometry as a function of total dry-etching time using the O_2/Ar plasma condition. The reported values represent spatially averaged estimates because the etched surface was non-uniform.

Total etching time	Average thickness reduction	Incremental effective removal rate
1 h	12.60 µm	12.60 µm h^{-1}
2 h	16.69 µm	4.09 µm h^{-1}
3 h	17.74 µm	1.05 µm h^{-1}

The incremental effective removal rates in Table 4.7 were calculated from the additional average thickness removed during each successive one-hour interval. The measured removal depth did not increase proportionally with etching time. Approximately 12.60 µm of b-DCPU was removed during the first hour, whereas only an additional 4.09 µm was removed during the second hour and approximately

1.05 µm during the third hour.

Although the total plasma-exposure time was increased from 1 h to 3 h, the average measured removal depth increased only from approximately 12.60 µm to 17.74 µm. Thus, the additional two hours of etching removed only approximately 5.14 µm of material. This behavior demonstrates a substantial reduction in the effective polymer removal rate as the process duration increased. Under the investigated condition, simply extending the etching time therefore did not result in a proportional increase in etching depth. Because the etched surface was spatially non-uniform, the profilometry results are interpreted primarily as average removal estimates for comparison between etching durations. The measurements establish the time-dependent decrease in effective removal rate, but they do not by themselves identify the physical or chemical origin of this behavior.

4.7.3. Optical Change and Endpoint Detection

During b-DCPU etching, the exposed polymer gradually changed from a transparent to a more opaque state. This optical change also affected the endpoint-monitoring signal used during the plasma process. The endpoint signal obtained during polymer etching is shown in Figure 4.7(d). At the beginning of the process, pronounced periodic variations were observed in the reflected optical signal. As etching progressed and the exposed polymer became increasingly opaque, the measured reflected optical intensity decreased. This behavior is consistent with increased attenuation of the monitoring light by the modified polymer surface, although the optical absorption of the etched material was not independently measured.

At later stages of the process, the periodic variations gradually diminished and the monitored signal approached a comparatively stable level. The transition from a pronounced oscillatory response to a comparatively flat signal was used as a practical qualitative indication that the polymer etching process was approaching its final stage. Since the endpoint response is based on an indirect optical signal, the transition was interpreted together with the measured etching depth and the observed surface condition rather than being used as the sole criterion for complete polymer removal. In particular, the relatively stable endpoint signal was not interpreted as direct evidence that all b-DCPU had been removed, because residual polymer or etch-generated surface material could still remain within the exposed region. This limitation is particularly relevant because the measured removal depth increased from only approximately 16.69 µm after 2 h to approximately 17.74 µm after 3 h, showing that the process had entered a regime of substantially reduced material removal even while plasma exposure continued.

4.7.4. Formation of White Opaque Residue

After prolonged plasma exposure, a white, opaque, powder-like layer was observed in the regions subjected to b-DCPU etching. The formation of this residue occurred concurrently with the reduction in the apparent polymer removal rate and the loss of optical transparency. Figure 4.7(b) shows a representative sample during the etching process, where the exposed region had already developed a visibly opaque appearance. Figure 4.7(c) shows a representative sample after completion of the polymer etching process, in which the target polymer pattern had been formed. It should be noted that Figures 4.7(a)–(c) were obtained from three different samples rather than from sequential imaging of the same specimen. Consequently, the corresponding metal patterns differ between the three images. The figures are therefore used to illustrate representative process states rather than a continuous evolution of a single sample.

The specific chemical composition of the white residue was not identified in this study. Therefore, although its formation is associated experimentally with prolonged plasma exposure and reduced etching efficiency, the underlying chemical mechanism cannot be determined from the present results alone.

4.7.5. Mechanical and Solvent Removal Tests

Simple removal tests were performed to evaluate the physical behavior of the white residue. Further plasma exposure did not remove the residue effectively. However, its mechanical adhesion appeared to be relatively weak, and the layer could be scraped away using tweezers. The residue also showed a tendency to dissolve gradually in hot water and ethanol. These observations indicate that the post-etch material differs from the original unetched b-DCPU in its physical state and removal behavior.

No additional chemical characterization was performed in this study, and the residue composition therefore remains undetermined.

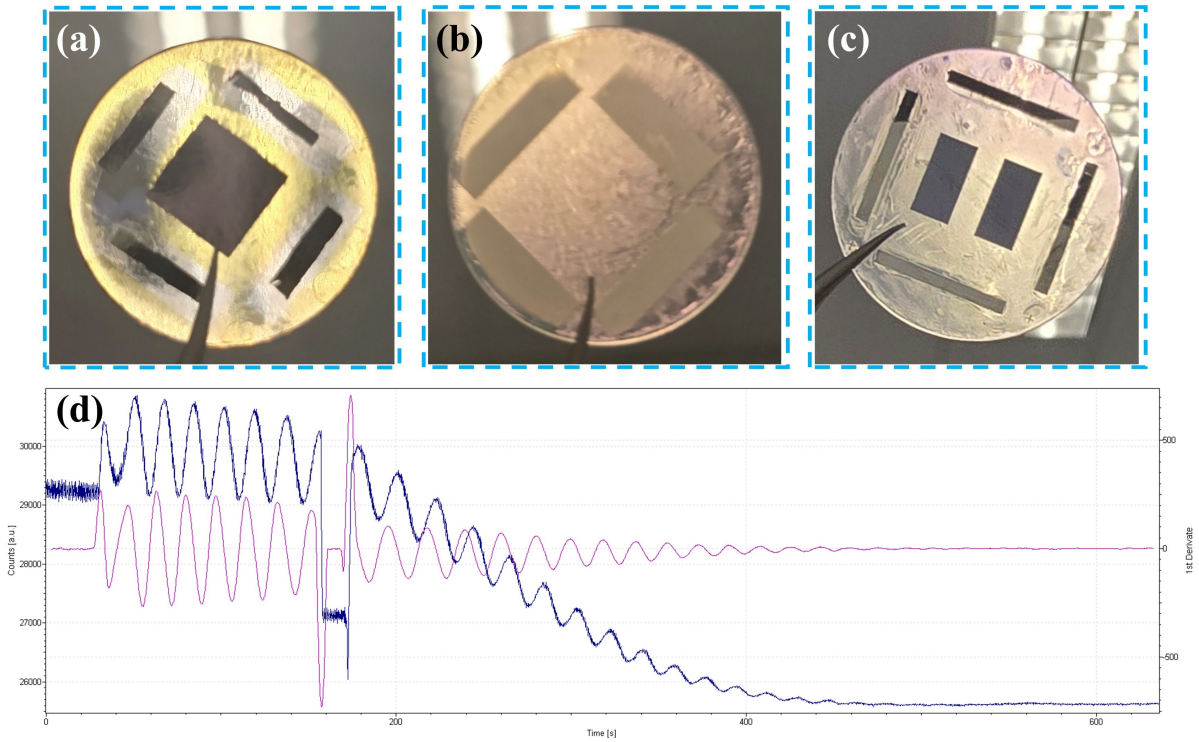


Figure 4.7: Representative results of the b-DCPU dry-etching process. (a) Sample after completion of SiN etching but before b-DCPU dry etching. (b) Representative sample during b-DCPU etching, showing the progressive development of an opaque surface in the exposed polymer region. (c) Representative sample after completion of polymer etching, showing the patterned polymer structure. The samples shown in (a)–(c) are different specimens and therefore exhibit different underlying metal patterns. (d) Endpoint-monitoring signal recorded during b-DCPU dry etching.

4.7.6. Final Etching Limitation

The O_2/Ar plasma condition was effective for b-DCPU removal during the initial stage of the process. However, the effective etching rate decreased substantially with increasing process duration, while prolonged plasma exposure was accompanied by the formation of a white opaque residue.

These results indicate that the current etching condition is not yet sufficient for reliable removal of relatively thick b-DCPU layers over extended etching times. Further optimization is therefore required to maintain an effective polymer removal rate and to suppress or remove the post-etch residue. Despite this limitation, the combination of the patterned SiN hard mask, O_2/Ar plasma etching, and endpoint monitoring established a workable process route for local b-DCPU patterning and provided a basis for further optimization of the polymer dry-etching step.

4.7.7. Final Integrated Device and Process Validation

Due to the limited availability of functional detector samples, the complete integration workflow was validated using a previously processed detector in which the optical transmission window had not been fully opened. This sample was therefore not intended for final optical characterization, but was used as a process-validation platform to evaluate whether the individual fabrication steps could be sequentially integrated on the detector structure.

The final state of the fabricated sample is shown in Figure 4.8. The major fabrication steps, including temporary bonding, front-side metal patterning, Fabry–Pérot filter integration, UCNP deposition, b-DCPU coating, SiN protection-layer formation, photolithography, and polymer patterning, could be carried out on the same device. The resulting structure demonstrates that the proposed multilayer integration sequence is practically feasible and that the different material systems can be processed

within a common fabrication workflow.

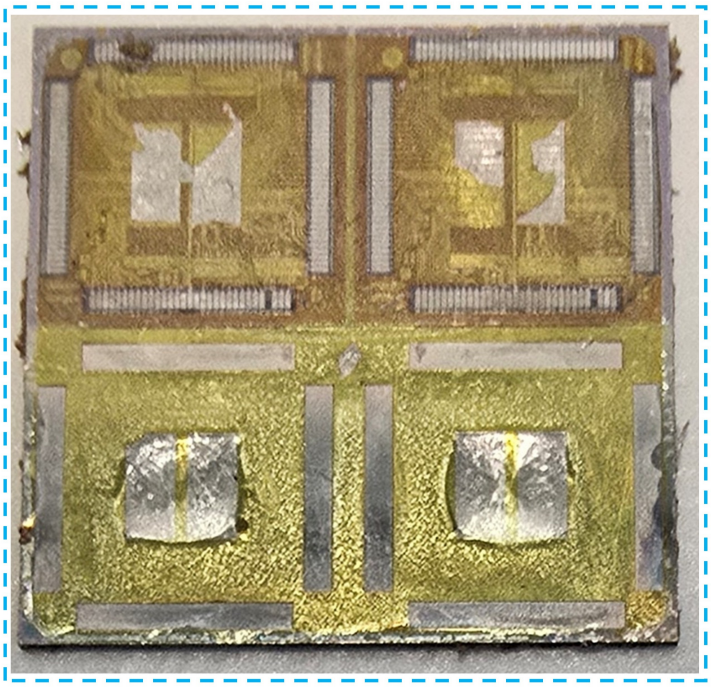


Figure 4.8: Final integrated device used for fabrication-process validation. The completed structure was assessed by optical inspection and interpreted together with the characterization results obtained during the preceding fabrication stages. Due to the limited availability of functional detector samples, the demonstrated device was fabricated using a previously processed detector in which the optical transmission window had not been fully opened. The sample was therefore used to evaluate the feasibility of the complete multilayer integration workflow rather than for final optical characterization. Most of the intended device structure was successfully integrated, although partial removal of the front-side Mo light-blocking layer was observed after lift-off and subsequent processing.

The sample therefore served as a process-validation platform for evaluating the integration workflow rather than as a fully functional optical sensing device, together with the characterization results obtained during the preceding fabrication stages. The Fabry–Pérot filter deposition and patterning were evaluated through thin-film thickness measurements and etching characterization, the UCNP layer was examined by SEM and AFM, and the b-DCPU layer was characterized in terms of thickness and mechanical properties. Endpoint monitoring was additionally used during SiN and b-DCPU dry etching. The final device image should therefore be interpreted together with these intermediate characterization results, rather than as an independent demonstration of complete optical or electrical functionality.

However, partial removal of the front-side Mo light-blocking layer was observed after completion of the process. Part of the patterned metal was unintentionally detached during the lift-off and subsequent processing steps. This indicates that the adhesion and mechanical robustness of the Mo pattern remain important limitations of the current fabrication sequence. The observed metal loss may be related to the combined effects of prolonged solvent exposure, interfacial adhesion, and mechanical stresses introduced during handling and subsequent processing, although the dominant mechanism was not independently identified in this study.

In addition, because the optical transmission window of the detector used for this demonstration was not fully opened, the fabricated sample cannot be regarded as a fully functional final device. The optical transmission window refers to the locally thinned region of the silicon detector through which the excitation light is intended to propagate toward the underlying tissue. Since this region was not fully defined in the validation sample, the intended excitation and detection pathways could not be functionally verified. Instead, the sample serves as a proof of process integration, demonstrating that the principal fabrication steps can be combined into a single multilayer structure. Future fabrication

should therefore focus on improving the robustness of the Mo light-blocking layer and repeating the complete integration sequence on a detector with a fully defined optical transmission window.

5 Discussion

5.1. Overall Integration Strategy

The main challenge of this work lies in integrating materials and fabrication steps with different mechanical, chemical, and optical requirements. The final device cannot be fabricated simply according to the stacking order of the functional layers; instead, the process sequence must be adapted to preserve detector integrity, optical performance, and electrical accessibility throughout fabrication.

Several process decisions were therefore determined by integration constraints. Temporary bonding was introduced before the first photolithography step to protect the locally thinned detector during vacuum-assisted spin coating. The final backside thinning was postponed in order to maintain sufficient substrate stability and surface flatness during multilayer deposition. In addition, a SiN intermediate layer was introduced to isolate b-DCPU from direct contact with photoresist and to serve as a hard mask for polymer patterning, although this required additional control of the thermal load during deposition. Taken together, these process adaptations enabled the major front-side fabrication steps to be combined within a single sequential workflow rather than being developed only as isolated material or component processes.

A key outcome of this work is therefore the establishment of a practical heterogeneous integration strategy in which temporary bonding, optical multilayer deposition, nanoparticle deposition, polymer processing, hard-mask patterning, and delayed backside thinning are coordinated within one device fabrication sequence. This represents an important step beyond the separate fabrication of the individual functional layers, because the integration sequence was developed while simultaneously preserving the requirements for optical access, electrical contact, mechanical support, and material compatibility.

These results show that the feasibility of the proposed device depends not only on the performance of the individual functional layers, but also on the compatibility of the complete fabrication sequence. The process flow developed in this study therefore provides an experimentally established basis for the subsequent realization of the complete integrated device. Although several individual process steps still require further optimization, the overall integration route has been demonstrated sufficiently to identify the remaining limitations as specific process-level challenges rather than as a fundamental incompatibility of the proposed device architecture.

5.2. Optical Functional Layer Integration

The integration of the Fabry–Pérot filter and UCNP layer demonstrated that the main wavelength-selective and upconversion-related functions of the proposed optical stack could be incorporated within the same fabrication sequence. The deposited FP filter showed a spectral response comparable to the previously fabricated reference sample, while the CHF_3/Ar etching condition provided improved selectivity for patterning the approximately 1 µm multilayer structure. Importantly, the FP multilayer could be deposited, patterned, and subsequently combined with the UCNP deposition process without eliminating the intended wavelength-dependent optical response. This demonstrates that the two principal optical functional layers can be integrated sequentially rather than being treated only as separately fabricated components.

For the UCNP layer, deposition uniformity was found to depend strongly on the drying condition. Humidity control combined with lower-temperature drying produced the clearest improvement in spatial confinement and macroscopic uniformity, whereas the additional use of glycerol and sodium citrate did not result in an obvious further improvement under the tested conditions. Within the investigated process window, this indicates that controlling the drying environment was the most effective parameter for improving the macroscopic deposition morphology. In particular, the humidity-controlled, lower-temperature condition provided a practical route for obtaining a more spatially

confined UCNP deposit without introducing additional suspension modification. This represents a useful process improvement because localized UCNP deposition is required to maintain the intended optical functional area while avoiding unnecessary particle coverage of surrounding device structures.

The optimized deposition process therefore established a reproducible route for forming a continuous, localized UCNP layer on top of the FP filter. However, the measured UCNP thickness remained above the approximately 1 µm design target, with measured values in the range of approximately 1.6 µm to 2.2 µm. Further control of deposited volume and particle loading is therefore still required to bring the layer thickness closer to the intended design value. In addition, the optical-power measurements showed that the UCNP-containing sample produced an increasingly positive power difference relative to the filter-only reference as the excitation level was increased. This provides experimental evidence that the integrated UCNP layer contributes an additional optical signal under 808 nm excitation. At the same time, because the present setup measures integrated optical power rather than spectrally resolved emission, the observed difference cannot yet be interpreted as the absolute upconversion-emission power or as a quantitative upconversion efficiency. Overall, the optical-layer experiments demonstrate that the FP filter and UCNP layer can be fabricated and combined within the proposed device architecture while retaining their intended process-level optical roles. The remaining work is therefore focused primarily on quantitative optimization of UCNP thickness and wavelength-resolved optical validation rather than on establishing the basic compatibility of the two optical layers.

5.3. Mechanical and Polymer Integration

The b-DCPU layer plays a central role in the mechanical integration of the device because it serves as the flexible supporting substrate while also remaining within the optical path. The measured Young's modulus of approximately 3.37 MPa confirms that the material itself is relatively compliant. However, the structural response of the polymer layer depends strongly on its thickness, particularly when tensile and flexural rigidities are considered.

The mechanical analysis showed that the initial polymer thickness was too large to satisfy the adopted tensile-rigidity criterion for myocardial compatibility. Since the tensile rigidity scales linearly with thickness, reducing the b-DCPU layer was necessary to improve mechanical matching. A particularly useful outcome of this analysis is that the required mechanical adjustment could be achieved through thickness control rather than through reformulation of the polymer composition. The calculated thickness required to match the adopted tensile-rigidity criterion was approximately 22.6 µm, which lies within the predefined design range of 15 µm to 25 µm.

The optimized spin-coating process produced films with an average thickness of approximately 17.8 µm, demonstrating experimentally that the required thickness range is accessible using the developed deposition process. Using the measured mean Young's modulus, this optimized thickness corresponds to a calculated tensile rigidity per unit width of approximately 59.9 $\mathrm{N\,m^{-1}}$, compared with the adopted cardiac reference of 76 $\mathrm{N\,m^{-1}}$. The process therefore provides a practical means of tuning the supporting polymer toward the intended tensile-rigidity range.

The flexural rigidity showed a different behavior because of its cubic dependence on thickness. The calculated bending stiffness of the b-DCPU layer was substantially lower than the adopted cardiac reference value, indicating that the polymer remains highly compliant under bending. This high bending compliance is advantageous for a thin supporting layer that must conform to soft tissue and accommodate local deformation. However, the same mechanical compliance also introduces a fabrication trade-off, because thinner polymer films become increasingly sensitive to handling and to stresses introduced during subsequent processing. Polymer integration therefore requires balancing mechanical compliance against fabrication robustness. Reducing the b-DCPU thickness improves tensile matching and bending flexibility, but also narrows the process window for lithography, thin-film deposition, and dry etching.

Importantly, the developed fabrication sequence already incorporates process adaptations to manage this trade-off. The SiN protection layer separates the b-DCPU from direct photoresist contact and provides a hard mask for subsequent polymer patterning, while the interrupted SiN deposition procedure reduces the thermal load applied to the polymer.

The thermal sensitivity observed during SiN deposition nevertheless shows that b-DCPU remains one of the process-sensitive materials in the overall integration sequence. Further optimization is therefore required mainly to increase the robustness of processing rather than to establish the basic feasibility of using b-DCPU as the supporting substrate. The optical properties of the integrated polymer layer also support its use in the proposed device.

The measured transmittance spectrum of the combined b-DCPU/FP-filter stack showed that the wavelength-dependent response of the underlying optical filter was retained after polymer integration. In particular, the combined structure maintained relatively high transmission outside the attenuation band while preserving pronounced attenuation in the approximately 400 nm to 460 nm region. This is an important integration result because the polymer layer provides the required mechanical support while remaining compatible with the optical function of the underlying filter stack.

Overall, the results demonstrate that b-DCPU can satisfy the combined mechanical, fabrication, and optical requirements of the proposed architecture within an experimentally accessible thickness range. The remaining challenges are therefore associated primarily with improving processing robustness and reproducibility rather than with the fundamental suitability of the polymer for device integration.

5.4. Dry-Etching Challenges and Process Control

Dry etching was one of the most critical fabrication steps because both the SiN protection layer and the underlying b-DCPU had to be patterned without damaging the remaining device structure.

For SiN etching, endpoint monitoring provided a practical means of identifying the final stage of material removal. Although the detailed signal evolution varied between different samples, a reproducible transition to pronounced high-frequency fluctuations was observed near the endpoint. This suggests that endpoint monitoring can be used as a useful process-control tool, although it should be interpreted together with surface inspection and other measurements. An important outcome of the present process development is that the photolithographic pattern could be transferred first into the SiN hard mask and subsequently into the underlying polymer, establishing a complete dry-patterning route for b-DCPU within the integrated device workflow.

The b-DCPU etching process nevertheless showed a pronounced time-dependent limitation. Under the O_2/Ar plasma condition, the polymer was removed relatively rapidly during the initial stage, but the effective removal rate decreased substantially with increasing process duration. The average removal depths measured by profilometry were approximately 12.60 µm, 16.69 µm, and 17.74 µm after 1 h, 2 h, and 3 h. These values correspond to incremental effective removal rates of approximately 12.60 µm h^{-1}, 4.09 µm h^{-1}, and 1.05 µm h^{-1} during the first, second, and third hour, respectively. The process therefore clearly deviated from constant-rate etching during prolonged plasma exposure. Such time-dependent behavior is plausible for polyurethane-based materials because oxygen-plasma exposure does not result only in physical material removal. Previous studies have shown that polyurethane surfaces exposed to oxygen plasma undergo simultaneous oxidation, surface functionalization, morphological modification, and plasma-induced etching [44, 46]. For example, oxygen-plasma-treated polyurethane has been reported to develop additional oxygen-containing functionalities such as hydroxyl, carbonyl, and related oxidized groups, together with changes in surface morphology [44, 46]. Moles et al. further reported changes in the oxidation state and increased crosslinking associated with the isocyanate region of oxygen-plasma-etched polyurethane [47].

These observations suggest that the surface exposed during prolonged plasma etching may progressively differ chemically and structurally from the original b-DCPU. Such plasma-induced modification could contribute to the changing etching behavior observed in the present work. However, the available data do not allow the reduction in removal rate to be assigned to a single mechanism. The decrease in etching efficiency was accompanied by the formation of a white opaque residue in the exposed polymer regions. The residue could be removed mechanically and showed partial solubility in hot water and ethanol, indicating that its physical state differed from that of the original b-DCPU. The formation of this residue is also consistent with the broader observation that oxygen-plasma treatment can chemically restructure polyurethane surfaces rather than simply removing material layer by layer [44, 46, 47].

Nevertheless, none of these literature results directly identifies the composition of the white residue

observed in the present b-DCPU system. Because b-DCPU has a different chemical formulation and was exposed for much longer etching durations than those typically used for surface modification, the residue cannot be assumed to have the same composition as the modified surface layers reported in previous polyurethane studies. Possible explanations include plasma-induced oxidation, chain scission, surface restructuring, increased local crosslinking, or the accumulation of less volatile degradation products. These mechanisms are therefore treated as plausible hypotheses rather than confirmed explanations of the observed residue.

Direct chemical characterization of the post-etch surface and residue would be required to distinguish between these possibilities. Techniques such as X-ray photoelectron spectroscopy (XPS), Fourier-transform infrared spectroscopy (FTIR), or Raman spectroscopy could be used to determine whether the residue contains increased oxygen-containing groups, altered urethane bonding, or other plasma-induced degradation products. The optical endpoint signal during polymer etching also reflected the progressive change in the polymer surface. As the exposed b-DCPU became increasingly opaque, the reflected monitoring signal decreased and the initially periodic response gradually became more stable.

The simultaneous evolution of the optical appearance, removal rate, and endpoint signal further indicates that the surface condition changed substantially during prolonged plasma exposure. However, because the endpoint measurement is indirect, the changing signal cannot by itself distinguish between remaining polymer, chemically modified polymer, and post-etch residue. This behavior provided a practical indication of the later stage of the etching process, but, as with SiN etching, the endpoint signal alone cannot be regarded as direct proof of complete material removal.

Overall, the present experiments establish a workable dry-patterning route in which the SiN hard mask and the underlying b-DCPU can be sequentially patterned within the same fabrication process. The principal remaining challenge is not whether b-DCPU can be plasma patterned, but how to maintain a sufficiently stable removal rate and prevent the formation of modified or residual surface material during prolonged etching of relatively thick films. The literature suggests that optimization should therefore consider not only the nominal etching rate, but also the evolution of polyurethane surface chemistry with plasma dose. Shorter cyclic etching steps, intermediate cooling, variation of oxygen concentration and ion bombardment conditions, and post-etch residue characterization could help determine whether the observed rate reduction is dominated by thermal effects, plasma-induced surface restructuring, or residue accumulation.

Despite the remaining limitation, the current process has already identified the critical transition from efficient initial removal to strongly reduced long-duration etching. This provides a quantitative and mechanistic basis for targeted optimization of the polymer-patterning step in the next fabrication iteration.

5.5. Final Device Validation and Remaining Limitations

The final process-validation sample demonstrated that the major fabrication steps developed in this study could be integrated within a single device workflow. The sequence including temporary bonding, Mo patterning, Fabry–Pérot filter integration, UCNP deposition, b-DCPU coating, SiN protection, photolithography, and polymer patterning was successfully combined on the same detector structure.

This is a significant outcome of the present work because these processing steps involve materials with substantially different mechanical, chemical, thermal, and optical requirements. Their successful sequential integration shows that the proposed heterogeneous device architecture can be translated from a conceptual layer stack into a practical fabrication route. The process-validation sample therefore provides experimental evidence for the overall feasibility of the proposed integration strategy and establishes a fabrication platform on which the final functional device can be completed.

The demonstrated sample was fabricated using a detector in which the optical transmission window had not been fully opened. Consequently, the sample was not suitable for complete optical validation of the intended excitation and detection pathway and should therefore be regarded as a process-validation device rather than as a fully functional sensing device. Importantly, this limitation does not prevent evaluation of the fabrication compatibility of the multilayer integration sequence itself. The sample was sufficient to demonstrate that the principal front-side fabrication steps could be performed sequentially

on the detector without preventing completion of the overall integration workflow. Final verification of the complete sensing concept will require repetition of the developed process on a detector with the intended optical-window geometry, followed by wavelength-resolved optical characterization and electrical readout of the integrated photodetector.

One remaining process-level limitation is the mechanical robustness of the front-side Mo light-blocking layer. Partial removal of the patterned Mo was observed after lift-off and subsequent fabrication steps, indicating that the metal adhesion and stability require further improvement. The observed metal loss may be influenced by prolonged solvent exposure, interfacial adhesion, or uneven surface morphology. However, the dominant mechanism was not independently identified in this study, and these explanations should therefore be regarded as possible contributing factors rather than confirmed failure mechanisms. Because the Mo pattern could nevertheless be formed and integrated before the partial material loss occurred, the remaining challenge is primarily to improve the durability of the metal pattern through the complete fabrication sequence rather than to establish the basic feasibility of Mo patterning.

Additional optimization is also required for UCNP thickness control and long-duration b-DCPU dry etching. The current UCNP deposition process achieved localized particle deposition on the FP filter, but the measured thickness remained above the design target. Similarly, b-DCPU could be patterned through the SiN hard mask using O_2/Ar plasma etching, although the effective removal rate decreased during prolonged processing and a white post-etch residue was formed. These limitations are therefore concentrated in a relatively small number of well-defined process steps and provide clear targets for the next fabrication iteration.

Overall, the present work establishes and experimentally demonstrates a complete heterogeneous integration route for the proposed optical platform. Although the process-validation sample does not yet constitute a fully functional NADH sensing device, the principal fabrication sequence has been shown to be practically achievable. The next stage of development can therefore focus on improving process robustness and completing functional optical and electrical validation, rather than redefining the overall device-integration strategy.

5.6. Future Process Improvements

The present work has established a practical fabrication route for integrating the principal functional layers of the proposed device. The next stage of development should therefore focus on improving process robustness, reproducibility, and functional validation rather than redefining the overall integration strategy. The most important next step is to repeat the complete integration sequence on a detector with a fully opened optical transmission window, followed by optical and electrical verification of the final device. This would allow the fabrication route demonstrated in the present process-validation sample to be transferred directly to a detector geometry that supports the intended excitation and fluorescence-detection pathways.

For the optical functional layers, further optimization should focus on improving UCNP thickness control and deposition reproducibility. The current drop-casting process already provides improved spatial confinement under humidity-controlled, lower-temperature drying, demonstrating that the deposition morphology can be influenced effectively through control of the drying environment. However, the deposited UCNP layer remains thicker than the original design target. More precise control of deposited volume, particle concentration, and drying conditions may therefore help reduce both the mean layer thickness and its spatial variation while maintaining sufficient particle coverage within the optical functional region. Future optimization should also include repeated thickness measurements across multiple deposited samples so that process reproducibility and thickness variation can be quantified statistically rather than evaluated primarily from individual deposits.

The b-DCPU process also requires further development. The target polymer thickness range has already been reached through spin-coating optimization, indicating that the main remaining polymer-related challenge is the subsequent dry-patterning step rather than film formation itself. The b-DCPU dry etching remains limited by the strong reduction in effective removal rate and the formation of white residue during prolonged plasma exposure.

Future work should investigate alternative O_2/Ar plasma conditions, variation of plasma power and gas composition, and shorter cyclic etching steps with intermediate cooling in order to determine whether the long-duration rate reduction can be mitigated. Post-etch cleaning strategies should also be evaluated systematically to remove the residue without damaging the remaining b-DCPU, SiN hard mask, or underlying optical layers.

Chemical characterization of the residue should form an important part of this optimization. X-ray photoelectron spectroscopy (XPS), Fourier-transform infrared spectroscopy (FTIR), or Raman spectroscopy could be used to evaluate changes in oxidation state, urethane bonding, and other plasma-induced chemical modifications. Such measurements would help determine whether the observed residue and decreasing removal rate are associated primarily with oxidation, plasma-induced restructuring or crosslinking, thermal degradation, or the accumulation of less volatile reaction products. This information could then be used to guide the selection of a more stable etching condition.

In addition, the mechanical robustness of the front-side Mo light-blocking layer should be improved. Because the Mo patterning and lift-off process itself was successfully implemented, future development should focus primarily on maintaining metal adhesion throughout the subsequent fabrication sequence.

Surface preparation, adhesion enhancement, and optimization of the selected photoresist may reduce unintended metal delamination during later fabrication steps.

Dedicated adhesion tests or simplified process-control samples could be used to distinguish the effects of prolonged solvent exposure, interfacial adhesion, and mechanical handling on the stability of the Mo layer. Together with improved endpoint control for SiN and polymer etching, these modifications could increase the reproducibility and reliability of the complete integration workflow.

Finally, future characterization should extend from process validation to full functional testing of the integrated device. This should include wavelength-resolved optical measurements, verification of the intended excitation and detection pathways, and electrical readout of the photodetector under representative optical conditions. In particular, spectrally resolved measurements should verify transmission of the UCNP-generated UV component through the integrated optical stack, suppression of unwanted blue UCNP emission by the FP filter, and detection of the fluorescence signal returning through the backside of the photodetector.

Successful completion of these measurements would provide the final link between the fabrication strategy established in this thesis and functional validation of the proposed cardiac NADH sensing platform. The present work therefore provides a concrete experimental basis for this next stage of device development.

6 Conclusion

This thesis investigated the fabrication and heterogeneous integration of an upconversion-based optical platform for cardiac NADH sensing. The work focused on establishing a compatible process sequence for integrating a silicon photodetector, Mo light-blocking layer, Fabry–Pérot filter, UCNP layer, b-DCPU flexible substrate, and SiN protection layer within a single device architecture.

A complete front-side integration route was developed. Temporary bonding was introduced before photolithography to protect the locally thinned detector during vacuum-assisted spin coating. The Fabry–Pérot filter was fabricated using calibrated SiO_2/SiN deposition and patterned using a CHF_3/Ar dry-etching process with improved filter-to-photoresist selectivity. UCNP deposition was improved by reducing the solvent evaporation rate through humidity control and lower-temperature drying. The b-DCPU layer was optimized by spin coating to reach the target thickness range required for device integration.

Mechanical characterization showed that the fabricated b-DCPU had a Young's modulus of approximately 3.37 MPa. By considering both material stiffness and film thickness, the required polymer thickness for the adopted tensile-rigidity criterion was estimated to be approximately 22.6 µm, which is consistent with the experimentally achievable thickness range. The polymer could also be integrated above the Fabry–Pérot filter while retaining the wavelength-dependent optical response of the combined structure.

Several process limitations were identified during integration. Continuous SiN deposition introduced excessive thermal loading to b-DCPU and was therefore replaced by an interrupted deposition approach with intermediate cooling. During b-DCPU dry etching, the effective removal rate decreased with process duration and a white opaque residue formed in the exposed regions. In addition, partial delamination of the front-side Mo light-blocking layer was observed during the final fabrication sequence.

Despite these limitations, the major fabrication steps were successfully combined on a single process-validation detector, demonstrating the feasibility of the proposed multilayer integration strategy. Since the detector used for this demonstration did not contain a fully opened optical transmission window, the fabricated sample cannot yet be considered a fully functional sensing device. Future work should therefore focus on improving polymer etching and metal adhesion, controlling UCNP layer thickness more precisely, and repeating the complete process on a fully functional detector followed by wavelength-resolved optical and electrical characterization.

References

[1] Véronique L. Roger. "Epidemiology of Heart Failure". In: *Circulation Research* 113.6 (2013), pp. 646–659. DOI: 10.1161/CIRCRESAHA.113.300268. eprint: https://www.ahajournals.org/doi/pdf/10.1161/CIRCRESAHA.113.300268. URL: https://www.ahajournals.org/doi/abs/10.1161/CIRCRESAHA.113.300268.

[2] Daniel Burkhoff et al. "Reverse Remodeling With Left Ventricular Assist Devices". In: *Circulation Research* 128.10 (2021), pp. 1594–1612. DOI: 10.1161/CIRCRESAHA.121.318160. eprint: https://www.ahajournals.org/doi/pdf/10.1161/CIRCRESAHA.121.318160. URL: https://www.ahajournals.org/doi/abs/10.1161/CIRCRESAHA.121.318160.

[3] Emma J. Birks et al. "Prospective Multicenter Study of Myocardial Recovery Using Left Ventricular Assist Devices (RESTAGE-HF [Remission from Stage D Heart Failure])". In: *Circulation* 142.21 (2020), pp. 2016–2028. DOI: 10.1161/CIRCULATIONAHA.120.046415. eprint: https://www.ahajournals.org/doi/pdf/10.1161/CIRCULATIONAHA.120.046415. URL: https://www.ahajournals.org/doi/abs/10.1161/CIRCULATIONAHA.120.046415.

[4] A. Saxton, M. A. Tariq, and B. Bordoni. "Anatomy, Thorax, Cardiac Muscle". In: *StatPearls [Internet]*. Updated 2023 Aug 8. Treasure Island (FL): StatPearls Publishing, Jan. 2026. URL: https://www.ncbi.nlm.nih.gov/books/NBK535355/ (visited on 09/07/2026).

[5] Mahmoud Abdellatif, Simon Sedej, and Guido Kroemer. "NAD+ Metabolism in Cardiac Health, Aging, and Disease". In: *Circulation* 144.22 (2021), pp. 1795–1817. DOI: 10.1161/CIRCULATIONAHA.121.056589. eprint: https://www.ahajournals.org/doi/pdf/10.1161/CIRCULATIONAHA.121.056589. URL: https://www.ahajournals.org/doi/abs/10.1161/CIRCULATIONAHA.121.056589.

[6] Kristina R. Rivera et al. "Measuring and regulating oxygen levels in microphysiological systems: design, material, and sensor considerations". In: *Analyst* 144.10 (May 2019), pp. 3190–3215. ISSN: 0003-2654. DOI: 10.1039/c8an02201a. eprint: https://pubs.rsc.org/an/article-pdf/144/10/3190/6437855/c8an02201a.pdf. URL: https://doi.org/10.1039/c8an02201a.

[7] Alba Luengo et al. "Increased demand for NAD^+ relative to ATP drives aerobic glycolysis". In: *Molecular Cell* 81.4 (Feb. 2021), 691–707.e6. DOI: 10.1016/j.molcel.2020.12.012. eprint: https://pmc.ncbi.nlm.nih.gov/articles/PMC8315838/pdf/nihms-1707388.pdf. URL: https://doi.org/10.1016/j.molcel.2020.12.012.

[8] Chi Fung Lee et al. "Normalization of NAD+ Redox Balance as a Therapy for Heart Failure". In: *Circulation* 134.12 (2016), pp. 883–894. DOI: 10.1161/CIRCULATIONAHA.116.022495. eprint: https://www.ahajournals.org/doi/pdf/10.1161/CIRCULATIONAHA.116.022495. URL: https://www.ahajournals.org/doi/abs/10.1161/CIRCULATIONAHA.116.022495.

[9] Simin Cao et al. "Femtosecond Fluorescence Spectra of NADH in Solution: Ultrafast Solvation Dynamics". In: *The Journal of Physical Chemistry B* 124.5 (Jan. 2020), pp. 771–776. ISSN: 1520-6106. DOI: 10.1021/acs.jpcb.9b10656. eprint: https://pubs.acs.org/jpcbfk/article-pdf/124/5/771/9951537/jp9b10656.pdf. URL: https://doi.org/10.1021/acs.jpcb.9b10656.

[10] Jianghui Guo et al. "Non-invasive optical monitoring of human lungs: Monte Carlo modeling of photon migration in Visible Chinese Human and an experimental test on a human". In: *Biomedical Optics Express* 13.12 (Dec. 2022), pp. 6389–6403. DOI: 10.1364/BOE.472530. eprint: https://pmc.ncbi.nlm.nih.gov/articles/PMC9774858/pdf/boe-13-12-6389.pdf. URL: https://doi.org/10.1364/BOE.472530.

[11] Inês S Martins et al. "Measurement of tissue optical properties in a wide spectral range: a review [Invited]". In: *Biomedical Optics Express* 14.1 (Jan. 2023), pp. 249–298. DOI: 10.1364/BOE.479320. eprint: https://pmc.ncbi.nlm.nih.gov/articles/PMC9841994/pdf/boe-14-1-249.pdf. URL: https://doi.org/10.1364/BOE.479320.

[12] Ralph Weissleder. "A clearer vision for in vivo imaging". In: *Nature Biotechnology* 19.4 (Apr. 2001), pp. 316–317. DOI: 10.1038/86684. eprint: https://www.nature.com/articles/nbt0401_316.pdf. URL: https://doi.org/10.1038/86684.

[13] Guosong Hong, Alexander L Antaris, and Hongjie Dai. "Near-infrared fluorophores for biomedical imaging". In: *Nature Biomedical Engineering* 1.1 (Jan. 2017), p. 0010. DOI: 10.1038/s41551-016-0010. eprint: https://www.nature.com/articles/s41551-016-0010.pdf. URL: https://doi.org/10.1038/s41551-016-0010.

[14] Xian Chen et al. "Photon upconversion in core–shell nanoparticles". In: *Chemical Society Reviews* 44.6 (Mar. 2015), pp. 1318–1330. DOI: 10.1039/C4CS00151F. eprint: https://pubs.rsc.org/en/content/getauthorversionpdf/C4CS00151F. URL: https://doi.org/10.1039/C4CS00151F.

[15] J E Moffatt et al. "A practical review of shorter than excitation wavelength light emission processes". In: *Applied Spectroscopy Reviews* 55.4 (Apr. 2020), pp. 327–349. DOI: 10.1080/05704928.2019.1672712. eprint: https://www.tandfonline.com/doi/pdf/10.1080/05704928.2019.1672712. URL: https://doi.org/10.1080/05704928.2019.1672712.

[16] Markus Haase and Helmut Schäfer. "Upconverting Nanoparticles". In: *Angewandte Chemie International Edition* 50.26 (2011), pp. 5808–5829. DOI: https://doi.org/10.1002/anie.201005159. eprint: https://onlinelibrary.wiley.com/doi/pdf/10.1002/anie.201005159. URL: https://onlinelibrary.wiley.com/doi/abs/10.1002/anie.201005159.

[17] Ton Koonen. "Fabry-Perot interferometer filters". In: *Wavelength Filters in Fibre Optics*. Ed. by Herbert Venghaus. Vol. 123. Springer Series in Optical Sciences. Berlin, Heidelberg: Springer, 2006, pp. 271–287. DOI: 10.1007/3-540-31770-8_7. URL: https://doi.org/10.1007/3-540-31770-8_7.

[18] Sara Pimenta et al. "High-selectivity neural probe based on a Fabry–Perot optical filter and a CMOS silicon photodiodes array at visible wavelengths". In: *Journal of Biomedical Optics* 23.10 (Oct. 2018), p. 105004. DOI: 10.1117/1.JBO.23.10.105004. URL: https://doi.org/10.1117/1.JBO.23.10.105004.

[19] Authors/Task Force Members: et al. "2023 Focused Update of the 2021 ESC Guidelines for the diagnosis and treatment of acute and chronic heart failure". In: *European Journal of Heart Failure* 26.1 (2024), pp. 5–17. DOI: https://doi.org/10.1002/ejhf.3024. eprint: https://onlinelibrary.wiley.com/doi/pdf/10.1002/ejhf.3024. URL: https://onlinelibrary.wiley.com/doi/abs/10.1002/ejhf.3024.

[20] José Lifante et al. "The role of tissue fluorescence in in vivo optical bioimaging". In: *Journal of Applied Physics* 128.17 (Nov. 2020), p. 171101. DOI: 10.1063/5.0021854. eprint: https://repositorio.uam.es/bitstream/handle/10486/708900/9016282.pdf. URL: https://doi.org/10.1063/5.0021854.

[21] Lingyan Shi et al. "Transmission in near-infrared optical windows for deep brain imaging". In: *Journal of Biophotonics* 9.1-2 (2016), pp. 38–43. DOI: https://doi.org/10.1002/jbio.201500192. eprint: https://onlinelibrary.wiley.com/doi/pdf/10.1002/jbio.201500192. URL: https://onlinelibrary.wiley.com/doi/abs/10.1002/jbio.201500192.

[22] Steven L. Jacques. "Optical properties of biological tissues: a review". In: *Physics in Medicine & Biology* 58.11 (June 2013), R37–R61. DOI: 10.1088/0031-9155/58/11/R37. eprint: https://iopscience.iop.org/article/10.1088/0031-9155/58/11/R37/pdf. URL: https://doi.org/10.1088/0031-9155/58/11/R37.

[23] Ye-Fu Wang et al. "Nd3+-Sensitized Upconversion Nanophosphors: Efficient In Vivo Bioimaging Probes with Minimized Heating Effect". In: *ACS Nano* 7.8 (July 2013), pp. 7200–7206. DOI: 10.1021/nn402601d. URL: https://doi.org/10.1021/nn402601d.

[24] Han-Lin Wei et al. "Tuning Near-Infrared-to-Ultraviolet Upconversion in Lanthanide-Doped Nanoparticles for Biomedical Applications". In: *Advanced Optical Materials* 11.11 (2023), p. 2201716. DOI: https://doi.org/10.1002/adom.202201716. eprint: https://advanced.onlinelibrary.wiley.com/doi/pdf/10.1002/adom.202201716. URL: https://advanced.onlinelibrary.wiley.com/doi/abs/10.1002/adom.202201716.

[25] CD Bioparticles. *DiagNano™ Water Dispersible Upconverting Nanoparticles, Absorbance Max 808 nm, Core-Shell, 365 nm/475 nm*. Product Datasheet, Cat. No. DNL-C073. Accessed: September 2026. URL: https://www.cd-bioparticles.com/product/diagnano-water-dispersible-upconverting-nanoparticles-absorbance-max-808-nm-core-shell-365-nm-475-nm-item-dnl-c073-14325.html.

[26] Feng Wang and Xiaogang Liu. "Recent advances in the chemistry of lanthanide-doped upconversion nanocrystals". In: *Chemical Society Reviews* 38.4 (Apr. 2009), pp. 976–989. DOI: 10.1039/B809132N. eprint: https://lab.semi.ac.cn/download/0.6887025825122697.pdf. URL: https://doi.org/10.1039/B809132N.

[27] Palak Jethva et al. "Lanthanide-Doped Upconversion Luminescent Nanoparticles—Evolving Role in Bioimaging, Biosensing, and Drug Delivery". In: *Materials* 15.7 (2022), p. 2374. DOI: 10.3390/ma15072374. eprint: https://mdpi-res.com/d_attachment/materials/materials-15-02374/article_deploy/materials-15-02374.pdf. URL: https://doi.org/10.3390/ma15072374.

[28] Sanyang Han et al. "Enhancing Luminescence in Lanthanide-Doped Upconversion Nanoparticles". In: *Angewandte Chemie International Edition* 53.44 (2014), pp. 11702–11715. DOI: https://doi.org/10.1002/anie.201403408. eprint: https://onlinelibrary.wiley.com/doi/pdf/10.1002/anie.201403408. URL: https://onlinelibrary.wiley.com/doi/abs/10.1002/anie.201403408.

[29] Ting Cheng et al. "Small and Bright Lithium-Based Upconverting Nanoparticles". In: *Journal of the American Chemical Society* 140.40 (Sept. 2018), pp. 12890–12899. DOI: 10.1021/jacs.8b07086. URL: https://doi.org/10.1021/jacs.8b07086.

[30] H. Angus Macleod. *Thin-Film Optical Filters*. 4th ed. Series in Optics and Optoelectronics. Boca Raton, FL: CRC Press/Taylor & Francis, 2010. 782 pp. ISBN: 978-1-4200-7302-7. DOI: 10.1201/9781420073034. URL: https://doi.org/10.1201/9781420073034.

[31] Haoxiang Jiang. "Design and Optimization of Implantable Light Emitter Through Upconverting Materials for Cardiac Muscle Concentration Monitoring". Master's thesis. Delft, The Netherlands: Delft University of Technology, 2025. URL: https://resolver.tudelft.nl/uuid:2210987a-a6cf-4f8a-a0a8-fe77f1587c6e.

[32] Xin Tang, Yichun He, and Jia Liu. "Soft bioelectronics for cardiac interfaces". In: *Biophysics Reviews* 3.1 (Jan. 2022), p. 011301. DOI: 10.1063/5.0069516. eprint: https://pmc.ncbi.nlm.nih.gov/articles/PMC10903430/pdf/. URL: https://doi.org/10.1063/5.0069516.

[33] Sung-Hyuk Sunwoo et al. "Soft bioelectronics for the management of cardiovascular diseases". In: *Nature Reviews Bioengineering* 2.1 (Jan. 2024), pp. 8–24. DOI: 10.1038/s44222-023-00102-z. URL: https://doi.org/10.1038/s44222-023-00102-z.

[34] Sung-Hyuk Sunwoo et al. "Wearable and Implantable Soft Bioelectronics: Device Designs and Material Strategies". In: *Annual Review of Chemical and Biomolecular Engineering* 12.Volume 12, 2021 (2021), pp. 359–391. ISSN: 1947-5446. DOI: https://doi.org/10.1146/annurev-chembioeng-101420-024336. URL: https://www.annualreviews.org/content/journals/10.1146/annurev-chembioeng-101420-024336.

[35] Ja Hoon Koo et al. "Soft Implantable Bioelectronics". In: *ACS Materials Letters* 3.11 (Nov. 2021), pp. 1528–1540. DOI: 10.1021/acsmaterialslett.1c00438. URL: https://doi.org/10.1021/acsmaterialslett.1c00438.

[36] Shoubhik Gupta et al. "Ultra-thin chips for high-performance flexible electronics". In: *npj Flexible Electronics* 2.1 (Mar. 2018), p. 8. DOI: 10.1038/s41528-018-0021-5. URL: https://doi.org/10.1038/s41528-018-0021-5.

[37] Yeon Sik Choi et al. "Stretchable, dynamic covalent polymers for soft, long-lived bioresorbable electronic stimulators designed to facilitate neuromuscular regeneration". In: *Nature Communications* 11.1 (Nov. 2020), p. 5990. DOI: 10.1038/s41467-020-19660-6. eprint: https://www.nature.com/articles/s41467-020-19660-6.pdf. URL: https://doi.org/10.1038/s41467-020-19660-6.

[38] Breno Rocha Barrioni et al. "Synthesis and characterization of biodegradable polyurethane films based on HDI with hydrolyzable crosslinked bonds and a homogeneous structure for biomedical applications". In: *Materials Science and Engineering: C* 52 (July 2015), pp. 22–30. DOI: 10.1016/j.msec.2015.03.027. URL: https://doi.org/10.1016/j.msec.2015.03.027.

[39] Maria G. Bauer et al. “Wetting behavior and stability of surface-modified polyurethane materials”. In: *Plasma Processes and Polymers* 18.11 (2021), p. 2100126. DOI: https://doi.org/10.1002/ppap.202100126. eprint: https://onlinelibrary.wiley.com/doi/pdf/10.1002/ppap.202100126. URL: https://onlinelibrary.wiley.com/doi/abs/10.1002/ppap.202100126.

[40] T. Yamamoto, J.R. Newsome, and D.S. Ensor. “Modification of surface energy, dry etching, and organic film removal using atmospheric-pressure pulsed-corona plasma”. In: *IEEE Transactions on Industry Applications* 31.3 (1995), pp. 494–499. DOI: 10.1109/28.382108. URL: https://doi.org/10.1109/28.382108.

[41] Dae-Hyeong Kim et al. “Electronic sensor and actuator webs for large-area complex geometry cardiac mapping and therapy”. In: *Proceedings of the National Academy of Sciences* 109.49 (Dec. 2012), pp. 19910–19915. DOI: 10.1073/pnas.1205923109. eprint: https://pmc.ncbi.nlm.nih.gov/articles/PMC3523871/pdf/. URL: https://doi.org/10.1073/pnas.1205923109.

[42] J W Hutchinson and Z Suo. “Mixed Mode Cracking in Layered Materials”. In: *Advances in Applied Mechanics*. Ed. by John W Hutchinson and Theodore Y Wu. Vol. 29. Elsevier, Jan. 1991, pp. 63–191. DOI: 10.1016/S0065-2156(08)70164-9. URL: https://doi.org/10.1016/S0065-2156(08)70164-9.

[43] Miran Mozetič. “Controlled oxidation of organic compounds in oxygen plasma”. In: *Vacuum* 71.1 (2003). Proceedings of the 9th Joint Vacuum Conference (JVC-9), organised by the Austrian Vacuum Society, in cooperation with the Vacuum societies of Hungary, Croatia, Slovenia, Czech Republic, Slovakia and Italy, Schloss Seggau, Austria, pp. 237–240. ISSN: 0042-207X. DOI: https://doi.org/10.1016/S0042-207X(02)00744-3. URL: https://www.sciencedirect.com/science/article/pii/S0042207X02007443.

[44] Rok Zaplotnik et al. “Rapid Hydrophilization of Model Polyurethane/Urea (PURPEG) Polymer Scaffolds Using Oxygen Plasma Treatment”. In: *Polymers* 8.4 (Apr. 2016), p. 144. DOI: 10.3390/polym8040144. URL: https://doi.org/10.3390/polym8040144.

[45] Marta Klanjšek Gunde et al. “Oxygen plasma etching of a two-component clear coating”. In: *Vacuum* 80.1 (2005). 10th Joint Vacuum Conference (JVC-10), Portoroz, Slovenia 28 September - 2 October 2004.Organised by the Slovenian Vacuum Society in collaboration with the Vacuum Societies of Austria, Croatia, Hungary, Czech Republic and Slovakia, pp. 189–192. ISSN: 0042-207X. DOI: https://doi.org/10.1016/j.vacuum.2005.08.010. URL: https://www.sciencedirect.com/science/article/pii/S0042207X05002885.

[46] M. R. Sanchis et al. “Surface modification of a polyurethane film by low pressure glow discharge oxygen plasma treatment”. In: *Journal of Applied Polymer Science* 105.3 (2007), pp. 1077–1085. DOI: https://doi.org/10.1002/app.26250. eprint: https://onlinelibrary.wiley.com/doi/pdf/10.1002/app.26250. URL: https://onlinelibrary.wiley.com/doi/abs/10.1002/app.26250.

[47] Matthew D. Moles, Colin A. Scotchford, and Alastair Campbell Ritchie. “Oxidation State of a Polyurethane Membrane after Plasma Etching”. In: *Conference Papers in Science* 2014.1 (2014), p. 347979. DOI: https://doi.org/10.1155/2014/347979. eprint: https://onlinelibrary.wiley.com/doi/pdf/10.1155/2014/347979. URL: https://onlinelibrary.wiley.com/doi/abs/10.1155/2014/347979.

A Fabrication Recipes

This appendix summarizes the main fabrication recipes and process conditions used throughout this study. The main recipes are presented in the order of the fabrication workflow used for device integration. Additional process development experiments and alternative recipes that were evaluated but not adopted as the final process are collected separately at the end of the appendix. Only experimentally applied or explicitly specified process conditions are included.

A.1. Mo Light-Blocking Layer

A.1.1. Photolithography Recipe

The S1813 positive photoresist process used for patterning the front-side Mo light-blocking layer is summarized in Table A.1.

Table A.1: Photolithography recipe used for Mo light-blocking layer patterning.

Process step	Condition
Photoresist	S1813 positive photoresist
Spin coating	2000 rpm, 55 s
Soft bake	2 min
Exposure dose	220
Defocus	−7
Developer	MF-322
Development time	30 s
DI-water rinse	30 s

A.1.2. Mo Deposition and Lift-Off

The principal Mo deposition and lift-off conditions are summarized in Table A.2.

Table A.2: Mo deposition and lift-off conditions.

Process parameter	Condition
Nominal target Mo thickness	approximately 200 nm
Deposition time	4 min 55 s
Lift-off solvent	Acetone
Lift-off duration	approximately 16 h

The approximately 200 nm Mo thickness represents the nominal deposition target and was not independently verified by a separate post-deposition thickness measurement on the integrated detector.

A.2. Fabry–Pérot Filter Fabrication

A.2.1. Deposition-Rate Calibration

Before deposition of the complete SiO_2/SiN multilayer stack, the deposition rates of SiO_2 and N-rich SiN were calibrated independently using 5 min ICPECVD test depositions. The thickness of each calibration film was subsequently measured by ellipsometry, and the resulting deposition rates were used to determine the deposition time required for each layer of the predefined Fabry–Pérot stack.

The principal ICPECVD conditions used for the calibration depositions are summarized in Table A.3.

Table A.3: ICPECVD conditions used for SiO_2 and N-rich SiN deposition-rate calibration.

Process parameter	SiO_2 calibration	N-rich SiN calibration
Base pressure	0.01 mTorr	0.01 mTorr
Deposition pressure	8.0 mTorr	2.0 mTorr
ICP RF power	1300 W	500 W
SiH_4 flow	16.0 sccm	4.0 sccm
O_2 flow	60 sccm	–
N_2 flow	–	50 sccm
Ar ring flow	10 sccm	10 sccm
Ar flow	Off	10 sccm
Calibration deposition time	5 min	5 min
Thickness measurement	Ellipsometry	Ellipsometry

The measured calibration thicknesses were used to calculate the corresponding deposition rates. These rates were then used to adjust the deposition time of each SiO_2 and SiN layer in the predefined Fabry–Pérot multilayer sequence. The total designed thickness of the complete filter was approximately 1049 nm.

A.2.2. Multilayer Deposition Recipe

Following deposition-rate calibration, the Fabry–Pérot filter was fabricated by sequential ICPECVD deposition of N-rich SiN and SiO_2 layers. The principal deposition conditions used for the two dielectric materials are summarized in Table A.4.

Table A.4: ICPECVD conditions used for deposition of the N-rich SiN and SiO_2 layers in the Fabry–Pérot filter.

Process parameter	N-rich SiN	SiO_2
Deposition pressure	2.0 mTorr	8.0 mTorr
ICP RF power	500 W	1300 W
SiH_4 flow	4.0 sccm	16.0 sccm
N_2 flow	50.0 sccm	–
O_2 flow	–	60.0 sccm
Deposition duration	5 min 19.89 s	1 min 12.07 s

The deposition durations were determined from the calibrated deposition rates and the predefined optical thicknesses of the individual layers in the Fabry–Pérot design. The complete multilayer stack had a total designed thickness of approximately 1049 nm.

A.2.3. Selected Dry-Etching Recipe

Based on the dry-etching comparison described in Section A.7.1, the CHF_3/Ar condition was selected for patterning the SiO_2/SiN multilayer stack.

Table A.5: Selected CHF_3/Ar dry-etching condition used for Fabry–Pérot filter patterning.

Process parameter	Condition
CHF_3 flow	50 sccm
Ar flow	5.0 sccm
Plasma power	100 W
Test duration	10 min
Measured filter removal	364 nm
Measured photoresist removal	274 nm
Filter-to-photoresist selectivity	1.33

A.3. UCNP Deposition

A.3.1. Selected Drop-Casting Condition

The UCNP deposition process used for device integration was based on reduced solvent evaporation through humidity-controlled, lower-temperature drying. The selected deposition conditions are summarized in Table A.6.

Table A.6: Selected process conditions used for UCNP drop casting.

Process parameter	Condition
Deposition method	Drop casting
Single-droplet volume	approximately 10 µL
Drying temperature	approximately 40 °C
Humidity control	Wet sponge inside enclosed local environment
Surface O_2 plasma treatment	Not used in selected process

The additional double-solvent condition investigated during process development is reported separately in Section A.7.2.

A.4. b-DCPU Preparation and Deposition

A.4.1. Polymer Synthesis and Curing

Bioresorbable dynamic covalent polyurethane (b-DCPU) was prepared from polycaprolactone triol (PCL-triol) and hexamethylene diisocyanate (HDI). The principal synthesis and curing conditions are summarized in Table A.7.

Table A.7: b-DCPU preparation and curing conditions.

Process parameter	Condition
Polyol precursor	PCL-triol, $M_n \approx 300$
Isocyanate precursor	HDI
Target crosslinking ratio	80%
Mixing method	Magnetic stirring
Mixing temperature	approximately 60 °C
Mixing duration	approximately 4.5 h
Catalyst	None
Degassing	Rest until most visible bubbles disappeared
Thermal curing temperature	120 °C
Thermal curing duration	4 h

A.4.2. Selected Spin-Coating Recipe

The b-DCPU spin-coating process consisted of three programmed stages. The parameters in Table A.8 are reported in the order rotational speed/acceleration/time, with units of rpm, rpm/s, and s, respectively.

Table A.8: Selected b-DCPU spin-coating recipe used to obtain a film within the target thickness range. The measured thickness is reported as mean ± SEM ($n = 3$).

Process step	Condition	Result
Step 1	500/300/40	–
Step 2	4000/1200/55	–
Step 3	0/300/55	–
Measured film thickness	–	17.77 ± 1.69 µm

The selected 4000 rpm second-stage condition produced a mean film thickness of (17.77 ± 1.69) µm, reported as mean ± SEM based on three measurements ($n = 3$). This value falls within the target thickness range of approximately 15 µm to 25 µm.

The complete spin-coating optimization series is summarized separately in Section A.7.3.

A.5. SiN Protective Layer

A.5.1. Interrupted Low-Stress SiN Deposition

A low-stress SiN ICPECVD recipe was used to form the protective and hard-mask layer on top of the b-DCPU film. Because prolonged continuous plasma exposure produced visible damage to the polymer, the standard deposition process was divided into shorter deposition cycles with intermediate sample removal and cooling.

The principal ICPECVD parameters of the low-stress SiN recipe are summarized in Table A.9.

Table A.9: Principal ICPECVD parameters of the low-stress SiN recipe used for the protective layer on b-DCPU.

Process parameter	Condition
Process type	Low-stress SiN ICPECVD
Process temperature	approximately 75 °C
Base pressure	0.037 mTorr
Deposition pressure	2.0 mTorr
ICP RF power	500 W
SiH_4 flow	26 sccm
N_2 flow	25 sccm
Recipe nominal deposition rate	approximately 45 nm min^{-1}
Standard recipe deposition duration	1 min

For integration on b-DCPU, the continuous deposition step was replaced by an interrupted deposition procedure, as summarized in Table A.10.

Table A.10: Interrupted low-stress SiN deposition procedure used on b-DCPU.

Process parameter	Condition
Deposition duration per cycle	30 s
Number of deposition cycles	4
Intermediate step	Sample removal and cooling
Total plasma deposition time	approximately 120 s
Calculated nominal thickness per cycle	approximately 22.5 nm
Calculated nominal accumulated thickness	approximately 90 nm

The nominal SiN thickness deposited during each cycle was calculated as

$$45\,\mathrm{nm\,min^{-1}} \times 0.5\,\mathrm{min} = 22.5\,\mathrm{nm}. \tag{A.1}$$

After four deposition cycles, the nominal accumulated thickness was therefore

$$4 \times 22.5\,\mathrm{nm} = 90\,\mathrm{nm}. \tag{A.2}$$

The accumulated SiN thickness of approximately 90 nm is therefore a nominal value calculated from the recipe deposition rate and total plasma deposition time. It was not independently verified by a post-deposition thickness measurement on the polymer-supported sample.

A.6. b-DCPU Dry Etching

A.6.1. O_2/Ar Plasma Recipe

The patterned SiN layer was used as the hard mask for b-DCPU dry etching. The selected plasma condition is summarized in Table A.11.

Table A.11: O_2/Ar plasma condition used for b-DCPU dry etching.

Process parameter	Condition
O_2 flow	80 sccm
Ar flow	5 sccm
Plasma power	200 W
Mask material	Patterned SiN

The measured thickness reduction during prolonged etching is summarized in Table A.12.

Table A.12: Measured b-DCPU thickness reduction at different dry-etching durations.

Total etching time	Total thickness reduction
1 h	12.60 µm
2 h	16.69 µm
3 h	17.74 µm

A reduction in the effective etching rate and formation of a white opaque residue were observed during prolonged plasma exposure.

A.7. Additional Process Development and Alternative Recipes

The following experiments were performed during process development to compare alternative fabrication conditions. These conditions were not used as the final selected recipes for the integrated device workflow.

A.7.1. Fabry–Pérot Dry-Etching Recipe Comparison

Two CHF_3-based dry-etching conditions were evaluated during development of the Fabry–Pérot filter patterning process.

Table A.13: Dry-etching recipes evaluated during Fabry–Pérot filter process development.

Recipe	CHF_3 flow	Additional gas	Plasma power	Test duration
CHF_3/O_2	50 sccm	O_2: 5 sccm	100 W	10 min
CHF_3/Ar	50 sccm	Ar: 5 sccm	100 W	10 min

The corresponding experimentally measured removal amounts are summarized in Table A.14.

Table A.14: Measured removal amounts and filter-to-photoresist selectivities for the tested Fabry–Pérot etching recipes.

Recipe	Filter removal	Photoresist removal	Selectivity
CHF_3/O_2	324 nm	466 nm	0.70
CHF_3/Ar	364 nm	274 nm	1.33

The CHF_3/Ar condition provided the higher filter-to-photoresist selectivity and was therefore selected for the main fabrication workflow.

A.7.2. UCNP Double-Solvent Test

An additional UCNP deposition condition was evaluated to determine whether modification of the suspension further improved the deposited morphology.

Table A.15: Alternative UCNP deposition condition evaluated using a double-solvent system and surfactant.

Parameter	Condition
Main solvent	H_2O
Secondary solvent	Glycerol
H_2O:glycerol volume ratio	50:1
Surfactant	Sodium citrate
Drying condition	Humidity control + lower temperature

Under the tested conditions, this additional suspension modification did not produce a clear improvement compared with the selected humidity-controlled, lower-temperature deposition process.

A.7.3. b-DCPU Spin-Coating Optimization

Several spin-coating conditions were evaluated before selection of the 4000 rpm second-stage condition used in the main fabrication workflow. The parameters for each step are reported in the order rotational speed/acceleration/time, with units of rpm, rpm/s, and s, respectively.

Table A.16: b-DCPU spin-coating conditions evaluated during thickness optimization and the corresponding measured film thicknesses. Thickness values are reported as mean ± SEM (n = 3).

Recipe	Step 1	Step 2	Step 3	Thickness (µm)
Previous recipe	500/300/40	1000/1200/5	0/300/5	74.21 ± 1.93
New recipe 1	500/300/40	2000/1200/55	0/300/55	33.38 ± 2.34
New recipe 2	500/300/40	3000/1200/55	0/300/55	27.27 ± 1.78
Selected recipe	500/300/40	4000/1200/55	0/300/55	17.77 ± 1.69

Increasing the second-stage rotational speed progressively reduced the measured film thickness. The 4000 rpm condition was selected because it produced a film thickness within the intended 15 µm to 25 µm range.